Constraints on Gas Mass Fractions and Cosmology From X-ray and Sunyaev-Zel'dovich Effect Data for a Sample of 36 Galaxy Clusters

Samuel J. LaRoque[1], Massimiliano Bonamente[2,3], John E. Carlstrom[1,4,5], Marshall Joy[3], Erik D. Reese[6]

ABSTRACT

We present a study of 36 massive galaxy clusters at redshifts $0.14 \leq z \leq 0.89$, whose properties are used to constrain cluster structure and cosmological models. The clusters are studied at both X-ray wavelengths using data from the *Chandra X-ray Observatory*, and at centimeter wavelengths using Sunyaev-Zel'dovich Effect (SZE) data from the BIMA and OVRO interferometric arrays. We motivate and adopt an isothermal β-model with central 100 kpc excluded from the X-ray data to describe the intracluster medium in all 36 clusters. This model is shown to provide consistently good fits to clusters with a wide range of morphological properties. Best-fit cluster gas masses and total masses are determined from this model, and cluster gas mass fractions from both X-ray and SZE data are compared and the implications for cluster structure noted. The gas mass fractions are used to obtain constraints on Ω_M and Ω_Λ both by comparing the mean $f_{\rm gas}$ values to Ω_B/Ω_M for assumed Ω_B, and by assuming that $f_{\rm gas}$ should be constant with redshift and determining what cosmology best facilitates this. Cosmological constraints are found to be consistent with CMB results, but a better understanding of the cluster baryon budget is needed to achieve the same level of precision.

---

[1]Kavli Institute for Cosmological Physics, Department of Astronomy and Astrophysics, University of Chicago, Chicago, IL 60637

[2]Department of Physics, University of Alabama, Huntsville, AL 35812

[3]NASA Marshall Space Flight Center, Huntsville, AL 35812

[4]Department of Physics, University of Chicago, Chicago, IL 60637

[5]Enrico Fermi Institute, University of Chicago, Chicago, IL 60637

[6]Department of Physics, University of California, Davis, CA 95616

1. Introduction

As the largest collapsed objects in the universe, galaxy clusters provide valuable probes of cosmological models. Current favored models of galaxy cluster formation hold that clusters collapse from volumes on the order (10 Mpc)^3 down to typical volumes of order (1 Mpc)^3 with typical gravitational masses of $\sim 10^{14}$—10^{15} $M_\odot$. Roughly 10% of their total mass is baryonic, of which most is in the form of hot (3—10 keV) gas. Since galaxy clusters collapse from such large spatial scales, the baryonic mass fraction $f_{\rm B}$ of a cluster should reflect the ratio Ω_B/Ω_M (White et al. 1993; Evrard 1997). Measurements of $f_{\rm B}$ can be combined with independent estimates of Ω_B from, e.g., D/H measurements combined with Big Bang nucleosynthesis (BBN) predictions (Copi et al. 1995; Burles & Tytler 1998b,a; Nollett & Burles 2000; O'Meara et al. 2001) or measurements of CMB anisotropy (Spergel et al. 2003). The cluster baryon fraction and constraints on cosmology can be determined in two complementary ways; one method uses X-ray emission from galaxy clusters and the other uses an upscattering of CMB photons by the hot cluster gas called the Sunyaev-Zel'dovich Effect (SZE).

X-ray emission in clusters arises predominantly from thermal bremsstrahlung for gas electron temperatures $T_e \gtrsim 3$ keV. The X-ray emissivity is not a directly observable quantity; instead X-ray proportional counters measure the X-ray surface brightness over some frequency band,

$$S_x = \frac{1}{4\pi(1+z)^4}\int n_e n_{\rm H}\Lambda \, d\ell \tag{1}$$

where the integral is along the line of sight and Λ is called the X-ray cooling function and is proportional to $T_e^{1/2}$. Cluster X-ray emission is therefore proportional to $n_e^2 T_e^{1/2}$. The observed X-ray emission can also be used to measure the gas temperature, if the instrument has spectral capability.

The thermal SZE is a small ($\lesssim 1$ mK) distortion in the CMB spectrum caused by inverse Compton scattering of the CMB photons off of energetic electrons in the hot intracluster gas. The spectral distortion is proportional to the cluster optical depth $\tau = \int n_e \sigma_{\rm T} dl$ times the fractional energy gained per scatter, and can be expressed for dimensionless frequency $x \equiv h\nu/k_{\rm B}T_{\rm CMB}$ as a temperature change ΔT relative to the CMB temperature $T_{\rm CMB}$:

$$\frac{\Delta T}{T_{\rm CMB}} = f(x)y = f(x)\int \sigma_{\rm T} n_e \frac{k_{\rm B}T_e}{m_e c^2}\, d\ell. \tag{2}$$

Here y is the Compton-y parameter, $\sigma_{\rm T}$ is the Thomson scattering cross-section of the electron, and $f(x)$ contains the frequency dependence of the SZE. The integral is along the line of sight. The frequency dependence can be expressed as

$$f(x) = \left(x \frac{e^x + 1}{e^x - 1} - 4 \right) (1 + \delta_{\rm SZE}(x, T_e)) \tag{3}$$

where $\delta_{\rm SZE}(x, T_e)$ is a relativistic correction to the frequency dependence. We adopt the analytic corrections of Itoh et al. (1998) which are good to fifth order in $k_{\rm B}T_e/m_e c^2$. As Eq. [2] shows, the SZE is really just the line of sight integral of the gas pressure and is independent of redshift. Its linear density dependence makes it a complementary probe to the X-ray emission, which goes as n_e^2, and its redshift independence makes the SZE an excellent probe of the high-z universe. The SZE is a thermal decrement at low frequencies and an increment at high frequencies due to the upscattering of photons by the hot electrons.

In addition to the thermal effect, there is a kinetic SZE that arises from scattering of CMB photons in a cluster with line of sight motion, or peculiar velocity V_p, relative to the CMB rest frame. Such scattering gives rise to a Doppler shift which is seen as a distortion of the CMB spectrum, although the kinetic distortion is indistinguishable from primary CMB anisotropy. However, given that it is a minor effect at our observing frequency of 30 GHz (e.g., Reese et al. 2002), it is not treated in this work.

With knowledge of the gas temperature, one can use either S_x or ΔT to solve for the central gas density and integrate over the gas distribution to determine $M_{\rm gas}$. The total mass $M_{\rm total}$ can be determined by assuming that the gas is in hydrostatic equilibrium (HSE) with the cluster potential. The gas mass fraction $f_{\rm gas}$ is then simply $M_{\rm gas}/M_{\rm total}$. Not all baryons reside in the gas, however; there is a baryonic component in stars (e.g., White et al. 1993; Kravtsov et al. 2005) and some hydrodynamical simulations show depletion of baryons during cluster formation (e.g., Evrard 1997). The measured gas mass fraction therefore provides a lower limit to the baryon fraction:

$$f_{\rm gas} \leq f_{\rm B} = \Omega_B/\Omega_M. \tag{4}$$

and the cluster gas mass fraction then provides an upper limit to Ω_M:

$$\Omega_M \leq \Omega_B/f_{\rm gas}. \tag{5}$$

This method has been applied by many authors using X-ray data (e.g., Allen et al. 2002; Mohr et al. 1999; Ettori & Fabian 1999; David et al. 1995; White et al. 1993) and more recently with SZE data as well (Grego et al. 2001; Myers et al. 1997). The results of these studies consistently indicate $\Omega_M \lesssim 0.3$, consistent with measurements of cluster abundances (e.g., Bahcall & Fan 1998) and the CMB (Spergel et al. 2003).

The dark energy density Ω_Λ can be measured by an extension of this method proposed by Sasaki (1996) and Pen (1997). They argue that since the gas mass fraction in clusters reflects Ω_B/Ω_M, and this ratio is generally assumed to be constant with redshift, the gas mass fraction should also be constant with redshift. They then make use of the fact that $D_{\rm A}$ must first be specified in order to deproject the X-ray surface brightness or SZE decrement to solve for $f_{\rm gas}$. Since $f_{\rm gas}$ depends on $D_{\rm A}$, and $D_{\rm A}$ depends on cosmology, the "correct" cosmology is taken to be the one that gives a flat $f_{\rm gas}$ versus z curve. This method is applied by Allen et al. (2002) and Allen et al. (2004), in which they use cluster X-ray data with priors on h and Ω_B to obtain non-zero limits on Ω_Λ. This is a powerful method for testing cosmology since it assumes only that $f_{\rm gas}$ should be constant with redshift. Since the normalization of $f_{\rm gas}$ is not important, a precise understanding of the baryon budget in clusters is not necessary.

We present a sample of 36 massive galaxy clusters with both archival *Chandra* X-ray data and centimeter-wave interferometric SZE data. We perform a maximum likelihood analysis using a Markov chain Monte Carlo method to determine both the gas masses and total gravitational masses of the 36 clusters. The ratio of gas mass to total mass is used to determine Ω_M and Ω_Λ using the methods described above, and the results are compared with those of previous studies. All told, our results provide a better understanding of both cosmology and cluster structure and evolution, as well as associated systematic uncertainties. In §2 we describe the properties of the cluster sample used in this study. The X-ray and SZE observations and data reduction are summarized in §3. In §4 we explain the cluster models and analysis used to extract cosmological parameters from the data, and our results are presented in §5 along with their implications for cosmology and cluster physics. An assessment of major systematic uncertainties is presented in §6. Finally, our conclusions and discussion of future prospects are contained in §7. All uncertainties are at the 68.3% confidence level unless otherwise stated.

2. Sample

The cluster sample consists of objects that have both X-ray data from the *Chandra X-ray Observatory* and SZE data from the BIMA/OVRO SZE imaging project, which uses the Berkeley-Illinois-Maryland Association (BIMA) and Owens Valley Radio Observatory (OVRO) centimeter-wave interferometers to image the SZE. The BIMA/OVRO SZE imaging project has generally pursued hot clusters (published $T_x \gtrsim 5$ keV) which by inference should be massive and have a stronger SZE (Grego 1999; Reese 2001). Hot clusters are also expected to have gas mass fractions more closely resembling the universal value (Mohr et al. 1999; Sanderson et al. 2003).

Most of the clusters in the X-ray/SZE sample come from at least one of four large X-ray catalogs. Clusters are X-ray selected because X-ray emission indicates the presence of a hot intracluster medium (ICM) and the X-ray data, with their n_e^2 dependence, are less prone to chance line of sight superpositions of structure than, e.g., optical data. Three of the catalogs are based on data from the *ROSAT* All Sky Survey (RASS) (Voges 1992): the X-ray Brightest Abell-type Clusters catalog (XBACs, Ebeling et al. 1996b,a) and Brightest Cluster Sample (BCS, Ebeling et al. 1998) consist mainly of low redshift ($z < 0.3$) clusters, while the Massive Cluster Survey (MACS, Ebeling et al. 2001a) consists of luminous, high redshift clusters at $z > 0.3$. The fourth catalog, the *Einstein Observatory* Extended Medium-sensitivity Survey (EMSS, Gioia et al. 1990), uses *Einstein* data and extends to very high redshift, $z > 0.8$. Some clusters not belonging to any of these catalogs are included for reasons of special interest, such as CL 1226.9+3332, the most distant cluster in the sample at $z = 0.890$, which was discovered in the RASS-based Wide-Angle *ROSAT* Pointed Survey (WARPS) (Scharf et al. 1997), and the *ROSAT* source RX J1347.5−1145, which is the most X-ray luminous galaxy cluster known (Schindler et al. 1997).

Clusters chosen for SZE observation are generally selected on the basis of X-ray luminosity, L_x. X-ray survey catalogs typically include all clusters above a certain flux threshold. Selecting by flux, however, could bias the SZE sample toward clusters elongated along the line of sight, and applying a spherical model to the ICM distribution could ultimately bias the derived cosmological parameters. Selecting instead by luminosity alleviates this problem, although it may introduce other biases. For instance, highly relaxed clusters have dense, cool cores with high associated luminosities; these "cool core" clusters are discussed more in §4. Some clusters undergoing major mergers are also expected to have very high luminosities. Such clusters may be preferentially chosen when selecting by luminosity.

Several observational constraints exist in selecting clusters to observe from BIMA and OVRO. For instance, the declination of the observatories limits the lowest observable declination to $\sim -15°$, and the spatial filtering properties of the interferometers limit detections to clusters at redshifts $z \gtrsim 0.15$. Another observational limitation involves radio point sources. The ability to accurately decouple point source flux from cluster signal in interferometric observations depends on the phase stability of the instrument. The present system is capable of removing point sources with beam attenuated fluxes $\lesssim 20$ mJy (Reese 2001), and clusters containing point sources with higher beam attenuated fluxes are not observed. Since a correlation exists between cool core clusters and radio point sources (Burns 1990; Peres et al. 1998), choosing clusters in this way may select against cool core clusters. In addition, point source flux falls off with distance squared whereas the SZE is redshift independent; our sample might therefore be biased toward high-z clusters, whose properties might differ from those of nearby clusters. The potential impact of the selection effects described above on derived cluster properties and cosmology will be discussed in §6.

Two additional cuts are made in compiling the final X-ray/SZE cluster sample: the selected clusters must have publicly available *Chandra* data as of 2004 October, and it must be possible to fit an isothermal β-model to the X-ray surface brightness profiles (see §4.1 for a detailed description of this model). The first criterion is easily satisfied, as the *Chandra* archive now contains several hundred galaxy clusters. The second criterion is more stringent as a cluster must have a smooth gas distribution with a characteristic shape in order to be well-fit by the β-model. Several clusters were rejected due to their highly irregular morphologies, evidence of strong merging activity.

The final cluster sample is shown in Table 1. This is the only place that the full cluster names appear; abbreviations are used in the remainder of this paper. The SZE positions are chosen rather than the X-ray positions since X-ray data, with its n_e^2 dependence, is more sensitive to substructure. The SZE profile is proportional to the gas pressure integrated along the line of sight, and cluster pressure profiles are usually smooth (e.g., Markevitch et al. 2000, 2001). The X-ray 2—10 keV luminosities are also calculated for these clusters using the archived *Chandra* data and are included in Table 1. Many of the clusters have published luminosities in the catalogs described above; however, we consider only the *Chandra* values in the remainder of this work since they are self-consistent, and in general result from longer, pointed exposures and therefore have less uncertainty. Altogether, the list in Table 1 constitutes a statistically large sample covering a wide range in redshift, $0.14 \leq z \leq 0.89$, making it an ideal sample for performing cosmological tests.

Table 1. Cluster Sample

Cluster	z	Central SZ Position (J2000.0) (hh mm ss)	(dd mm ss)	L_x[a] (10^{45} erg s^{-1})	z reference
CL 0016+1609	0.541	00 18 33.3	16 26 04.0	1.87	Stocke et al. (1991)
Abell 68	0.255	00 37 04.0	09 10 02.5	0.73	Struble & Rood (1999)
Abell 267	0.230	01 52 42.3	01 00 26.0	0.37	Struble & Rood (1999)
Abell 370	0.375	02 39 52.4	−01 34 43.8	0.70	Struble & Rood (1999)
MS 0451.6−0305	0.550	04 54 11.6	−03 01 01.3	1.90	Gioia & Luppino (1994)
MACS J0647.7+7015	0.584	06 47 50.2	70 14 56.1	1.59	LaRoque et al. (2003)
Abell 586	0.171	07 32 19.6	31 38 55.3	0.31	Struble & Rood (1999)
MACS J0744.9+3927	0.686	07 44 52.4	39 27 33.2	1.53	LaRoque et al. (2003)
Abell 611	0.288	08 00 56.5	36 03 22.9	0.48	Struble & Rood (1999)
Abell 665	0.182	08 30 58.6	65 50 49.8	0.74	Struble & Rood (1999)
Abell 697	0.282	08 42 57.8	36 21 54.5	1.46	Struble & Rood (1999)
Abell 773	0.217	09 17 53.5	51 43 49.8	0.66	Struble & Rood (1999)
ZwCl 3146	0.291	10 23 37.8	04 11 17.8	1.21	Allen et al. (1992)
MACS J1115+53	0.458	11 15 14.7	53 20 09.9	1.07	Ebeling et al., in prep
MS 1137.5+6625	0.784	11 40 23.1	66 08 05.3	0.33	Donahue et al. (1999)
MACS J1149.5+2223	0.544	11 49 34.9	22 23 54.8	2.03	LaRoque et al. (2003)
Abell 1413	0.142	11 55 17.7	23 24 39.5	0.52	Struble & Rood (1999)
CL 1226.9+3332	0.890	12 26.58.0	33.32 57.9	1.59	Ebeling et al. (2001b)
Abell 1689	0.183	13 11 29.1	−01 20 29.7	1.06	Struble & Rood (1999)
RX J1347.5−1145	0.451	13 47 30.6	−11 45 12.3	3.15	Schindler et al. (1995)
MS 1358.4+6245	0.327	13 59 50.2	62 31 07.0	0.51	Gioia & Luppino (1994)
Abell 1835	0.252	14 01 01.8	02 52 45.6	1.59	Struble & Rood (1999)

3. Data

Data for the 36 cluster sample includes both archival *Chandra* data and 30 GHz SZE data collected at the BIMA and OVRO interferometric arrays. Table 2 shows the total good observing time for the sample for both X-ray (in ks) and SZE (in hrs). Periods of poor observing for which data were rejected are not included in the table. Here we describe the X-ray and SZE data reduction procedures.

Table 1—Continued

Cluster	z	Central SZ Position (J2000.0) (hh mm ss)	(dd mm ss)	L_x[a] (10^{45} erg s^{-1})	z reference
MACS J1423.8+2404	0.545	14 23 47.7	24 04 37.3	0.73	LaRoque et al. (2003)
Abell 1914	0.171	14 26 01.3	37 49 38.6	1.06	Struble & Rood (1999)
Abell 1995	0.322	14 52 58.1	58 02 57.0	0.63	Patel et al. (2000)
Abell 2111	0.229	15 39 40.2	34 25 00.4	0.40	Struble & Rood (1999)
Abell 2163	0.202	16 15 43.6	−06 08 46.6	2.28	Struble & Rood (1999)
Abell 2218	0.176	16 35 48.7	66 12 28.1	0.44	Struble & Rood (1999)
RX J1716.6+6708	0.813	17 16 51.2	67 07 49.6	0.42	Henry et al. (1997)
Abell 2259	0.164	17 20 09.0	27 40 09.4	0.24	Struble & Rood (1999)
Abell 2261	0.224	17 22 26.9	32 07 59.9	0.67	Struble & Rood (1999)
MS 2053.7−0449	0.583	20 56 21.0	−04 37 47.2	0.13	Stocke et al. (1991)
MACS J2129.4−0741	0.570	21 29 24.9	−07 41 43.9	1.29	LaRoque et al. (2003)
RX J2129.3+0005	0.235	21 29 38.1	00 05 12.4	0.58	Ebeling et al. (1998)
MACS J2214.9−1359	0.450	22 14 58.4	−14 00 10.9	1.09	Ebeling et al., in prep
MACS J2228.5+2036	0.412	22 28 33.1	20 37 14.2	1.22	Böhringer et al. (2000)

[a]Calculated using flat cosmology with Ω_Λ=0.73, $h = 0.7$ over 2—10 keV frequency band.

Table 2. Cluster Data

Cluster	*Chandra* X-ray Data ObsID	Chip	Exposure (ks)	Interferometric SZE Data BIMA (hr)	OVRO (hr)
CL0016	520	I3	67.4	43	100
A68	3250	I3	10.0	54	···
A267	1448	I3	7.4	50	···
A370	515	S3	65.3	26	33
MS0451	902	S3	42.2	···	30
MC0647	3196	I3	19.3	···	23
	3584	I3	20.0	···	···
A586	530	I3	10.0	45	···
MC0744	3197	I3	20.2	8	17
	3585	I3	19.4	···	···
A611	3194	S3	36.1	···	57
A665	531	I3	9.0	52	16
	3586	I3	29.7	···	···
A697	4217	I3	19.5	···	47
A773	533	I3	11.3	26	66
	3588	I3	9.4	···	···
Zw3146	909	I3	46.0	25	15
MC1115	3253	I3	8.8	···	15
MS1137	536	I3	77.0	88	···
MC1149	1656	I3	18.5	39	···
	3589	I3	20.0	···	···
A1413	537	I3	9.6	28	···
	1661	I3	9.7	···	···
CL1226	3180	I3	31.7	33	···
A1689	540	I3	10.3	16	26
	1663	I3	10.7	···	···
R1347	3592	I3	57.7	22	3
MS1358	516	S3	48.1	70	···
A1835	495	S3	19.5	27	23

3.1. *Chandra* X-ray Data

The X-ray data are reduced using the Chandra Interactive Analysis of Observations (CIAO) 3.1 software package with CALDB 2.28. Details of the data reduction procedure are given in Bonamente et al. (2004); briefly, we run the CIAO routine *acis_process_events* on the level 1 events file to correct for charge transfer inefficiency (CTI) in the front-illuminated (FI) chips (Townsley et al. 2000). This file is then filtered on grade, bad pixels, and good time intervals to produce the level 2 events file. The CIAO routine *lightcurve* is used with a 500 s bin size to create a histogram of count rate versus time. We exclude data corresponding to any bin in which the count rate is more than 4σ above the mean. This procedure is performed iteratively until no bins remain with a count rate greater than 4σ above the mean.

The filtered level 2 events file is then used to make images of each chip relevant to the observation, typically chips I0—I3 for ACIS-I and S3 for ACIS-S. X-ray backgrounds are extracted from appropriate cluster-free regions of these chips; see Bonamente et al. (2004) for a detailed description of the background analysis. The images are binned by four to a pixel size of $1''.96$ to increase signal to noise, and are also filtered on energy to contain photons in the range 0.7—7.0 keV. All spatial analysis is performed on these binned images. Instrument and exposure maps are created using *mkinstmap* and *mkexpmap*; as of CIAO version 3.1, *mkinstmap* applies a time-dependent correction for the increased QE of the ACIS chips due to buildup of a molecular contaminant on the ACIS optical blocking filter.

Cluster spectra are extracted from a circular region centered on the cluster containing roughly 95% of the cluster counts. The spectrum itself is extracted from the 0.7—7.0 keV band with the CIAO script *acisspec*, which generates the raw count rate file as a function of energy, the ancillary response file (ARF), and response matrix file (RMF). The *mkwarf* routine, called by *acisspec* to extract the weighted ARF, includes a time-dependent correction for the ACIS contamination buildup. However, it does not account for the spatial variation of the contaminant across the optical blocking filter. This is done using with the routine *calcarf*, which applies a second-order spatial correction to the first-order temporal correction applied by *mkwarf*. This newer calibration also differs considerably from that used by *mkinstmap*. To account for the more recent calibration in the instrument maps, we calculate the weighted mean spectral response at 1 keV using the latest correction and compare it with the 1 keV response under the old calibration to get the appropriate scale factor $s_{\rm instmp}$, which is applied to the spatial data as described in §4.3. Spectra are grouped to contain a minimum of 25 counts per energy bin so that Gaussian statistics can be used in the spectral fitting. The routine *dmextract* is used to create a background spectrum, using the same background regions used in the image analysis. The software package XSPEC (Arnaud 1996) is used to fit a model to the spectrum and determine the emission-weighted temperature and metallicity

Table 2—Continued

	Chandra X-ray Data			Interferometric SZE Data	
Cluster	ObsID	Chip	Exposure (ks)	BIMA (hr)	OVRO (hr)
	496	S3	10.7	···	···
MC1423	4195	S3	115.6	35	···
A1914	542	I3	8.1	24	···
	3593	I3	18.9	···	···
A1995	906	S3	56.7	50	58
A2111	544	I3	10.3	36	···
A2163	1653	I1	71.1	23	37
A2218	1666	I0	41.7	32	70
R1716	548	I3	51.7	37	···
A2259	3245	I3	10.0	25	···
A2261	550	I3	9.1	23	40
MS2053	551	I3	44.3	···	154
	1667	I3	44.5	···	···
MC2129	3199	I3	8.5	···	24
	3595	I3	18.4	···	···
R2129	552	I3	10.0	47	···
MC2214	3259	I3	19.5	41	11
	5011	I3	16.1	···	···
MC2228	3285	I3	19.9	39	···

of the cluster.

3.2. SZE Data

All SZE data were obtained at the BIMA and OVRO interferometers between 1995 and 2002. Interferometry provides a means of observing clusters with very low noise and well-controlled systematics. An interferometer measures the Fourier transform of the sky brightness distribution modified by the primary beam of the telescope, which sets the field of view. The interferometric data are therefore best described in the Fourier plane, also known as the u-v plane where u and v are the Fourier conjugate variables to the sky position variables x and y. The effective resolution of the interferometer is determined by the synthesized beam, which is the Fourier transform of a sampling function $S(u,v)$, which is unity at positions in the u-v plane that are sampled by a projected baseline and zero elsewhere. This means that the telescope configuration can be optimized to achieve maximum sensitivity on the spatial scales of interest. The smallest observable angular scale is determined by the maximum separation between elements. The largest observable scale is determined by the smallest separation, which depends on the diameter D of the telescope dishes. This limiting scale is roughly $\lambda/2D$, which is $\sim 2\farcm8$ at BIMA and $\sim 1\farcm7$ for OVRO.

Our 30 GHz observations were carried out at BIMA and OVRO between 1994 and 2002. BIMA consists of nine 6.1 m diameter dishes while OVRO consists of six 10.4 m diameter dishes. The primary beams are measured holographically, but are well approximated by Gaussians with FWHM $6\farcm6$ for BIMA and $4\farcm2$ for OVRO at 28.5 GHz. The telescopes are outfitted with centimeter-wavelength receivers specifically designed and built to detect the SZE in distant clusters (Carlstrom et al. 1996). The receivers use cryogenically cooled high electron mobility transistor (HEMT) amplifiers (Pospieszalski et al. 1995) sensitive to radio frequencies (RF) between 26 and 36 GHz with typical receiver temperatures in the range 11–20 K. Typical system temperatures (scaled to above the atmosphere) for the SZE observations range between 45 and 55 K. At BIMA the output corresponds to an 800 MHz wide channel centered at an observing frequency of 28.5 GHz. The OVRO output corresponds to two 1 GHz wide channels centered at observing frequencies of 28.5 GHz and 30 GHz. Clusters are generally observed in a compact configuration to maximize sensitivity on cluster scales. However, at least two telescopes are placed at outlying locations to create long baselines for point source sensitivity. Cluster measurements are interleaved with short observations of some bright, nearby radio point source every 25 minutes in order to monitor the amplitude and phase gains of the system. The system temperatures are also measured between observations of the cluster and gain calibrator so as to carefully monitor the system noise. When visible, observations of Mars are used for absolute flux calibration. The true flux of Mars is taken from the model of Rudy (1987), and the fluxes of the gain calibrators are calibrated against this predicted flux.

The interferometric data are reduced using the MIRIAD software package (Sault et al. 1995) at BIMA and the MMA software package (Scoville et al. 1993) at OVRO. We remove data that are not bracketed in time by observations of a gain calibrator, data that show evidence of high atmospheric noise or artificial correlations, data from baselines where one telescope dish partially obscures another, and data corresponding to erroneous system temperature measurements. The program DIFMAP (Pearson et al. 1994) is used to create images from the u-v data which can be studied to estimate positions and fluxes for point sources and clusters.

Figure 1 shows SZE contours overlaid on smoothed *Chandra* X-ray images for all 36 clusters in our sample. The X-ray images are raw counts images which have been smoothed using a Gaussian kernel with $\sigma = 2''$. The wedge at the top of each panel indicates the smoothed count rate for the image. In some cases extremely bright X-ray point sources significantly distort the color scale of the images; in such cases the point sources are masked out from the images prior to smoothing. The SZE contours are at the 2σ level, and come from cluster images created in DIFMAP with a Gaussian taper of half-power radius 1 kλ for BIMA data and 2 kλ for OVRO applied. The white ellipses indicate the FWHM and position angles of the restoring synthesized beams.

4. Analysis Methods and Modeling

To calculate gas mass fractions, we fit a parameterized model of the ICM to the cluster data. Here we introduce and compare results from three models that describe the gas density distribution in clusters, and show how these models can be used to derive masses for the clusters in our sample. Next we describe how the model fitting and likelihood analysis are performed, then demonstrate how one of the models can be applied more consistently than the others.

4.1. Cluster Density Models

We begin with a spherical β-model (Cavaliere & Fusco-Femiano 1976, 1978) of the form

$$n_e(\mathbf{r}) = n_{e_o} \left(1 + \frac{r^2}{r_c^2}\right)^{-3\beta/2}, \tag{6}$$

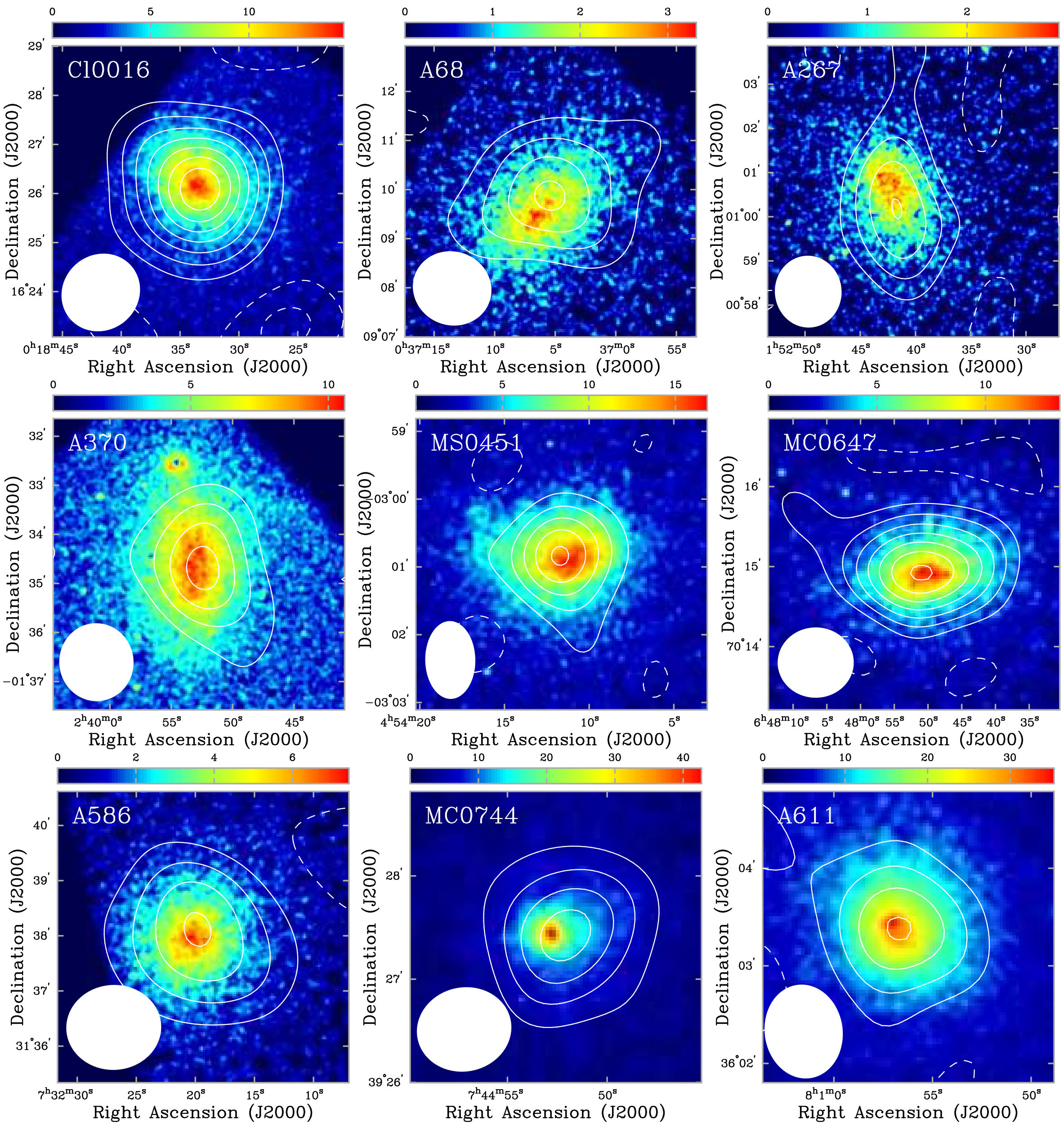

Fig. 1.— SZE (contours) and X-ray (color) images of each cluster in our sample. Negative contours are shown as solid lines. The contours are multiples of 2 σ and the FWHM of the synthesized beams are shown in the bottom left corner. The X-ray color images are raw counts images smoothed with Gaussians with $\sigma = 2''$. X-ray point sources that significantly alter the image statistics have been masked out before smoothing.

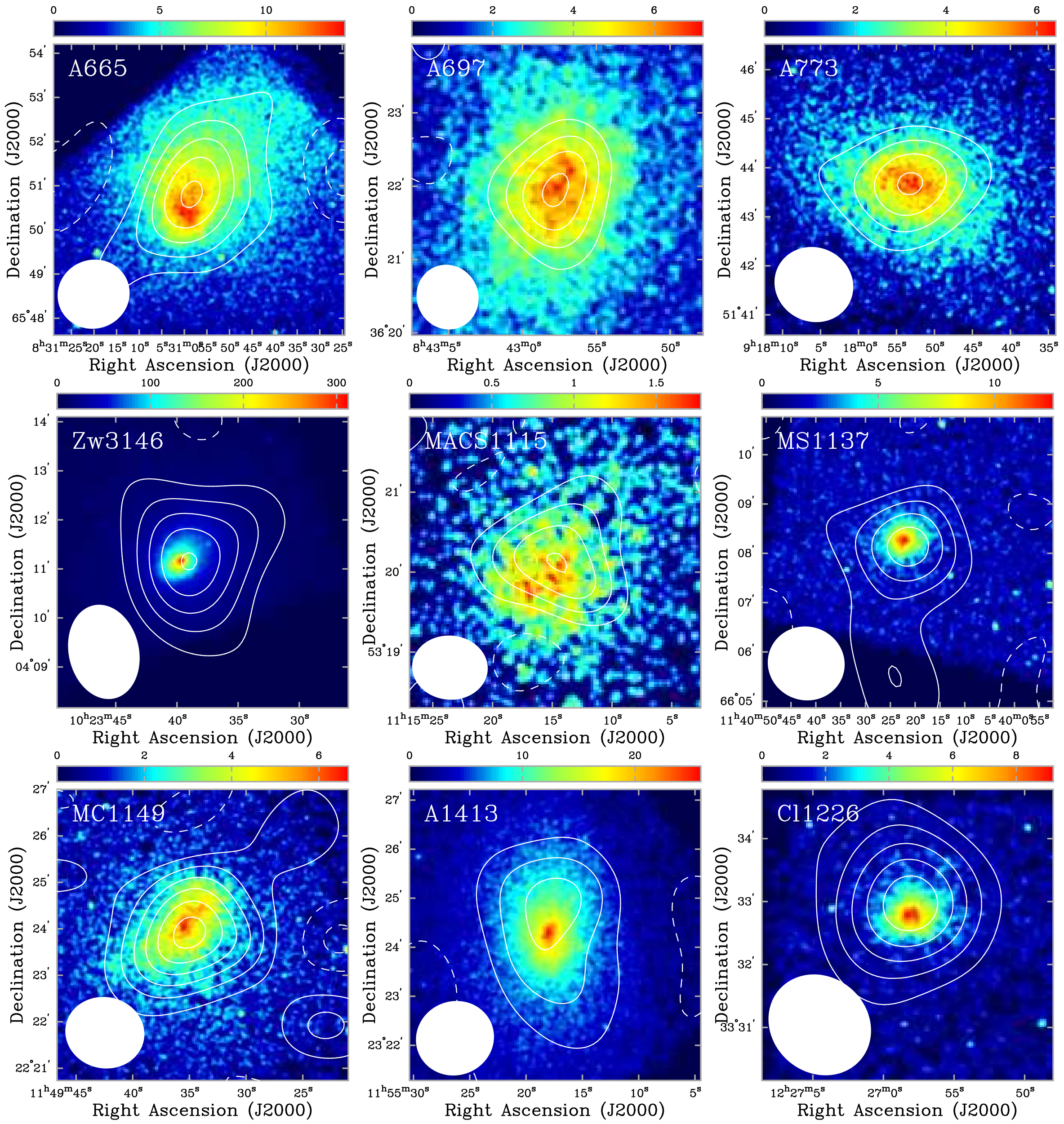

A665
A697
A773
Zw3146
MACS1115
MS1137
MC1149
A1413
Cl1226
Declination (J2000)
Right Ascension (J2000)

Fig. 1.— Cont.

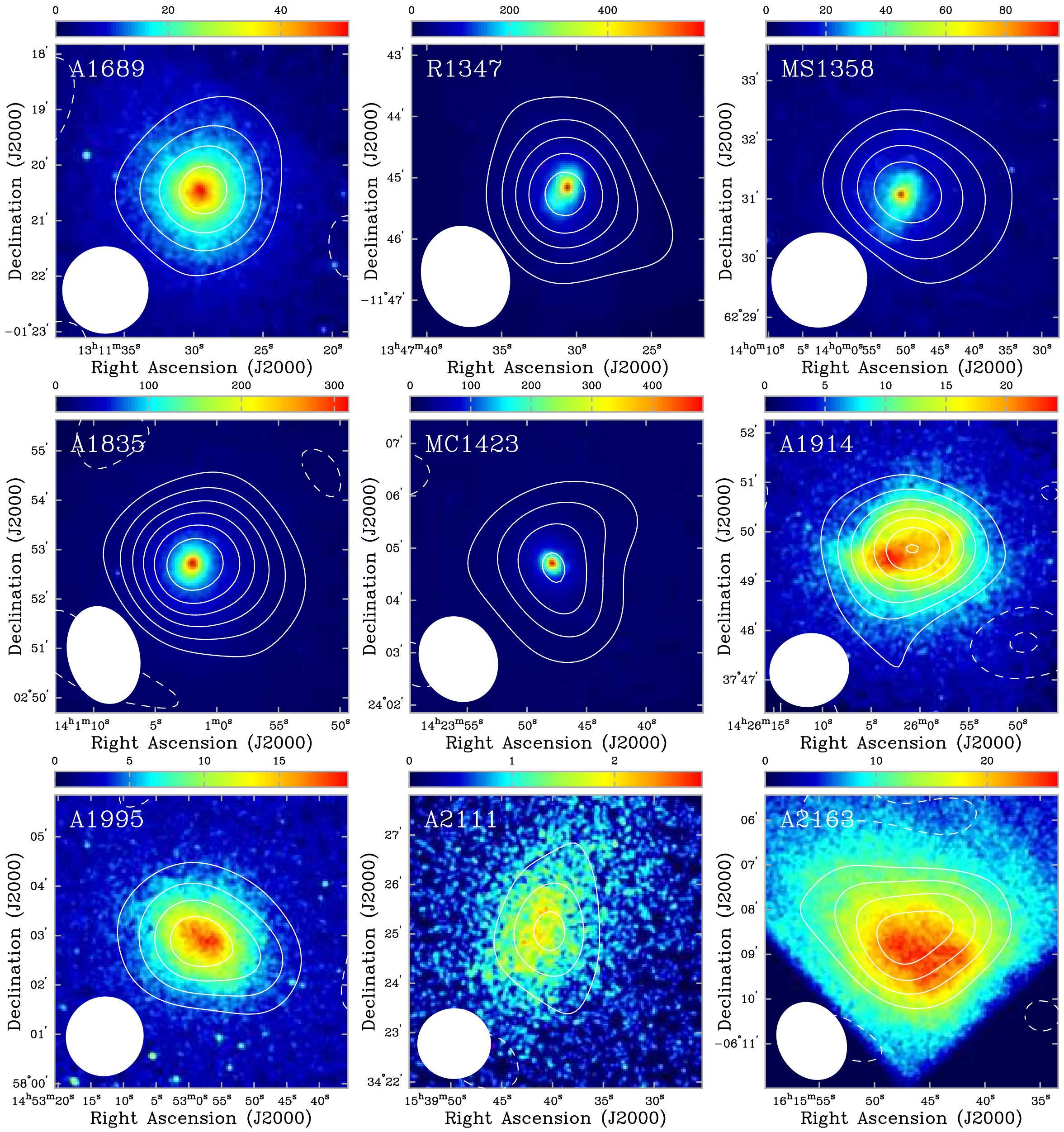

A1689
R1347
MS1358
A1835
MC1423
A1914
A1995
A2111
A2163
Declination (J2000)
Right Ascension (J2000)

Fig. 1.— Cont.

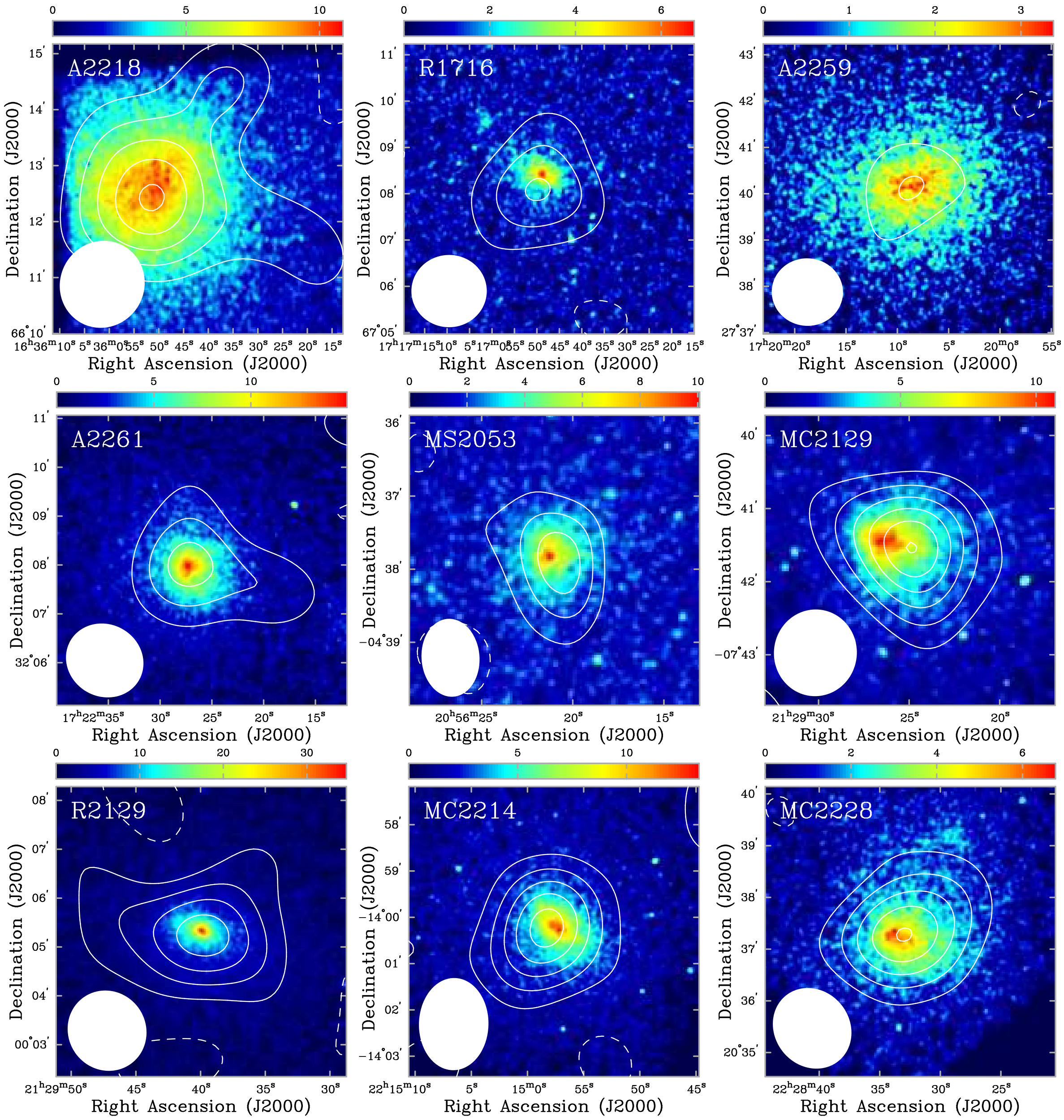
A2218
R1716
A2259
A2261
MS2053
MC2129
R2129
MC2214
MC2228
Declination (J2000)
Right Ascension (J2000)

Fig. 1.— Cont.

where n_e is the electron number density, r is the radius from the center of the cluster, r_c is the core radius of the ICM, and β is a power law index. The main advantage of this model is that the integrals in Eqs. [1] and [2] have analytic solutions when Eq. [6] is used to describe the density profile and a constant temperature is assumed. The model is typically referred to as the isothermal β-model under these conditions. The isothermal β-model has been shown to provide excellent fits to X-ray surface brightness and SZE decrement profiles in most cases (e.g., Jones & Forman 1984; Elbaz et al. 1995; Grego et al. 2001; Reese et al. 2002; Ettori et al. 2004), although simulations indicate that cluster density profiles steepen in their outer regions so the model should not be extrapolated beyond radii to which the data are sensitive (e.g., Borgani et al. 2004).

Substituting Eq. [6] for n_e in Eq. [1] gives the solution (Birkinshaw et al. 1991)

$$S_x = S_{x0}\left(1+\frac{\theta^2}{\theta_c^2}\right)^{(1-6\beta)/2}, \tag{7}$$

where S_{x0} is the central X-ray surface brightness and θ_c is the angular core radius of the cluster. The SZE case is analogous to the X-ray case; the SZE signal of Eq. [2] combined with Eq. [6] can be written as (Birkinshaw et al. 1991)

$$\Delta T = \Delta T_0\left(1+\frac{\theta^2}{\theta_c^2}\right)^{(1-3\beta)/2} \tag{8}$$

where ΔT_0 is the central thermodynamic SZE temperature decrement/increment.

One class of clusters which must be dealt with differently consists of those with dense, cool cores. These tend to be relaxed systems for which the HSE assumption should be reasonable, so cool core clusters are expected to give the most consistent mass results. The gas temperature in such systems is found to decrease in the center by at least a factor of three relative to the outer regions (e.g., Fabian 2003). However, because the density is so high the X-ray surface brightness is sharply peaked in the center and the isothermal β-model is a poor description of these clusters. Ten of the 36 clusters in our sample strongly demonstrate these cool core properties, and it is desireable to have a model which adequately describes them.

In Mohr et al. (1999), the authors find that including a second β-model component that accounts for the sharply peaked inner core provides enough freedom to fit the outer regions and the central emission excess of a cool core cluster simultaneously. Generalizing their approach and expressing the double β-model directly in terms of the density components, we write

$$n_e(\mathbf{r}) = n_{e_o}\left[f\left(1+\frac{r^2}{\theta_{c_1}^2}\right)^{-3\beta/2} + (1-f)\left(1+\frac{r^2}{\theta_{c_2}^2}\right)^{-3\beta/2}\right] \tag{9}$$

where the two core radii, θ_{c_1} and θ_{c_2}, describe the narrow, peaked central density component and the broad, shallow outer density profile, respectively, and f represents the fractional contribution of the narrow, peaked component to the central density n_{e_o} ($0 \leq f \leq 1$). Following Mohr et al. (1999) we use one β for both density components, thereby reducing the degrees of freedom in the fit to tighten the constraints on the other parameters. Tests that include a second β show no significant difference in the fits relative to the one-β case. The density profile in Eq. [9] is combined with a trial temperature profile and the best-fit abundance profile from De Grandi et al. (2004), then integrated along the line of sight in Eqs. [1] and [2] to obtain the X-ray surface brightness profile and SZE decrement profile to compare with the data. The X-ray cooling function is a very weak function of Z, and varying this De Grandi et al. abundance profile within the model uncertainties makes a difference of less than 1% in the cluster mass.

The temperature profiles are solved for iteratively assuming a gas density distribution described by Eq. [9] in HSE with a "universal" NFW dark matter density distribution (Navarro et al. 1997). Assuming an ideal gas equation of state and spherical symmetry, the gas temperature gradient can be written

$$\frac{dT}{dr} = -\left[\frac{\mu m_p}{k_{\rm B}}\frac{d\phi(r)}{dr} + \frac{T(r)}{\rho(r)}\frac{d\rho_g(r)}{dr}\right] \tag{10}$$

where μ is the mean molecular weight of the gas, $k_{\rm B}$ is Boltzmann's constant, m_p is the proton mass, $\rho_g(r)$ is the mean gas density at radius r, and $\phi(r)$ contains contributions from both the gas and dark matter. For the dark matter, we assume an NFW density distribution of the form (Navarro et al. 1996, 1997)

$$\frac{\rho_{\rm DM}(r)}{\rho_{\rm crit}(z)} = \frac{\delta_c}{(r/r_s)(1+r/r_s)^2} \tag{11}$$

derived from numerical simulations. Here $\rho_{\rm crit}(z)$ is the critical density of the universe at redshift z, $r_s = r_{200}/c$ is a characteristic radius known as the scale radius, and c is called the concentration parameter. The parameters δ_c and c are dimensionless and are linked by the requirement that the mean density within r_{200} be $200 \times \rho_c$:

$$\delta_c = \frac{200}{3}\frac{c^3}{\ln(1+c) - c/(1+c)}. \tag{12}$$

Putting all of this information into Eq. [10], we use a fourth-order Runge-Kutta method (Press et al. 1992) to solve for the true temperature profile $T_e(r)$ of the cluster. Based on the results of Vikhlinin et al. (2004), the temperature at radius r_{200} is held fixed at 10% of the "average" cluster temperature, which Vikhlinin et al. define as the mean emission-weighted temperature excluding the central 70 kpc. The Runge-Kutta then proceeds iteratively from

r_{200} to the cluster center to solve for $T_e(r)$. This temperature profile is then integrated along the line of sight weighted by Eq. [9] to determine the emission-weighted temperature profile, and this is compared with a temperature profile extracted from the *Chandra* data.

Ultimately the parameters fit to the combination of spatial and spectral data for the non-isothermal double β-model are the dark matter shape parameters r_{200} and c, and the ICM parameters n_{e_o}, θ_{c_1}, θ_{c_2}, β, and f. This approach allows sufficient freedom in the shape of the surface brightness and temperature profiles to obtain good fits to the cool core cluster data.

Not all of the cool core clusters in our sample have data of sufficient quality that we can extract temperature profiles and fit this double β-model, and many non-cool core clusters have significant substructure in their cores (e.g., Markevitch et al. 2003b) which cannot be described by either of the models above. We therefore propose a third model, which is simply the single isothermal β model with the central 100 kpc excised from the X-ray data (the SZE data are dealt with somewhat differently, as will be explained below). This is consistent with the treatments of, e.g., Majerowicz et al. (2002) who mask out the core of A1835 in studying its gas mass fraction, and Vikhlinin et al. (2004) who exclude the inner 70 kpc when extracting temperature profiles from a sample of 11 relaxed clusters. We choose the 100 kpc limit because our sample, being selected for optimal SZE observing, contains larger, more massive clusters than Vikhlinin's. With the 70 kpc cut, several cool core clusters do not have their cooling regions entirely excluded, leading to biased results for θ_c and β. Pushing the cut above 100 kpc, several clusters in our sample no longer have a sufficient number of counts to be fit by a β-model of any sort.

All the same analytic equations that apply to the single isothermal β-model still apply when the central 100 kpc are excluded, and this model can be applied to all clusters in the sample allowing a consistent analysis of the entire data set. Furthermore, it is well-motivated physically by several factors. The observational results of Markevitch et al. (2003b) indicate that HSE may be a poor assumption within a 100 kpc radius, even in relaxed clusters. As will be shown, total cluster masses are calculated assuming HSE, so this model treats only the regions most likely to satisfy this condition. Additionally, Vikhlinin et al. (1999) show that when the cooling regions of cool core clusters are excluded, their density profiles are similar in shape to those of non-cool core clusters, so applying this single model to both types of clusters should be appropriate. Finally, simulations indicate that while there is considerable variation in core behavior from cluster to cluster, density and temperatures profiles are reasonably self-similar outside cluster cores, over a range of masses and dynamical states (e.g., Kravtsov et al. 2005). The disadvantage of this model is that it does not model the entire cluster profile, but instead extrapolates the density profile into the central 100 kpc.

However, as will be shown, the central 100 kpc contributes little to the mass measured on the scales to which the *Chandra* and BIMA/OVRO data are sensitive.

There is no simple way to excise the central 100 kpc from the interferometric SZE data because these data are fit in the Fourier plane. In analyzing the SZE data, we therefore fit the entire SZE dataset and use the 100 kpc-cut emission weighted temperature. Since the SZE depends only linearly on the density, it is less sensitive to behavior in the dense core than are the X-ray data. Additionally, even clusters with significant core substructure are frequently found to be in pressure equilibrium (e.g., Markevitch et al. 2000, 2001) and should therefore have smooth SZE profiles. Using the 100 kpc-cut X-ray values of θ_c and β in the SZE analysis should therefore be appropriate. Furthermore, upcoming SZE cluster surveys (references here) will generally not have the benefit of high-resolution X-ray followup observations to assess the amount of substructure in cluster cores. Comparison of the X-ray and SZE results should help determine how significant of an effect substructure might have on the SZE results.

4.2. Calculating Cluster Properties from the Models

Ultimately we would like to determine the gas mass fraction $f_{\rm gas} = M_{\rm gas}/M_{\rm total}$ using both the X-ray and SZE data for the 36 clusters in our sample. These calculations are shown here for the models described above.

Under the assumptions of the isothermal β-model, the central electron density n_{e_o} can be expressed analytically as (Birkinshaw et al. 1991):

$$n_{e_o} = \left(\frac{S_{x0}\, 4\pi (1+z)^4\, \frac{\mu_H}{\mu_e}\, \Gamma(3\beta)}{\Lambda_{e\rm H} D_{\rm A} \pi^{1/2}\, \Gamma(3\beta - \frac{1}{2})\, \theta_c} \right)^{1/2} \tag{13}$$

Since the density profile is known from Eq. [6], the gas mass at radius r can be obtained (e.g., Patel et al. 2000):

$$M_{\rm gas}(r) = A \int_0^{r/D_{\rm A}} \left(1 + \frac{\theta^2}{\theta_c^2}\right)^{-3\beta/2} \theta^2 d\theta, \tag{14}$$

where $A = 4\pi \mu_e n_{e_o} m_p\, {D_{\rm A}}^3$ and μ_e is calculated using the elemental abundances derived from the X-ray spectral data. Note that the angular diameter distance $D_{\rm A}$ must be known in order to solve for the gas mass, and therefore a specific cosmology (Ω_M, Ω_Λ, h) must be assumed.

The total mass, $M_{\rm total}$, follows from the assumptions of ideal gas pressure, isothermality, and HSE (Grego et al. 2001):

$$M_{\rm total}(r) = \frac{3\beta kT_e}{G\mu m_p}\frac{r^3}{r_c^2+r^2}. \tag{15}$$

The X-ray gas mass fraction follows from dividing the results of Eq. [14] by Eq. [15].

Calculating $M_{\rm gas}$ from the SZE data is very similar to the X-ray case. For the SZE, the central electron density can be expressed as (e.g., Grego et al. 2001):

$$n_{e_o} = \left(\frac{\Delta T_0\, m_e c^2\, \Gamma(\frac{3}{2}\beta)}{f_{(x,T_e)} T_{\rm CMB}\sigma_{\rm T}\, k_{\rm B}T_e D_{\rm A}\pi^{1/2}\,\Gamma(\frac{3}{2}\beta-\frac{1}{2})\,\theta_c}\right) \tag{16}$$

We can then use Eq. [14] to derive the gas mass at a radius r_0. As with the X-ray data, $D_{\rm A}$ must be specified to solve for the gas mass. Derivation of the total mass and subsequently the SZE gas mass fraction follows using Eq [15].

Calculating the mass of cool core clusters fit with the non-isothermal double β-model is straightforward since in the double β-model case we fit for the central electron density n_{e_o} directly. To obtain the gas mass from the quantities n_{e_o}, f, β, θ_{c_1}, and θ_{c_2}we simply integrate Eq. [9] over the spherical distribution out to the desired radius r:

$$M_{\rm gas}(r) = A\int_0^{r/D_{\rm A}}\left[f\left(1+\frac{\theta^2}{\theta_{c1}^2}\right)^{-3/2\beta} + (1-f)\left(1+\frac{\theta^2}{\theta_{c2}^2}\right)^{-3/2\beta}\right]\theta^2\,d\theta, \tag{17}$$

where A is defined as above. Note that μ_e is actually a function of r since the metal abundance ratio Z is no longer assumed constant in this model. However, since μ_e changes by only 0.3% over the radius range considered it is removed from the integral and treated as a constant.

The total mass is solved for by assuming that it is simply the sum of the gas mass (Eq. [17]) and the mass of the underlying dark matter, $M_{\rm DM}$. An analytic form for $M_{\rm DM}$ is given by Klypin et al. (2001),

$$M_{\rm DM}(r) = 4\pi\rho_c\,\delta_c\,r_s^3\left[\ln(1+r/r_s) - \frac{r}{r_s(1+r/r_s)}\right], \tag{18}$$

and the total mass then follows immediately. Since the temperature and gas profiles were determined assuming HSE with the dark matter potential, this calculation of total mass is consistent with the HSE method used for the single isothermal β-model.

Calculation of cluster masses using the 100 kpc cut model for the X-ray data follows the same procedures used for the single isothermal β-model, as described above. The central

100 kpc are simply excluded when the X-ray spatial and spectral data are fit, so masses are extrapolated into the cluster centers. The impact of this extrapolation on the results will be investigated in §4.4.

Mass results from these three different models are compared in §4.4. First, however, we investigate how these models are actually fit to the X-ray and SZE data so that masses can be inferred.

4.3. Model Fitting and Likelihood Analysis

Best-fit model parameters and confidence intervals are obtained using a Markov chain Monte Carlo (MCMC) method which efficiently handles the large number of parameters involved in the model fitting. Implementation of a MCMC method for determining the angular diameter distance to the cluster A611 from SZE and X-ray data is described in detail in Bonamente et al. (2004). The Markov chain is constructed by starting with a parameter set $\mathbf{\Theta}$ and either accepting it into the chain or rejecting it based on the Metropolis-Hastings acceptance algorithm (Metropolis et al. 1953; Hastings 1970; Christensen et al. 2001; Gilks et al. 1996). Additional parameter sets are tested randomly from within a specified proposal distribution about the current $\mathbf{\Theta}$; we take this distribution to be a simple top hat function. When a sufficiently large number of parameters are accepted, the frequency of their occurence in the chain approaches the true probability distribution function for each parameter (Gamerman 1997; Gilks et al. 1996).

The range to be explored or support for each parameter is determined from test runs of the Markov chain using very broad parameter limits. By testing proposal distribution widths from 10% to 50% of the parameter support and calculating the number of iterations needed for convergence of the Markov chain, we find an optimal proposal distribution width of $\sim 20\%$ of the parameter support, and adopt this value for the top hat.

Testing for convergence to the true probability distribution is extremely important, as a chain which has not converged will give incorrect results. Convergence is tested for using the Raftery-Lewis diagnostic (Raftery & Lewis 1992; Gilks et al. 1996) and the Gelman-Rubin diagnostic (Gelman & Rubin 1992); the Raftery-Lewis diagnostic also estimates the number of iterations required to determine confidence intervals to a desired accuracy. We find that for a typical cluster, no more than 10^5 iterations are needed to produce probability density functions that give 90% confidence intervals at 98% accuracy (Bonamente et al. 2004). We perform the Raftery-Lewis test on each chain to ensure that it has converged and is accurately reporting 90% confidence intervals. The Gelman-Rubin diagnostic tests for another desired property of a Markov chain, known as "mixing." The chain cannot tell anything about areas of the parameter space that it has not covered. An ideal chain will therefore move rapidly throughout the space, and such a chain is said to have achieved good mixing. Poor mixing, often a result of using too small a proposal distribution, may cause the chain to get stuck in a small area of parameter space and take a very long time to explore the entire likelihood surface. A poorly mixed chain with highly correlated neighboring steps may appear to have converged to the final distribution before it has actually done so (e.g., Verde et al. 2003). Running the Gelman-Rubin test on the cluster A611 (Bonamente et al. 2004), it was found that good mixing is achieved after $\sim 10^4$ iterations. Since the Raftery-Lewis results indicate that 10^5 iterations are typically required to achieve the desired accuracy on confidence intervals, poor mixing should not be a problem.

The X-ray, SZE, and spectral datasets are generally combined for best results. In jointly fitting these datasets, we take advantage of the fact that they are independent and the likelihoods for each dataset can simply be multiplied together to construct a joint likelihood. The easiest approach is to work with log likelihoods, which for spatial fitting to X-ray and SZE images can be written (Cash 1979; Reese et al. 2002)

$$\sum_i D_i \ln(M_i) - M_i \qquad \text{for X-ray data (Poisson)}, \tag{19}$$

$$\sum_i -\frac{1}{2}\left(\Delta R_i^2 + \Delta I_i^2\right) W_i \qquad \text{for SZE data (Gaussian)}, \tag{20}$$

where M_i and D_i are the model prediction and data in pixel i, while ΔR_i^2 and ΔI_i^2 are the difference between the real and imaginary components of the data and model at each point i in the Fourier plane and $W_i = 1/\sigma^2$ is a measure of the Gaussian noise. Calculation of the spectral log likelihood is done with XSPEC. The spatial and spectral log likelihoods are then added together to compute the joint log likelihood (Bonamente et al. 2004). We examine the likelihood calculation for the spatial and spectral data in the context of the isothermal β-model, which is trivially extended to the 100 kpc-cut β-model. The likelihood calculation for the non-isothermal double β-model is also described.

In the case of the single isothermal β-model, the X-ray model consists of a β-model (Eq. 7) plus a constant cosmic background, B_x. Free parameters in the fit include the two-dimensional cluster position, central surface brightness S_{x0}, θ_c, and β. The model is calculated at each pixel position then multiplied by the exposure map before being compared with the image. The Poisson log likelihood is computed using Eq. [19], and the best-fit S_{x0} is then scaled by the factor $s_{\rm instmp}$ of §3.1 to account for the most recent calibration.

X-ray point sources and any obvious substructure or "clumps" are masked out and the masked pixels are ignored in the likelihood calculation. Likewise, in the 100 kpc-cut fits, any pixels within 100 kpc of the cluster center are ignored; the 100 kpc radius is generally calculated assuming a ΛCDM cosmology with Ω_M=0.3, Ω_Λ=0.7, and h=0.7. The background is determined using the methods described in §3.1. B_x is fixed to avoid degeneracies with S_{x0} that can lead to poorly constrained results; the systematic uncertainty associated with a fixed background is addressed in §6.2.

The spectral likelihoods are calculated using χ^2 information from XSPEC. A photoabsorbed Raymond-Smith thermal plasma model (Raymond & Smith 1977) is fit to the 0.7—7.0 keV X-ray spectral data, with HI column density fixed at the value from Dickey & Lockman (1990) and solar abundances from Feldman (1992). XSPEC is used to create a table of T_e and Z values versus log likelihood for the spectral model using the relation $\ln \mathcal{L} = -\frac{1}{2}\chi^2$.

The interferometric SZE data are analyzed directly in the Fourier plane, where the noise characteristics and spatial filtering of the interferometer are well understood. The composite SZE model consists of an isothermal β-model and any point sources detected in the field. The parameters of interest are the two-dimensional cluster position, ΔT_0, θ_c, and β and the positions and fluxes of any point sources. If SZE datasets from different years exist for a given cluster, all parameters are linked between datasets except the point source fluxes; this accounts for temporal and spectral variability of the fluxes. The SZE β-model is constructed in the image plane, multiplied by the primary beam, then fast Fourier transformed to the u-v plane for comparison with the data. Eq. [20] is used to calculate the Gaussian log likelihood.

For each cluster in the single β-model analysis, we perform two different fits. The first is to the SZE and X-ray data jointly, in which θ_c and β are linked between X-ray and SZE datasets (Reese et al. 2000), and an X-ray spectral model is included as well (Bonamente et al. 2004). The SZE data do not have the spatial resolution to constrain θ_c and β well individually (Grego et al. 2001), so the X-ray dataset drives the fit to these parameters while ΔT_0 and the cluster position are allowed to find their best-fit values. In the 100 kpc-cut case, the central 100 kpc are excluded from the X-ray data but not the SZE data. This provides an interesting check of systematics due to substructure in cluster cores. The second fit is to the SZE data only, providing an additional check of cluster systematics. The procedure for SZE only fitting is described in §4.5.

A convenient property of MCMC analysis is that the chains can be used to determine the probability distributions of functions of other parameters in the chain. The parameters $\Lambda_{e\mathrm{H}}$, n_{e_o}, M_{gas}, M_{total}, and $f_{\mathrm{gas}}$are calculated at each step in the Markov chain using the current values of S_{x0}, ΔT_0, θ_c, β, T_e and Z, so probability histograms for these inferred parameters are computed as well.

The likelihood calculation for the non-isothermal double β-model is slightly different from that described above. For the X-ray data the integral in Eq. [1] is done numerically in one dimension at spacings equal to one half the pixel size to ensure sufficient sampling. Cubic spline interpolation (Press et al. 1992) is then used to fill out the pixel grid. The pixel grid is multiplied by the exposure map and compared with the *Chandra* data, and the likelihood is calculated using Eq. [19]. The likelihood calculation for the SZE data is similar; the integral in Eq. [2] is calculated numerically at spacings equal to one half the pixel size, which is determined by the smallest spatial scale (largest u-v spacing) to which the interferometer is sensitive. Interpolation is then performed to fill out the two dimensional grid which is Fourier transformed and compared with the data in Fourier space. In theory, the line of sight integrals extend from minus infinity to infinity, but in practice they are cut off at r_{200}, which is a free parameter in the fit. Typical values of r_{200} are ~ 2 Mpc. The gas density at r_{200} is several orders of magnitude lower than the central value, and numerical simulations suggest that it falls off as r^{-3} beyond r_{200}, as opposed to the shallower r^{-2} suggested by the β-model with $\beta \sim 2/3$ (Frenk et al. 1999; Navarro et al. 1997). The gas should therefore make very little contribution to the integrals beyond r_{200}. X-ray and SZE data are always fit jointly with θ_{c_1}, θ_{c_2}, and β linked between models. The SZE data do not have sufficient resolution to constrain all three parameters individually. The density profile of Eq. [9] is combined with a model temperature profile and, in the X-ray case, the abundance profile from De Grandi et al. (2004) to perform the integrals of Eqs. [1] and [2].

A spectral likelihood is also calculated for the non-isothermal temperature profiles and included in the total likelihood calculation. Emission-weighted temperature profiles are constructed by extracting spectra from concentric annular regions in the *Chandra* data. According to Vikhlinin et al. (2004), temperature profiles of relaxed clusters have a nearly universal shape beyond $\sim 15\%$ of the virial radius. This is estimated to be ~ 300 kpc for the clusters in our sample, and we choose the annuli such that the temperature in the 300 kpc annulus is well-constrained ($\sim 10\%$ statistical uncertainty). Annuli are then chosen so as to be thinner toward the cluster center where the temperature profile is steepest, and wider toward the outer regions of the cluster where the count rates are lowest. The emission-weighted mean temperature and 1σ uncertainty for each annulus are determined with XSPEC using the models *wabs* and *raymond-smith*. To calculate the spectral likelihood, the model temperature profile is integrated over the density distribution of Eq. [9] to determine the emission weighted temperature at projected radius r_i corresponding to the midpoint of annulus i. A χ^2 is determined in this way for each annulus and added to the log likelihood from the spatial fits as $\ln \mathcal{L} = -\frac{1}{2}\chi^2$.

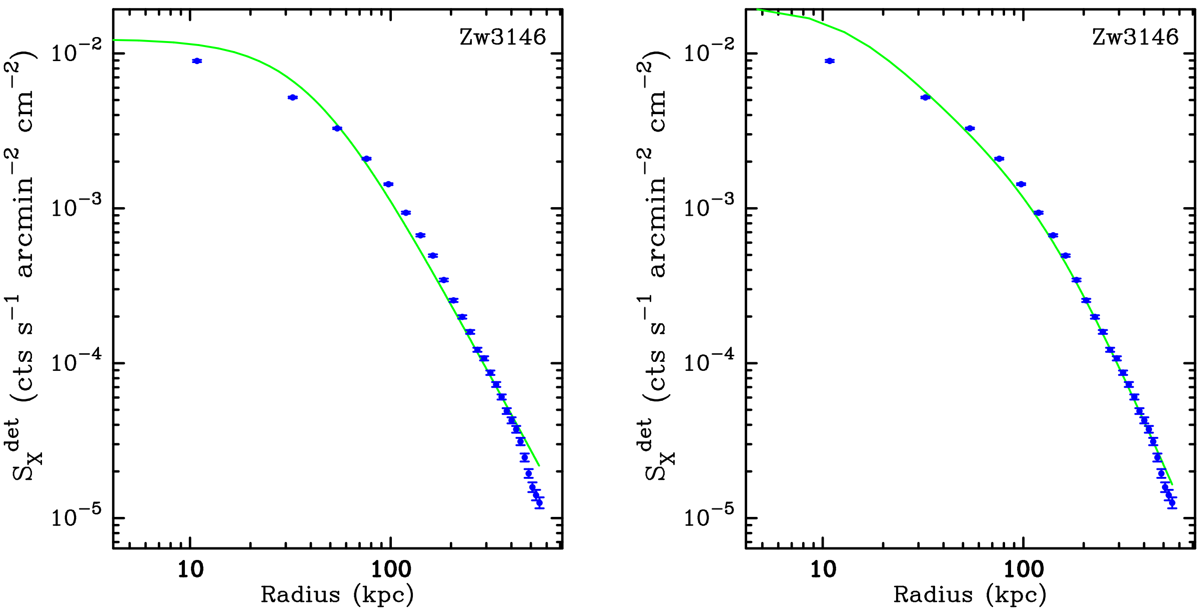

Fig. 2.— Comparison of X-ray surface brightness radial profiles for the single, isothermal β-model (left) and the non-isothermal, double β-model (right). Physical radii are again calculated for a cosmology with $\Omega_M = 0.3$, $\Omega_\Lambda = 0.7$, and $h = 0.7$. Although the single β-model provides a marginally better fit in the extreme inner regions, the double β-model provides a better fit over a larger range of radii.

4.4. Comparison of the Density Models

Having introduced three density models and described the likelihood analysis, we now fit these models to the data and compare the results. Since the non-isothermal double β-model was developed to deal with cool core clusters, we begin by comparing the results of the single and double β-models when applied to the cool core cluster Zw3146. We then show that the 100 kpc cut model gives nearly the same results as the double β-model. This model is much simpler, and it allows a more consistent treatment of the entire cluster dataset.

X-ray surface brightness profiles with best fit models from both the isothermal β-model and the non-isothermal, double β-model are shown in Figure 2. The best-fitting single β-model slightly overshoots the surface brightness in the cluster core, then trades off between over- and underestimating the surface brightness beyond the core. The best fit core radii and β values for the single and double β-models are shown in Table 3. Because the fit is driven by the high signal to noise in the sharply peaked core, Zw3146 and other cool core clusters tend to have extremely small core radii when fit by a single β-model. The small core radius leads to a small value for β as well, since the model must drop off less steeply to fit the outer, less sharply peaked regions of the cluster.

The double β-model prefers an even higher surface brightness in the extreme inner regions where the effect of cooling is strongest ($r \lesssim 20$ kpc). This is likely attributable to the fact that the double β-model also includes a spectral likelihood, and the emission-weighted temperature is strongly constrained in the core, as demonstrated by Figure 3. That the temperature profile and surface brightness are not both satisfied in this innermost region could be be due to a number of factors; for instance, simulations of cluster formation and evolution indicate that cluster dark matter profiles steepen relative to the NFW prediction in their inner regions (Gnedin et al. 2004), which if true would cause the $d\rho/dr$ term in Eq. [10] to be overestimated in our analysis. *Chandra* observations of nearby clusters also indicate that HSE is not necessarily a good assumption in the inner 100 kpc (Markevitch et al. 2003b). Dealing with this issue carefully is beyond the scope of this work, however, so we conclude only that the double β-model provides a good fit to the data between ~ 20 kpc out to ~ 600 kpc, where the background begins to dominate the cluster signal.

Table 4 compares results of derived cluster properties under these models; all results are reported at 600 kpc, the limit of the X-ray data. The over- and underestimates of the surface brightness appear to roughly cancel in the case of the single β-model, and the gas masses for the single and double β-models (measured at 600 kpc) are consistent. However, the total masses are not consistent due to their linear dependence on β at large radii (cf. Eq. [15]); in this case, the small β value in the single β-model biases the total mass low. The $\sim 15\%$ difference in β between the two models for Zw3146 is actually rather modest; other cool core clusters in our sample have differences as large as $\sim 30\%$. The total mass also depends linearly on temperature. Since the best fit isothermal temperature is emission-weighted, it is dominated by the bright, cool inner core region in the single β-model case. Figure 3 shows that the best fitting isothermal temperature of 6.62 ± 0.12 keV is appropriate only for the inner regions of Zw3146, which do not contribute as much to the mass as the outer regions with their greater volume.

In summary, the single isothermal β-model is driven by the properties of the bright inner region, but in cool core clusters these properties are not indicative of the overall cluster behavior and the results are therefore biased. The double β model gives a better overall fit to the surface brightness data, and the temperature profile of Figure 3 is also well fit. However, not all of the cool core clusters in our sample have data of sufficient quality that we can extract such detailed temperature profiles. Furthermore, many non-cool core clusters have significant substructure in their cores (e.g., Markevitch et al. 2003b) which cannot be described by either of the models considered above.

We therefore fit the 100 kpc-cut model to the data, with results shown in Figure 4. The outer regions of the cluster are well fit by this model. As Table 3 indicates, the values of

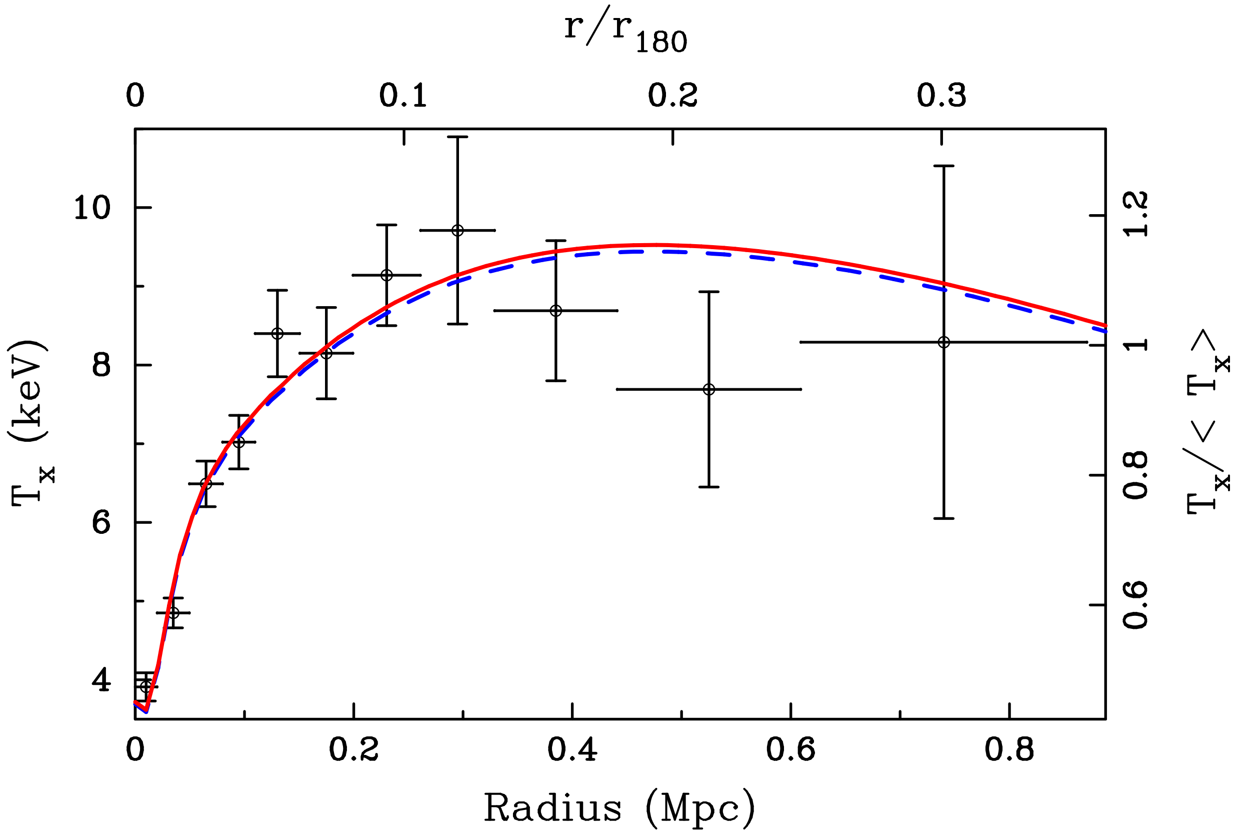

Fig. 3.— The spectral temperature profile extracted from the Zw3146 *Chandra* data along with the best fitting X-ray (solid red) and SZE (dashed blue) models from the non-isothermal, double β-model. The bars along the x-direction represent the bins within which T_x is calculated, and are not statistical error bars.

Table 3. Fit Parameters for Three Cluster Models

Model	θ_c ($''$)	β	T_x (keV)
single β	$9.0^{+0.1}_{-0.1}$	$0.567^{+0.002}_{-0.002}$	$6.62^{+0.12}_{-0.12}$
double β	$4.3^{+0.1}_{-0.1}$,$25.1^{+0.5\text{a}}_{-0.7}$	$0.667^{+0.005}_{-0.007}$	$\cdots$
single β, $r \geq 100$ kpc	$30.4^{+0.9}_{-0.9}$	$0.736^{+0.009}_{-0.009}$	$8.28^{+0.30}_{-0.29}$

[a]Values correspond to inner and outer θ_c, resp.

Table 4. Derived Properties for Three Cluster Models

Model	$M_{\rm gas}^{\rm x\text{-}ray}$ (10^{13}M$_\odot$)	$M_{\rm total}$ (10^{14}M$_\odot$)	$f_{\rm gas}^{\rm x\text{-}ray}$
single β	$5.37^{+0.07}_{-0.07}$	$2.66^{+0.08}_{-0.08}$	$0.202^{+0.004}_{-0.003}$
double β	$5.50^{+0.08}_{-0.09}$	$4.00^{+0.15}_{-0.17}$	$0.121^{+0.003}_{-0.003}$
single β, $r \geq 100$ kpc	$5.26^{+0.12}_{-0.12}$	$4.23^{+0.25}_{-0.24}$	$0.124^{+0.005}_{-0.004}$

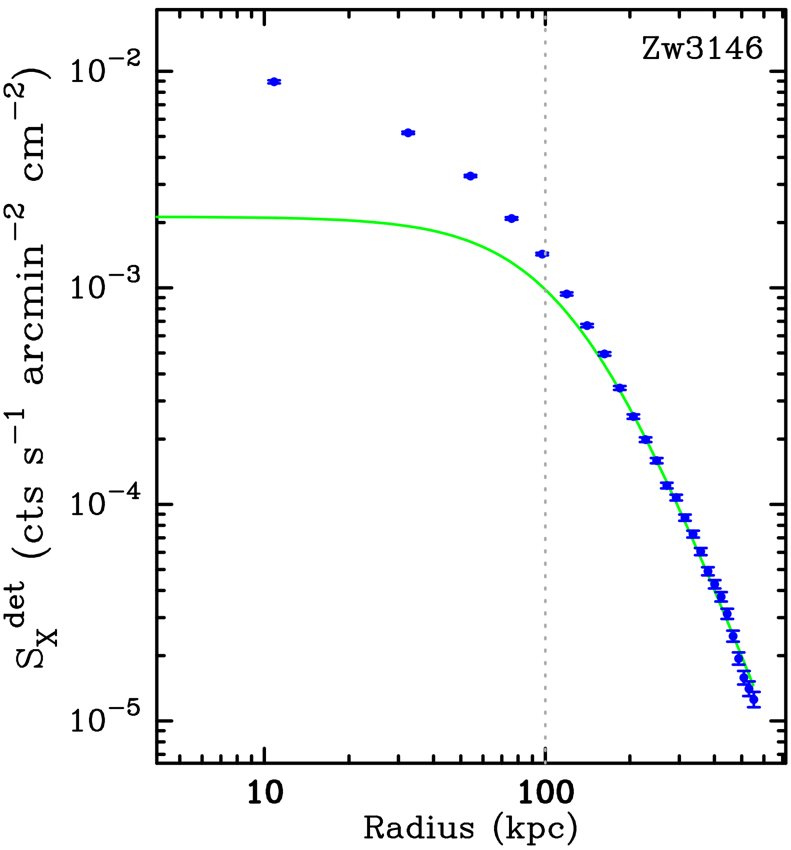

Fig. 4.— The radial profile is calculated using a single β-model, but excluding the inner 100 kpc from the fit as denoted by the dotted vertical line. (This radius is calculated for Ω_M= 0.3, Ω_Λ= 0.7, and h = 0.7). The quality of the fit outside the core is comparable to that of the double β-model.

θ_c and β are larger when the central 100 kpc are excluded and the mean emission-weighted temperature, as compared with Figure 3, is a better representation of the temperature of the cluster regions used in the fit. Table 4 shows that the gas mass is comparable to that of the other two models; this indicates that excluding the small core region from the fit and extrapolating into the cluster center has little effect on the derived masses since the volume of the extrapolated region is so small. The total cluster mass and gas mass fraction are consistent with the results of the double β-model. This model can be applied to all clusters in the sample, allowing a consistent analysis of the entire data set.

We now test the 100 kpc-cut model on clusters with different morphologies, applying it to the SZE data as well. In the rest of this work, cluster properties are calculated at r_{2500}, the radius at which the mean enclosed cluster density is equal to $2500\rho_{\rm crit}$. The *Chandra* data usually extend to at least r_{2000} before the cluster signal becomes dominated by background noise, and since r_{2500} typically subtends between $50''$ and $200''$ for clusters in our sample, the interferometric data still have good sensitivity on this scale. Since this radius is well matched to the observations, cluster properties do not have to be extrapolated to radii beyond the limits of the data. Reporting results at this radius also facilitates comparison with other recent cluster studies such as those of Allen et al. (2004) and the simulations of Kravtsov et al. (2005).

Surface brightness profiles for Zw3146 and two additional clusters are shown in Figure 5, and best-fitting models both with and without the central 100 kpc cut out are overlaid. For simplicity, we will now refer to these models as the 100 kpc-cut model and "full-fit" model. The double β-model is not treated here since the additional objects are not cool core clusters. Of the additional clusters, A611 appears very regular in X-ray and SZE (cf. Figure 1), although it does not have a bright, sharply peaked surface brightness profile. The cluster A665, by contrast, does not appear at all relaxed in Figure 1. Its peak X-ray emission is far offset from the center of the large-scale flux distribution, and its surface brightness profile has a sharp ridge around 100 kpc.

The 100 kpc-cut case clearly provides a better fit to the outer regions of both Zw3146 and A665, where most of the cluster mass is contained. The fit to the outer regions does not appear any different between the two cases for A611. Best fit β-model parameters and spectroscopic temperatures for these clusters are shown in Table 5; the SZE results reflect the case where θ_c and β are linked to the X-ray dataset, as described in §4.3. The X-ray results for Zw3146 are discussed above, and we find that the central SZE decrement also increases in the full-fit case, even though the SZE dataset is unchanged as described in §4.1. This is presumably a response to the smaller X-ray driven θ_c and β; the overall normalization of the fit must increase in order to still fit the SZE data at large radii. By contrast, the

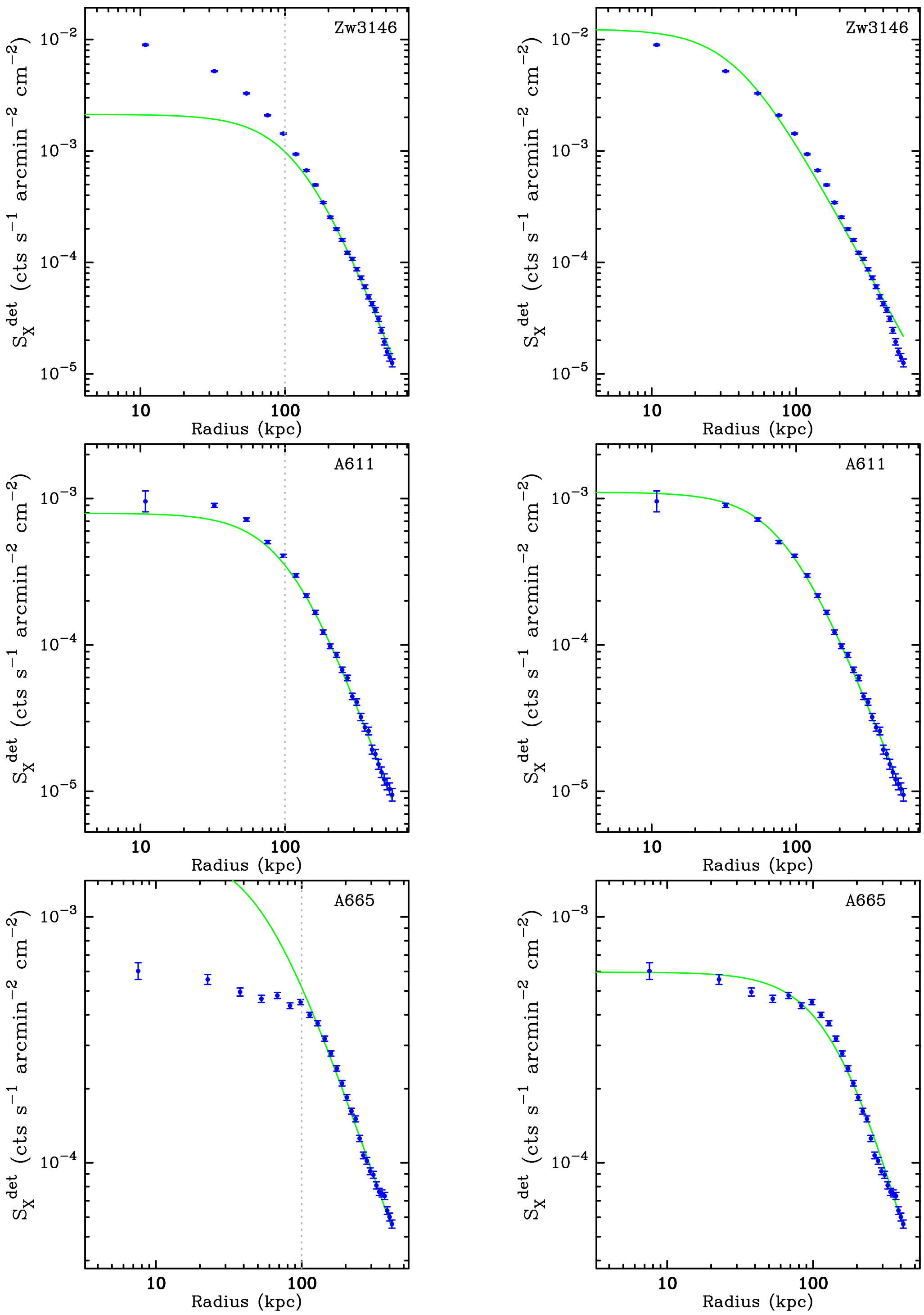

Fig. 5.— Surface brightness profiles are shown for clusters Zw3146, A611, and A665 with (left) and without (right) the inner 100 kpc of the X-ray data cut out. The position of the 100 kpc cut is marked by the vertical dotted line in left-hand panels. The 100 kpc-cut fits do a better job of fitting the outer cluster regions for a range of cluster morphologies.

X-ray and SZE results for A611 change very little whether the central 100 kpc are included or removed, and the spectroscopic temperature does not change at all. The A665 results represent an opposite extreme; the data prefer a much lower central X-ray surface brightness for the full-fit case. The trends in the fit parameters are therefore opposite those in the Zw3146 case, with S_{x0} and ΔT_0 decreasing while θ_c and β increase to compensate. The change in spectroscopic temperature is small, as with A611.

Derived cluster properties are shown in Table 6, where the first line for each cluster shows results for the 100 kpc-cut model evaluated at r_{2500}. The second line shows results of the full-fit model, although cluster properties are again determined at the 100 kpc-cut r_{2500} for consistency with the line above. In the third line the derived cluster properties are calculated at the full-fit value of r_{2500}. We focus on the first two lines for now, returning to the third line at the end of the discussion.

The X-ray determined $M_{\rm gas}$ should be a robustly measured quantity. Since the surface brightness profile essentially goes as n_e^2 and any small-scale substructure visible in the X-ray images is removed prior to fitting, the model should closely trace the true gas density distribution. For A611, the best-fit surface brightness profile is nearly unchanged between the two models outside of 100 kpc, so no observable change in the X-ray gas mass is seen. For Zw3146 and A665, the best-fit surface brightness profiles differ considerably between the 100 kpc-cut and full-fit models beyond 100 kpc. However, these differences cancel out on large scales and the recovered gas masses are statistically indistinguishable between the two models. The A665 results, as with Zw3146, demonstrate that extrapolating the surface brightness profile into the cluster center has little effect on the derived masses measured at r_{2500}. In general, the X-ray determined $M_{\rm gas}$ appears very stable to changes in the model so long as it is measured on scales sufficiently large relative to the core. The SZE gas mass is more sensitive to changes in the model, largely because the SZE determined central density goes as T_x^{-1} as opposed to the much weaker $T_x^{-1/4}$ in the X-ray case. Still, changes in the SZE gas masses are not severe even in the extreme cases of Zw3146 and A665, particularly given the measurement uncertainties.

The total mass is determined indirectly from the data using the HSE assumption and depends linearly on β and T_x. Since r_{2500} is typically much larger than the core radius, $M_{\rm total}$ has a negligible r_c dependence in our analysis (cf. Eq. [15]). In the case of Zw3146, the smaller T_e and β in the full-fit model decrease $M_{\rm total}$ by nearly 40% relative to the 100 kpc-cut model. The effects are less noticeable in the other two clusters; neither β nor T_x change substantially for A611, and the increase in β for the A665 full-fit model is partly offset by the decrease in T_x. Still, we find that $M_{\rm total}$ can be strongly biased by small scale behavior even when measured on large scales. This is especially disturbing in light of the fact that, as mentioned previously, recent *Chandra* observations by M. Markevitch and collaborators suggest that HSE is generally not satisfied within the central 100 kpc of clusters, both relaxed and unrelaxed. Allowing a region not in HSE to drive fits that assume HSE will likely bias the mass results. Furthermore, r_{2500} is determined from total mass measurements so this bias extends to any cluster properties calculated at that radius. This is seen in the third line of Table 6 for each cluster. In the case of Zw3146, the smaller total mass means that a mean density of $2500\rho_{\rm crit}$ is reached at a smaller radius; the resulting r_{2500} is 20% smaller than its 100 kpc-cut value, and this is reflected in the X-ray and SZE gas masses. Although this effect is weak for A611 and A665, it is capable of having a substantial effect on other cool core clusters and can be avoided by using the 100 kpc-cut model.

Statistical comparison of the full-fit model and the 100 kpc-cut model is complicated by the fact that the fit statistic used for the X-ray data (Eq. [19] times a factor of -2) does not provide a direct test of the goodness of fit. An estimate of goodness of fit is instead determined we use Monte-Carlo simulations and follow the method of Winkler et al. (1995). We first construct the best-fit model and compare it with the data to determine the fit statistic. We then randomly add Poisson noise to the best-fit model, creating 10^4 different realizations, and calculate the fit statistic for each of these realizations by comparing them with the original best-fit model. The fraction of simulations that give a lower fit statistic than that of the best-fit model compared to the data is called the "goodness" (e.g., Jonker et al. 2005), with values near 0.5 indicating that the best-fit model is a good description of the data and values near zero or one indicating a poor description.

Direct comparison of results from the two models is further complicated by the fact that the full-fit results are heavily weighted toward the central pixels which contain most of the photon counts. Therefore a cool core cluster may have a reasonable goodness as long as the central regions are well fit, while the outer regions, which contain most of the mass, could be poorly fit. In the case of Zw3146, the goodness for the full-fit model is 0.431 compared with a goodness of 0.475 for the 100 kpc-cut model. These are both acceptable descriptions of the data, despite the fact that the outer regions of the cluster are poorly described by the full-fit model (cf. Figure 2). Having established that most of the cluster mass measured at r_{2500} lies outside of the central 100 kpc, it is interesting to compare the goodness for the 100 kpc-cut X-ray model with that of a fit that still excludes the central 100 kpc, but uses the best-fit parameters from the full-fit model. In the case of Zw3146, such a model returns a goodness of zero, indicating that the parameters from the full-fit model are a poor description of the outer cluster regions as expected. The same is true for A665; the best-fit parameters obtained from the full-fit model give a goodness of zero when the central 100 kpc are excluded, compared with a goodness of 0.343 from the standard 100 kpc-cut model. The difference is much smaller for A611; the 100 kpc-cut model has a goodness of 0.462, compared with a goodness of 0.398 when the central 100 kpc are excluded but model parameters from the full-fit model are used.

Model comparison is easier with the SZE data, for which the fit statistic of Eq. [20] is just $-\frac{1}{2}\chi^2$. Furthermore, the central 100 kpc are not excised from the SZE datasets, so the models can be compared directly. Converting the best-fit maximum likelihoods for the SZE data to a simple χ^2, we find that the 100 kpc-cut model parameters generally provide a better fit to the SZE data than parameters from the full-fit model. This suggests that the SZE data are not strongly sensitive to the behavior of the cluster core, since the core is not excluded in the fits. For instance, in the case of the cool core cluster Zw3146 we find $\chi^2_{\rm ff} - \chi^2_{\rm 100c} = 4.2$, where $\chi^2_{\rm ff}$ is the least χ^2 for the full-fit model and $\chi^2_{\rm 100c}$ is that for the 100 kpc-cut model. For the case of A665, the difference is $\chi^2_{\rm ff} - \chi^2_{\rm 100c} = 1.6$ and for A611 the difference is 1.3. The 100 kpc-cut model is a better fit to the SZE data for eight of the ten cool core clusters, and provides a better fit to other clusters that, like A665, show evidence of significant core structure, such as A1914.

We conclude that in clusters with very regular morphologies, such as A611, the 100 kpc-cut and full-fit models return nearly identical results. However, in clusters with more complex morphologies, such as Zw3146 and A665, the 100 kpc-cut fit is a better fit to the outer regions of the cluster, where most of the mass lies. This holds for both X-ray and SZE datasets, suggesting that the SZE data are not very sensitive to core behavior. Based on the results of this section, we adopt the single isothermal β-model with inner 100 kpc excluded for all subsequent data analysis.

4.5. Fitting the 100 kpc-cut Model to SZE Data

In the previous section, the SZE θ_c and β were linked to the X-ray values, while ΔT_0 adjusted to its best fit value. To fully exploit the differing density dependences of the X-ray and SZE data, however, we need a method for fitting the SZE data independent of the X-ray images. The parameters θ_c and β are not well constrained individually by the SZE data due to the limited spatial sampling of the interferometer, and the corresponding mass probability distributions are non-Gaussian and difficult to interpret. Some prior on θ_c or β must therefore be used to obtain meaningful results from SZE data alone. While typical core radii can span a range greater than an order of magnitude depending on the dynamical state of a cluster (e.g., White et al. 1997; Ota & Mitsuda 2002; Reese et al. 2002; Ettori et al. 2004), the values of β are consistently in a range between 0.5 and 1.0 (e.g., Jones & Forman 1999; Mohr et al. 1999; Ettori et al. 2004). In addition, the SZE determined β may be biased at large radii under the isothermal assumption, since Compton-y goes linearly with T_e and negative temperature gradients are expected in the outer regions of clusters (Vikhlinin 2005). We therefore choose to put a prior on β. To determine an appropriate prior, we construct a histogram of best-fit, 100 kpc-cut β values from our own *Chandra* analysis; the 100 kpc-cut values are chosen because the SZE data should be more sensitive to the outer regions of the cluster. The 100 kpc-cut β values are almost entirely in the 0.5—1.0 range, with most clustered between 0.6 and 0.8. The median value of the distribution is $\beta = 0.7$, and we fix β at this value in the SZE-only fitting.

With β fixed, the long, diffuse tails of the distributions vanish; the results are nearly Gaussian and are treated as such. To test the effect of changing β, we rerun the analysis with β fixed at 0.6 and 0.8, a range encompassing most of our clusters. The results for all three values of β used are shown in Table 7. All changes in the parameters are small relative to the 68% statistical uncertainties. Marginalizing over β by allowing it to vary between 0.6 and 0.8 in the MCMC fits does lead to larger uncertainties in $M_{\rm total}$, although $M_{\rm gas}$ is not strongly affected. However, the uncertainties in this treatment become increasingly asymmetrical as the range in β is increased, and based on the results of Table 7 we choose to fix β at 0.7 in all SZE only fitting for the rest of this work.

Finally, we note that even with β fixed at 0.7, some clusters in the sample still have long tails in their parameter distributions and are not well fit to the SZE data only. The best results are for clusters with both BIMA and OVRO observations (cf. Table 2), as these have the most complete sampling in the u-v plane. Only clusters with well-behaved probability distributions are included in the SZE-only sample, and their properties are described in §5.

4.6. Effects of Asphericity

All cluster analysis to this point has assumed a spherical model. In practice, however, clusters are not perfect spheres and can demonstrate biaxial or triaxial geometries. We now seek to quantify the level of uncertainty introduced by asphericity so it can be accounted for when final results are presented in §5.

The X-ray data for all 36 clusters are refit with a 100 kpc-cut isothermal β-model that accounts for projected ellipticity η and position angle of the clusters on the sky. We find a mean projected ellipticity $\langle\eta\rangle = 0.79$ with rms scatter 0.09, where η is the ratio of a cluster's minor axis to major axis. This is similar to the results of Mohr et al. (1995), who find $\langle\eta\rangle = 0.80$ with rms scatter 0.12 for a sample of 65 clusters studied by *Einstein*. Piffaretti et al. (2003) study a sample of 10 clusters with a distribution of η values consistent with ours; applying several different triaxial geometries, they find that cluster asphericity causes on average a $\sim 10\%$ offset in the derived total mass evaluated at the core radius (~ 100 kpc). However, Piffaretti et al. do not consider the case in which the principal axes of the triaxial distribution are inclined at some angle to the line of sight. Inclination angle is treated by, e.g., Cooray (1998), who extends the asphericity analysis of Fabricant et al. (1984) to X-ray derived gas mass and total mass.

Using relations found in those papers, we find that an ellipsoidal cluster with $\eta = 0.8$ and axis of symmetry inclined at 45° to the line of sight can have a derived total mass in error by 12% and derived gas mass in error by 6% if modeled as a sphere. Extending this to the more complex triaxial distributions, we conservatively estimate an additional statistical uncertainty of 10% in the X-ray derived $M_{\rm gas}$ and 15% in $M_{\rm total}$. This translates to a $\sim 20\%$ uncertainty in the X-ray derived gas mass fractions, given that the changes in gas mass and total mass may add but may also partially cancel depending on inclination angle and geometry (Piffaretti et al. 2003). As for SZE observations, Grego et al. (2000) calculate the gas mass fraction of A370 assuming both prolate and oblate geometries and find a resulting uncertainty of 20%. This cluster has $\eta = 0.64$, however, so we assume a milder 10% uncertainty for the SZE gas mass fractions in our sample. The SZE analysis is less sensitive to asphericity than the X-ray results because its density dependence is linear rather than n_e^2.

5. Results

The results of 100 kpc-cut fits to the ICM gas distribution for all clusters in our sample are shown in Table 8. Uncertainties are statistical only; systematic uncertainties are non-negligible, however, and are discussed in §6. X-ray surface brightness profiles along with best-fit models for all clusters are shown in Figure 6. A vertical dotted line is drawn at a radius of 100 kpc in each panel; only data to the right of this line are included in the fits. As the figure demonstrates, the isothermal β-model with inner 100 kpc excluded consistently provides an excellent fit to the outer regions of the clusters. Derived cluster properties from the jointly fit X-ray and SZE data are provided in Table 9, measured at r_{2500}; these properties are determined using the methods described in §4.2. All quantities are calculated assuming a ΛCDM cosmology with Ω_M=0.3, Ω_Λ=0.7, and $h = 0.7$. Estimated cooling times for each cluster are also shown in the table, calculated as the total available radiative energy divided by the rate at which it is emitted, or:

$$t_{\rm cool} \approx \frac{3 k_{\rm B} T_x \mu_{\rm H}}{2 \Lambda_{e{\rm H}} n_e \mu_{\rm tot}}. \tag{21}$$

Since we are estimating the central cooling time, we use the values of n_e, $\Lambda_{e\mathrm{H}}$, and T_x that include the core; this is the only entry in Table 9 calculated with the inner 100 kpc included. Cross-referencing the t_{cool} results with the panels of Figure 6, we find that clusters with $t_{\mathrm{cool}} \lesssim 0.3$ demonstrate the bright, sharply peaked cores typical of cool core clusters. We therefore designate these clusters, MC0744, Zw3146, A1413, A1689, R1347, MS1358, A1835, MC1423, A2261, and R2129, as the cool core sample throughout the remainder of this work.

Model parameters and cluster properties determined from fits to the SZE data with β fixed at 0.7 are provided in Table 10, measured at the X-ray/SZE determined r_{2500} for consistency with Table 9. Twenty-one of the 36 clusters in the sample have SZE data of sufficient quality that both θ_c and ΔT_0 can be individually constrained with reasonable, nearly Gaussian uncertainties. Although no X-ray information on the spatial structure of the gas is used in the fits, X-ray spectral data are still incorporated into the total likelihood using the method described in §4.3. However, comparison of the results in Tables 9 and 10 should still provide useful constraints on systematics associated with spatial modeling of the gas. For clarity, we hereafter denote any results derived from the SZE data with shape parameters linked to the X-ray data as SZE I results, and any results derived from fits directly to the SZE data with β fixed at 0.7 as SZE II results.

Table 5. Comparison of Fit Parameters for Different ICM Models

Cluster	Model	S_{x0}[a]	θ_c ($''$)	β	ΔT_0 (mK)	T_x (keV)
Zw3146	100 kpc-cut	$2.13^{+0.09}_{-0.08} \times 10^{-3}$	$30.4^{+0.9}_{-0.9}$	$0.736^{+0.009}_{-0.009}$	$-1.172^{+0.143}_{-0.144}$	$8.28^{+0.30}_{-0.29}$
...	All Data	$1.24^{+0.02}_{-0.02} \times 10^{-2}$	$9.0^{+0.1}_{-0.1}$	$0.567^{+0.002}_{-0.002}$	$-1.984^{+0.259}_{-0.254}$	$6.62^{+0.12}_{-0.12}$
A611	100 kpc-cut	$7.93^{+0.91}_{-0.71} \times 10^{-4}$	$25.7^{+2.1}_{-2.2}$	$0.632^{+0.017}_{-0.017}$	$-0.761^{+0.084}_{-0.082}$	$6.79^{+0.41}_{-0.38}$
...	All Data	$1.10^{+0.03}_{-0.03} \times 10^{-3}$	$19.9^{+0.7}_{-0.6}$	$0.592^{+0.008}_{-0.007}$	$-0.793^{+0.083}_{-0.085}$	$6.81^{+0.29}_{-0.30}$
A665	100 kpc-cut	$1.87^{+0.42}_{-0.32} \times 10^{-3}$	$17.7^{+2.9}_{-2.5}$	$0.454^{+0.023}_{-0.018}$	$-1.330^{+0.117}_{-0.119}$	$8.37^{+0.37}_{-0.33}$
...	All Data	$5.96^{+0.10}_{-0.10} \times 10^{-4}$	$49.4^{+1.4}_{-1.4}$	$0.536^{+0.007}_{-0.007}$	$-1.048^{+0.096}_{-0.094}$	$8.24^{+0.32}_{-0.32}$

[a]Units are counts cm^{-2} arcmin^{-2} s^{-1}.

Table 6. Comparison of Derived Properties for Different ICM Models

Cluster	Model	$M_{\rm gas}^{\rm x\text{-}ray}(R)$ (10^{13} M$_\odot$)	$M_{\rm gas}^{\rm sze}(R)$ (10^{13} M$_\odot$)	$M_{\rm total}(R)$ (10^{14} M$_\odot$)	R (kpc)
Zw3146	100 kpc-cut	$4.42^{+0.11}_{-0.11}$	$3.80^{+0.47}_{-0.47}$	$3.62^{+0.22}_{-0.20}$	570[a]
⋯	All Data	$4.49^{+0.06}_{-0.06}$	$4.64^{+0.60}_{-0.60}$	$2.33^{+0.07}_{-0.07}$	570[a]
⋯	All Data	$3.33^{+0.04}_{-0.04}$	$3.44^{+0.44}_{-0.45}$	$1.87^{+0.05}_{-0.05}$	460[b]
A611	100 kpc-cut	$2.36^{+0.11}_{-0.11}$	$2.33^{+0.26}_{-0.26}$	$2.14^{+0.22}_{-0.20}$	480[a]
⋯	All Data	$2.36^{+0.08}_{-0.08}$	$2.17^{+0.23}_{-0.23}$	$2.04^{+0.14}_{-0.14}$	480[a]
⋯	All Data	$2.29^{+0.07}_{-0.08}$	$2.11^{+0.22}_{-0.22}$	$2.00^{+0.14}_{-0.14}$	470[b]
A665	100 kpc-cut	$2.62^{+0.10}_{-0.09}$	$2.53^{+0.22}_{-0.23}$	$2.00^{+0.14}_{-0.12}$	500[a]
⋯	All Data	$2.66^{+0.10}_{-0.10}$	$3.04^{+0.27}_{-0.28}$	$2.17^{+0.14}_{-0.14}$	500[a]
⋯	All Data	$2.84^{+0.11}_{-0.11}$	$3.24^{+0.29}_{-0.30}$	$2.26^{+0.15}_{-0.15}$	510[b]

[a]Radius r_{2500} from the 100 kpc-cut model.

[b]Radius r_{2500} from model including the central 100 kpc.

Table 7. SZE Fitting Results for Different Values of β

β	θ_c ($''$)	ΔT_0 (mK)	$M_{\rm gas}^{\rm sze}$ (10^{13} M$_\odot$)	$M_{\rm total}$ (10^{14} M$_\odot$)	$f_{\rm gas}^{\rm sze}$
0.6	$23.2^{+11.3}_{-\ 8.9}$	$-1.39^{+0.20}_{-0.29}$	$5.03^{+1.03}_{-0.86}$	$3.39^{+0.14}_{-0.15}$	$0.148^{+0.036}_{-0.028}$
0.7	$29.4^{+11.9}_{-\ 9.7}$	$-1.22^{+0.18}_{-0.24}$	$4.58^{+1.02}_{-0.88}$	$3.89^{+0.18}_{-0.19}$	$0.117^{+0.032}_{-0.025}$
0.8	$35.5^{+12.0}_{-\ 9.4}$	$-1.12^{+0.16}_{-0.19}$	$4.27^{+0.97}_{-0.83}$	$4.38^{+0.21}_{-0.23}$	$0.097^{+0.027}_{-0.021}$

Table 8. Jointfit ICM Parameters

Cluster	S_{x0}[a]	S_{x0}[b]	θ_c ($''$)	β	ΔT_0 (mK)	T_x (keV)	Z (% solar)
CL0016	$3.56^{+0.12}_{-0.11} \times 10^{-4}$	$1.27^{+0.04}_{-0.04} \times 10^{-12}$	$42.8^{+2.1}_{-2.0}$	$0.742^{+0.025}_{-0.022}$	$-1.361^{+0.083}_{-0.083}$	$10.46^{+0.61}_{-0.60}$	$0.303^{+0.085}_{-0.083}$
A68	$4.62^{+0.38}_{-0.31} \times 10^{-4}$	$1.60^{+0.13}_{-0.11} \times 10^{-12}$	$55.1^{+5.3}_{-5.0}$	$0.764^{+0.046}_{-0.042}$	$-0.712^{+0.099}_{-0.103}$	$9.55^{+1.09}_{-0.96}$	$0.507^{+0.207}_{-0.204}$
A267	$5.85^{+0.81}_{-0.66} \times 10^{-4}$	$2.04^{+0.28}_{-0.23} \times 10^{-12}$	$43.1^{+5.8}_{-5.1}$	$0.720^{+0.049}_{-0.040}$	$-0.692^{+0.077}_{-0.080}$	$5.89^{+0.66}_{-0.54}$	$0.224^{+0.187}_{-0.130}$
A370	$1.70^{+0.05}_{-0.05} \times 10^{-4}$	$7.34^{+0.22}_{-0.22} \times 10^{-13}$	$61.8^{+3.6}_{-3.5}$	$0.811^{+0.039}_{-0.037}$	$-0.866^{+0.090}_{-0.088}$	$8.67^{+0.51}_{-0.49}$	$0.458^{+0.098}_{-0.095}$
MS0451	$5.42^{+0.25}_{-0.24} \times 10^{-4}$	$2.35^{+0.11}_{-0.10} \times 10^{-12}$	$40.0^{+1.9}_{-1.7}$	$0.773^{+0.026}_{-0.023}$	$-1.476^{+0.086}_{-0.086}$	$9.95^{+0.76}_{-0.69}$	$0.370^{+0.109}_{-0.108}$
MC0647	$6.19^{+0.56}_{-0.51} \times 10^{-4}$	$2.19^{+0.20}_{-0.18} \times 10^{-12}$	$24.1^{+2.0}_{-1.8}$	$0.687^{+0.023}_{-0.020}$	$-1.312^{+0.116}_{-0.123}$	$14.06^{+1.78}_{-1.59}$	$0.206^{+0.161}_{-0.109}$
A586	$9.46^{+1.22}_{-1.01} \times 10^{-4}$	$3.36^{+0.43}_{-0.36} \times 10^{-12}$	$45.3^{+5.1}_{-4.6}$	$0.723^{+0.039}_{-0.033}$	$-0.651^{+0.081}_{-0.084}$	$6.35^{+0.46}_{-0.39}$	$0.678^{+0.170}_{-0.165}$
MC0744	$4.32^{+0.36}_{-0.31} \times 10^{-4}$	$1.40^{+0.12}_{-0.10} \times 10^{-12}$	$25.8^{+2.0}_{-2.0}$	$0.723^{+0.028}_{-0.027}$	$-1.299^{+0.134}_{-0.138}$	$8.14^{+0.80}_{-0.72}$	$0.201^{+0.119}_{-0.102}$
A611	$7.95^{+0.91}_{-0.71} \times 10^{-4}$	$3.21^{+0.37}_{-0.29} \times 10^{-12}$	$25.7^{+2.1}_{-2.2}$	$0.632^{+0.017}_{-0.017}$	$-0.761^{+0.084}_{-0.082}$	$6.79^{+0.41}_{-0.38}$	$0.387^{+0.105}_{-0.104}$
A665	$1.87^{+0.42}_{-0.32} \times 10^{-3}$	$6.51^{+1.46}_{-1.11} \times 10^{-12}$	$17.7^{+2.9}_{-2.5}$	$0.454^{+0.006}_{-0.005}$	$-1.330^{+0.117}_{-0.119}$	$8.37^{+0.37}_{-0.33}$	$0.403^{+0.083}_{-0.079}$
A697	$7.28^{+0.18}_{-0.18} \times 10^{-4}$	$2.46^{+0.06}_{-0.06} \times 10^{-12}$	$42.7^{+1.6}_{-1.5}$	$0.605^{+0.011}_{-0.011}$	$-1.223^{+0.125}_{-0.121}$	$10.21^{+0.70}_{-0.65}$	$0.403^{+0.104}_{-0.104}$
A773	$6.82^{+0.50}_{-0.44} \times 10^{-4}$	$2.31^{+0.17}_{-0.15} \times 10^{-12}$	$38.7^{+2.5}_{-2.5}$	$0.594^{+0.013}_{-0.012}$	$-1.101^{+0.118}_{-0.116}$	$8.16^{+0.56}_{-0.52}$	$0.631^{+0.126}_{-0.122}$
Zw3146	$2.13^{+0.09}_{-0.08} \times 10^{-3}$	$7.56^{+0.32}_{-0.28} \times 10^{-12}$	$30.4^{+0.9}_{-0.9}$	$0.736^{+0.009}_{-0.009}$	$-1.172^{+0.143}_{-0.144}$	$8.28^{+0.30}_{-0.29}$	$0.275^{+0.055}_{-0.052}$
MC1115	$3.11^{+0.46}_{-0.36} \times 10^{-4}$	$1.04^{+0.15}_{-0.12} \times 10^{-12}$	$36.6^{+6.5}_{-5.5}$	$0.664^{+0.063}_{-0.050}$	$-1.424^{+0.186}_{-0.199}$	$12.16^{+2.34}_{-2.13}$	$0.390^{+0.296}_{-0.225}$
MS1137	$2.12^{+0.41}_{-0.29} \times 10^{-4}$	$6.17^{+1.19}_{-0.84} \times 10^{-13}$	$22.3^{+3.8}_{-3.4}$	$0.877^{+0.097}_{-0.078}$	$-0.775^{+0.094}_{-0.102}$	$4.47^{+0.53}_{-0.44}$	$0.686^{+0.275}_{-0.306}$
MC1149	$2.51^{+0.11}_{-0.11} \times 10^{-4}$	$8.13^{+0.36}_{-0.36} \times 10^{-13}$	$44.7^{+2.6}_{-2.3}$	$0.666^{+0.020}_{-0.018}$	$-1.166^{+0.112}_{-0.114}$	$9.93^{+0.80}_{-0.68}$	$0.222^{+0.104}_{-0.097}$
A1413	$1.25^{+0.17}_{-0.12} \times 10^{-3}$	$4.31^{+0.59}_{-0.41} \times 10^{-12}$	$37.9^{+3.7}_{-4.3}$	$0.536^{+0.015}_{-0.015}$	$-1.037^{+0.150}_{-0.150}$	$7.51^{+0.35}_{-0.29}$	$0.518^{+0.090}_{-0.088}$
CL1226	$7.26^{+2.34}_{-1.49} \times 10^{-4}$	$2.36^{+0.76}_{-0.48} \times 10^{-12}$	$16.2^{+3.8}_{-3.3}$	$0.732^{+0.084}_{-0.060}$	$-1.715^{+0.202}_{-0.234}$	$13.47^{+2.72}_{-2.20}$	$0.285^{+0.236}_{-0.164}$
A1689	$1.70^{+0.08}_{-0.07} \times 10^{-3}$	$6.26^{+0.29}_{-0.26} \times 10^{-12}$	$48.4^{+2.1}_{-2.0}$	$0.688^{+0.013}_{-0.012}$	$-1.651^{+0.130}_{-0.137}$	$10.46^{+0.46}_{-0.47}$	$0.331^{+0.072}_{-0.077}$
R1347	$4.35^{+0.32}_{-0.25} \times 10^{-3}$	$1.56^{+0.07}_{-0.06} \times 10^{-11}$	$17.7^{+0.7}_{-0.8}$	$0.651^{+0.007}_{-0.007}$	$-2.777^{+0.294}_{-0.284}$	$16.48^{+0.99}_{-0.92}$	$0.280^{+0.083}_{-0.087}$
MS1358	$4.28^{+0.32}_{-0.26} \times 10^{-4}$	$1.79^{+0.13}_{-0.11} \times 10^{-12}$	$28.9^{+1.8}_{-1.9}$	$0.638^{+0.016}_{-0.016}$	$-0.721^{+0.096}_{-0.097}$	$8.93^{+0.88}_{-0.74}$	$0.591^{+0.174}_{-0.165}$
A1835	$2.09^{+0.08}_{-0.07} \times 10^{-3}$	$9.49^{+0.36}_{-0.32} \times 10^{-12}$	$33.6^{+1.0}_{-1.0}$	$0.690^{+0.007}_{-0.008}$	$-1.636^{+0.116}_{-0.114}$	$11.44^{+0.66}_{-0.56}$	$0.422^{+0.103}_{-0.100}$

Table 8—Continued

Cluster	S_{x0}[a]	S_{x0}[b]	θ_c ($''$)	β	ΔT_0 (mK)	T_x (keV)	Z (% solar)
MC1423	$8.83^{+1.06}_{-0.94} \times 10^{-4}$	$3.21^{+0.39}_{-0.34} \times 10^{-12}$	$14.6^{+1.2}_{-1.0}$	$0.637^{+0.012}_{-0.011}$	$-1.177^{+0.210}_{-0.200}$	$6.97^{+0.42}_{-0.40}$	$0.420^{+0.094}_{-0.091}$
A1914	$3.04^{+0.12}_{-0.11} \times 10^{-3}$	$1.03^{+0.04}_{-0.04} \times 10^{-11}$	$44.0^{+1.3}_{-1.3}$	$0.734^{+0.009}_{-0.010}$	$-1.565^{+0.125}_{-0.125}$	$9.48^{+0.35}_{-0.29}$	$0.229^{+0.056}_{-0.058}$
A1995	$3.95^{+0.13}_{-0.12} \times 10^{-4}$	$1.62^{+0.05}_{-0.05} \times 10^{-12}$	$57.5^{+2.7}_{-2.6}$	$1.013^{+0.041}_{-0.038}$	$-0.879^{+0.053}_{-0.052}$	$8.22^{+0.44}_{-0.45}$	$0.469^{+0.100}_{-0.098}$
A2111	$2.52^{+0.29}_{-0.24} \times 10^{-4}$	$8.87^{+1.02}_{-0.84} \times 10^{-13}$	$51.0^{+7.6}_{-6.6}$	$0.611^{+0.044}_{-0.036}$	$-0.596^{+0.117}_{-0.122}$	$8.15^{+0.98}_{-0.83}$	$0.219^{+0.167}_{-0.127}$
A2163	$1.04^{+0.02}_{-0.02} \times 10^{-3}$	$4.63^{+0.09}_{-0.09} \times 10^{-12}$	$57.6^{+1.3}_{-1.2}$	$0.538^{+0.005}_{-0.005}$	$-1.903^{+0.171}_{-0.177}$	$14.81^{+0.39}_{-0.38}$	$0.315^{+0.046}_{-0.046}$
A2218	$4.99^{+0.08}_{-0.07} \times 10^{-4}$	$1.69^{+0.03}_{-0.02} \times 10^{-12}$	$70.3^{+1.7}_{-1.7}$	$0.765^{+0.014}_{-0.013}$	$-0.870^{+0.079}_{-0.078}$	$7.80^{+0.41}_{-0.37}$	$0.333^{+0.081}_{-0.078}$
R1716	$1.68^{+0.66}_{-0.39} \times 10^{-4}$	$5.49^{+2.16}_{-1.27} \times 10^{-13}$	$17.6^{+5.7}_{-4.5}$	$0.665^{+0.097}_{-0.064}$	$-0.656^{+0.148}_{-0.166}$	$6.57^{+1.08}_{-0.88}$	$0.982^{+0.261}_{-0.317}$
A2259	$4.44^{+0.56}_{-0.43} \times 10^{-4}$	$1.48^{+0.19}_{-0.14} \times 10^{-12}$	$59.1^{+9.1}_{-8.4}$	$0.663^{+0.057}_{-0.048}$	$-0.397^{+0.138}_{-0.139}$	$5.81^{+0.44}_{-0.36}$	$0.486^{+0.141}_{-0.137}$
A2261	$1.61^{+0.26}_{-0.21} \times 10^{-3}$	$5.92^{+0.96}_{-0.77} \times 10^{-12}$	$28.9^{+3.5}_{-3.0}$	$0.624^{+0.023}_{-0.018}$	$-1.178^{+0.122}_{-0.121}$	$7.45^{+0.65}_{-0.55}$	$0.542^{+0.191}_{-0.189}$
MS2053	$9.60^{+1.96}_{-1.49} \times 10^{-5}$	$2.88^{+0.59}_{-0.45} \times 10^{-13}$	$27.0^{+6.2}_{-4.8}$	$0.821^{+0.122}_{-0.085}$	$-0.419^{+0.069}_{-0.078}$	$4.77^{+0.71}_{-0.58}$	$0.271^{+0.206}_{-0.161}$
MC2129	$6.12^{+0.77}_{-0.63} \times 10^{-4}$	$1.99^{+0.25}_{-0.20} \times 10^{-12}$	$24.4^{+2.9}_{-2.6}$	$0.712^{+0.040}_{-0.033}$	$-1.176^{+0.129}_{-0.133}$	$8.55^{+0.97}_{-0.80}$	$0.518^{+0.164}_{-0.161}$
R2129	$1.45^{+0.32}_{-0.24} \times 10^{-3}$	$4.99^{+1.10}_{-0.83} \times 10^{-12}$	$25.4^{+3.8}_{-3.3}$	$0.611^{+0.024}_{-0.020}$	$-0.734^{+0.113}_{-0.120}$	$6.69^{+0.49}_{-0.47}$	$0.501^{+0.147}_{-0.141}$
MC2214	$5.32^{+0.45}_{-0.41} \times 10^{-4}$	$1.76^{+0.15}_{-0.14} \times 10^{-12}$	$31.0^{+3.2}_{-2.8}$	$0.705^{+0.039}_{-0.034}$	$-1.445^{+0.123}_{-0.125}$	$10.20^{+1.02}_{-0.87}$	$0.264^{+0.137}_{-0.121}$
MC2228	$7.10^{+1.21}_{-0.89} \times 10^{-4}$	$2.36^{+0.17}_{-0.13} \times 10^{-12}$	$20.2^{+2.7}_{-2.5}$	$0.522^{+0.015}_{-0.013}$	$-1.727^{+0.166}_{-0.177}$	$8.43^{+0.78}_{-0.71}$	$0.420^{+0.132}_{-0.131}$

[a]Units are cnts cm^{-2} $arcmin^{-2}$ s^{-1}.

[b]Units are erg cm^{-2} $arcmin^{-2}$ s^{-1}.

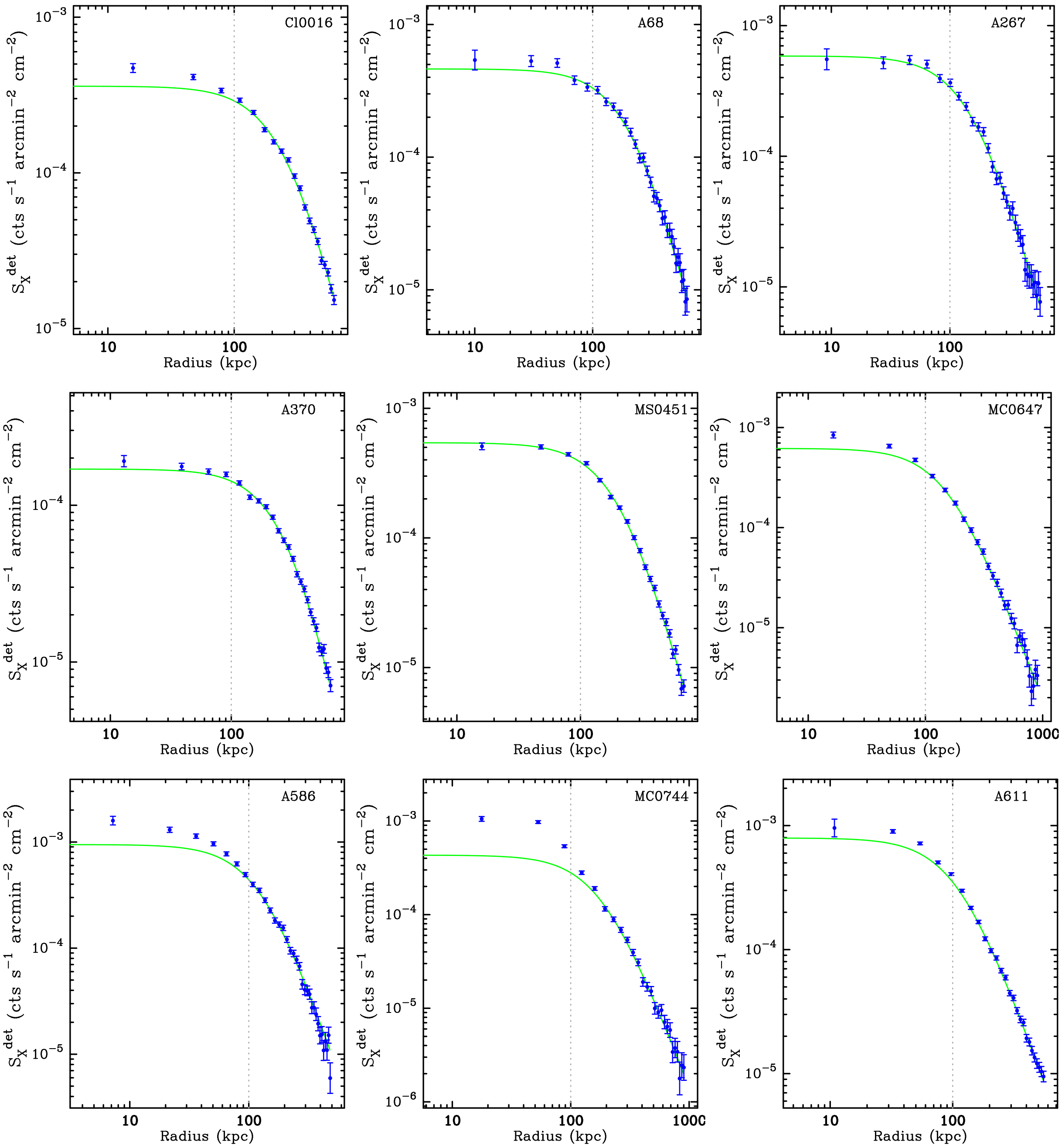

Fig. 6.— X-ray surface brightness radial profiles (blue points) with the best fit model (green lines). Radii are calculated using a reasonable input cosmology of Ω_M= 0.3, Ω_Λ= 0.7, and h = 0.7. The vertical dotted line is drawn at 100 kpc; data within this radius are not used in the fit. In general, the data are well-fit by the model outside of the core.

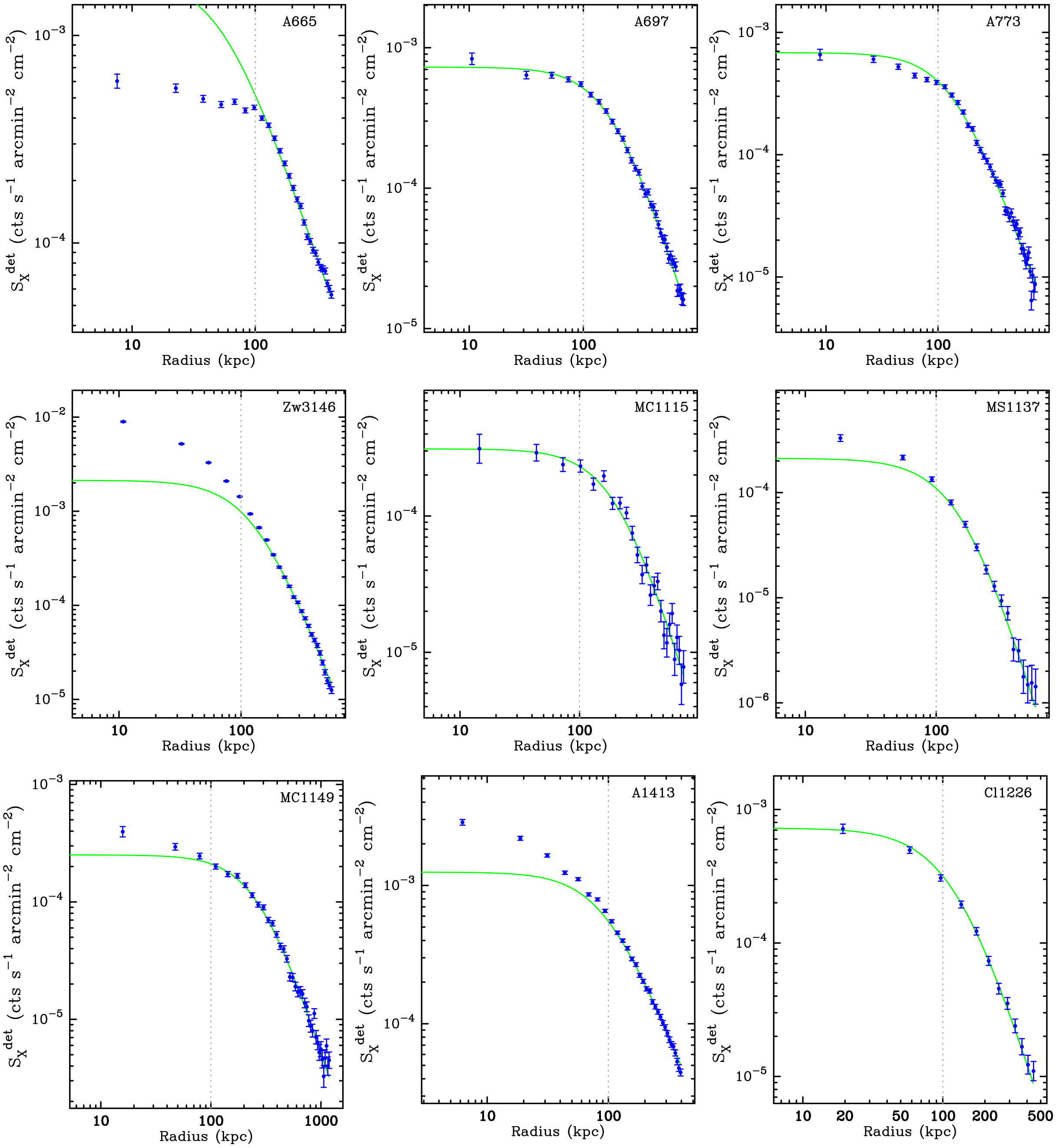
A665
A697
A773
Zw3146
MC1115
MS1137
MC1149
A1413
Cl1226
Radius (kpc)
S_X^{det} (cts s^{-1} arcmin^{-2} cm^{-2})

Fig. 6.— Cont.

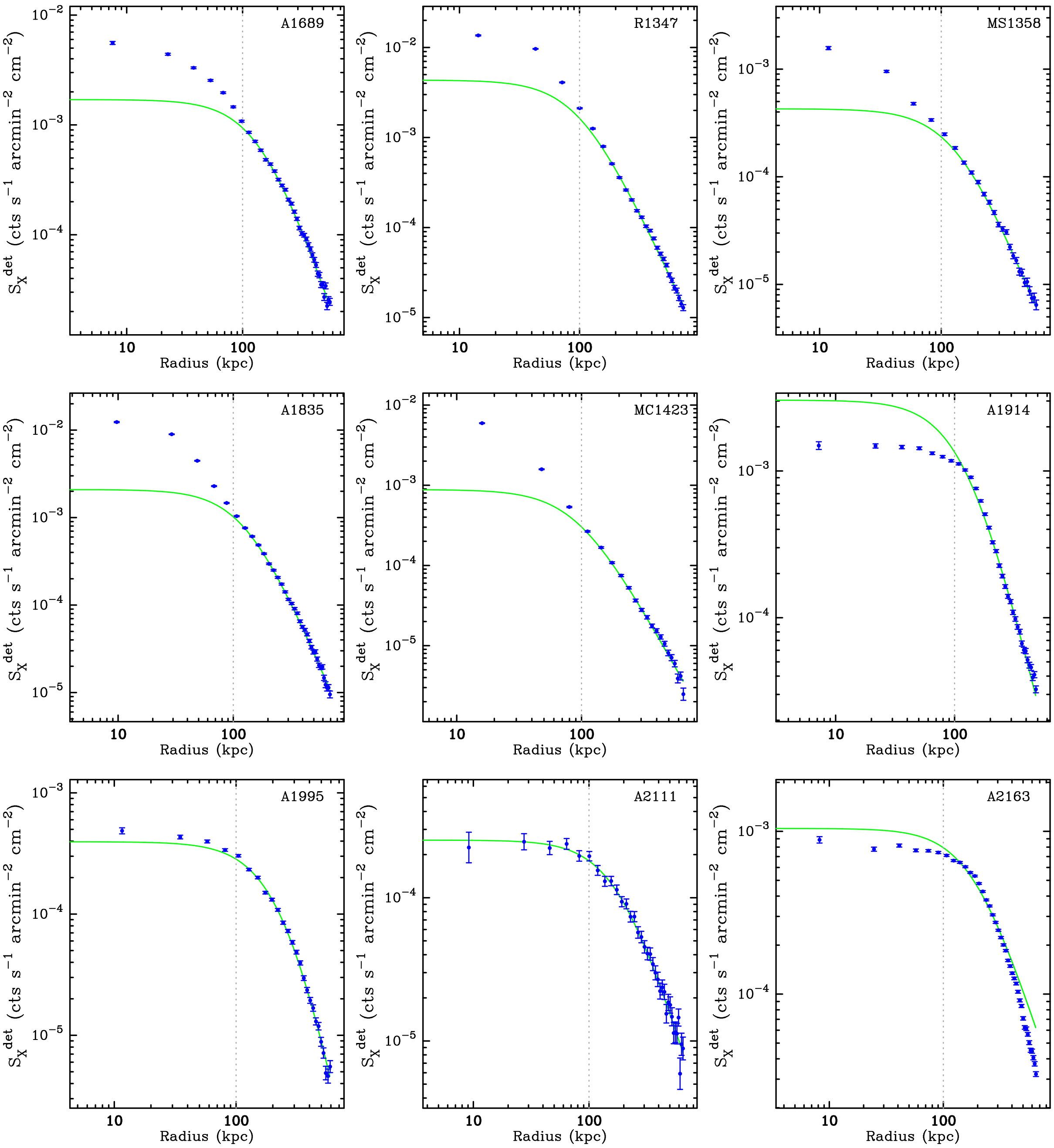
A1689
R1347
MS1358
A1835
MC1423
A1914
A1995
A2111
A2163
S_X^{det} (cts s^{-1} arcmin^{-2} cm^{-2})
Radius (kpc)

Fig. 6.— Cont.

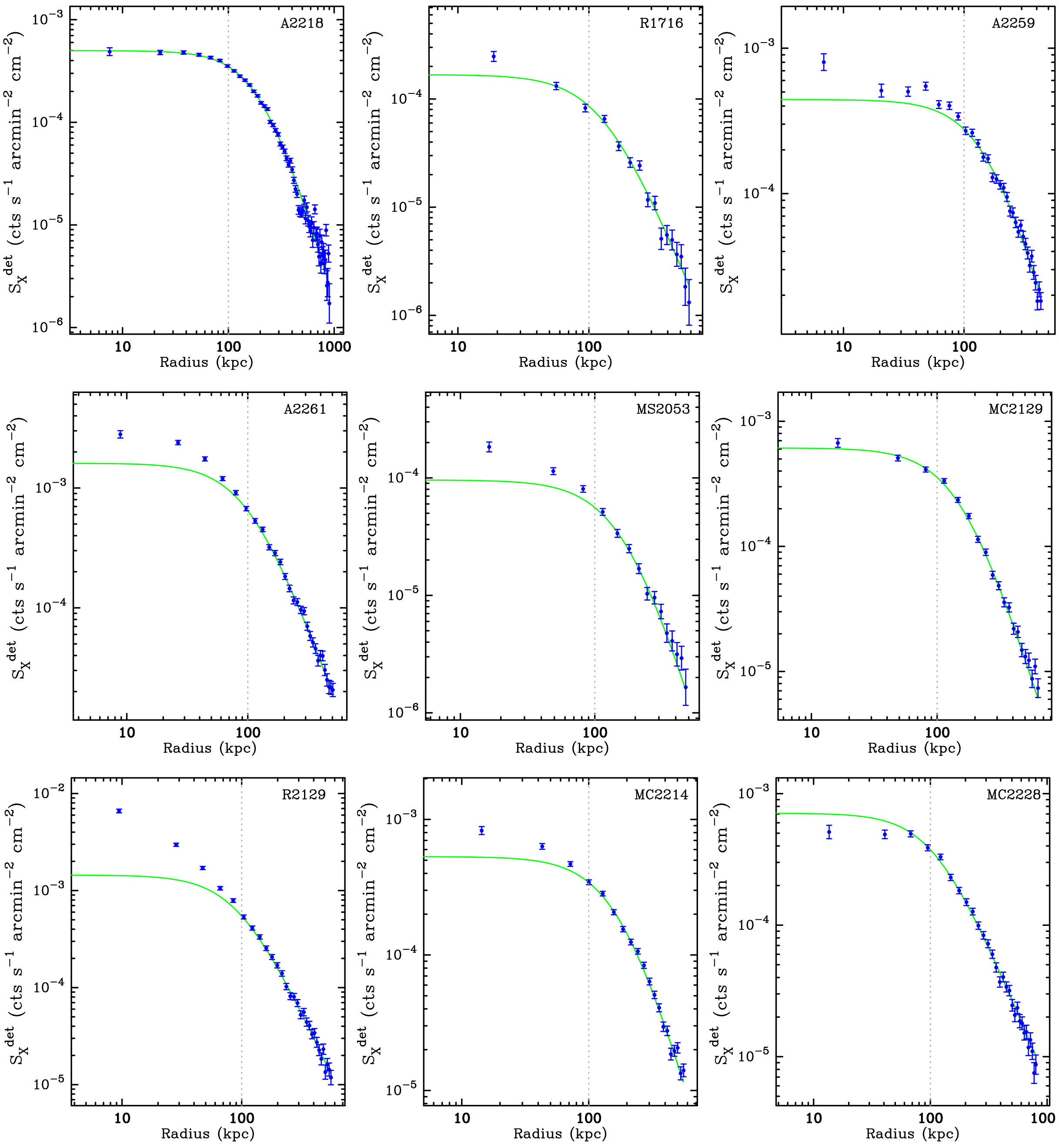
A2218
R1716
A2259
A2261
MS2053
MC2129
R2129
MC2214
MC2228
Radius (kpc)
S_X^{det} (cts s^{-1} arcmin^{-2} cm^{-2})

Fig. 6.— Cont.

Table 9. Jointfit Masses and Gas Mass Fractions

Cluster	$M_{\rm gas}^{\rm x\text{-}ray}(r_{2500})$ (10^{13} M$_\odot$)	$M_{\rm gas}^{\rm sze}(r_{2500})$ (10^{13} M$_\odot$)	$M_{\rm total}(r_{2500})$ (10^{14} M$_\odot$)	$f_{\rm gas}^{\rm x\text{-}ray}(r_{2500})$	$f_{\rm gas}^{\rm sze}(r_{2500})$	$t_{\rm cool}/t_{\rm H}$
CL0016	$4.38^{+0.29}_{-0.29}$	$4.34^{+0.26}_{-0.26}$	$3.33^{+0.39}_{-0.37}$	$0.131^{+0.007}_{-0.006}$	$0.130^{+0.016}_{-0.015}$	1.5
A68	$3.65^{+0.34}_{-0.31}$	$3.07^{+0.45}_{-0.44}$	$4.32^{+0.91}_{-0.74}$	$0.084^{+0.009}_{-0.008}$	$0.071^{+0.019}_{-0.016}$	1.4
A267	$2.24^{+0.20}_{-0.18}$	$2.83^{+0.32}_{-0.31}$	$2.03^{+0.42}_{-0.33}$	$0.110^{+0.011}_{-0.011}$	$0.140^{+0.032}_{-0.029}$	0.8
A370	$2.78^{+0.21}_{-0.20}$	$3.51^{+0.37}_{-0.36}$	$2.77^{+0.37}_{-0.33}$	$0.100^{+0.005}_{-0.005}$	$0.127^{+0.020}_{-0.018}$	2.1
MS0451	$4.76^{+0.31}_{-0.30}$	$4.79^{+0.28}_{-0.28}$	$3.76^{+0.53}_{-0.46}$	$0.127^{+0.009}_{-0.008}$	$0.127^{+0.020}_{-0.018}$	1.0
MC0647	$4.90^{+0.47}_{-0.42}$	$3.26^{+0.30}_{-0.29}$	$5.98^{+1.30}_{-1.05}$	$0.082^{+0.009}_{-0.008}$	$0.055^{+0.014}_{-0.012}$	1.0
A586	$2.26^{+0.13}_{-0.11}$	$2.49^{+0.32}_{-0.32}$	$2.48^{+0.34}_{-0.28}$	$0.091^{+0.007}_{-0.007}$	$0.100^{+0.019}_{-0.017}$	0.5
MC0744	$3.07^{+0.27}_{-0.25}$	$3.36^{+0.34}_{-0.35}$	$2.26^{+0.42}_{-0.35}$	$0.136^{+0.012}_{-0.011}$	$0.148^{+0.032}_{-0.027}$	0.3
A611	$2.36^{+0.11}_{-0.11}$	$2.33^{+0.26}_{-0.26}$	$2.14^{+0.22}_{-0.20}$	$0.110^{+0.006}_{-0.006}$	$0.109^{+0.017}_{-0.016}$	0.5
A665	$2.62^{+0.10}_{-0.09}$	$2.53^{+0.22}_{-0.23}$	$2.00^{+0.14}_{-0.12}$	$0.131^{+0.004}_{-0.004}$	$0.126^{+0.014}_{-0.013}$	1.1
A697	$4.39^{+0.28}_{-0.26}$	$4.09^{+0.41}_{-0.42}$	$3.47^{+0.40}_{-0.37}$	$0.127^{+0.007}_{-0.006}$	$0.117^{+0.019}_{-0.017}$	1.2
A773	$2.75^{+0.17}_{-0.15}$	$3.64^{+0.39}_{-0.39}$	$2.59^{+0.30}_{-0.27}$	$0.106^{+0.006}_{-0.005}$	$0.140^{+0.024}_{-0.021}$	1.0
Zw3146	$4.42^{+0.11}_{-0.11}$	$3.80^{+0.47}_{-0.47}$	$3.62^{+0.22}_{-0.20}$	$0.122^{+0.004}_{-0.004}$	$0.105^{+0.015}_{-0.014}$	0.1
MC1115	$3.84^{+0.68}_{-0.64}$	$4.42^{+0.67}_{-0.65}$	$4.45^{+1.58}_{-1.27}$	$0.086^{+0.015}_{-0.012}$	$0.099^{+0.042}_{-0.028}$	1.9
MS1137	$1.19^{+0.14}_{-0.13}$	$2.13^{+0.26}_{-0.25}$	$1.03^{+0.26}_{-0.20}$	$0.115^{+0.014}_{-0.013}$	$0.207^{+0.054}_{-0.045}$	0.7
MC1149	$3.09^{+0.34}_{-0.30}$	$3.00^{+0.30}_{-0.30}$	$2.31^{+0.40}_{-0.34}$	$0.134^{+0.008}_{-0.008}$	$0.130^{+0.022}_{-0.019}$	1.9
A1413	$2.63^{+0.11}_{-0.10}$	$2.98^{+0.43}_{-0.42}$	$2.15^{+0.17}_{-0.15}$	$0.122^{+0.004}_{-0.004}$	$0.139^{+0.022}_{-0.022}$	0.3
CL1226	$3.89^{+0.51}_{-0.46}$	$2.90^{+0.34}_{-0.30}$	$5.21^{+1.96}_{-1.39}$	$0.075^{+0.015}_{-0.014}$	$0.056^{+0.024}_{-0.018}$	0.9
A1689	$5.06^{+0.16}_{-0.17}$	$5.85^{+0.49}_{-0.47}$	$4.96^{+0.36}_{-0.36}$	$0.102^{+0.004}_{-0.004}$	$0.118^{+0.014}_{-0.013}$	0.3
R1347	$8.84^{+0.37}_{-0.35}$	$5.60^{+0.58}_{-0.60}$	$8.08^{+0.77}_{-0.69}$	$0.109^{+0.006}_{-0.005}$	$0.069^{+0.011}_{-0.010}$	0.1
MS1358	$2.53^{+0.19}_{-0.17}$	$2.23^{+0.29}_{-0.29}$	$3.13^{+0.51}_{-0.41}$	$0.081^{+0.006}_{-0.006}$	$0.071^{+0.015}_{-0.014}$	0.2
A1835	$5.78^{+0.23}_{-0.20}$	$4.98^{+0.36}_{-0.36}$	$5.56^{+0.50}_{-0.42}$	$0.104^{+0.005}_{-0.005}$	$0.089^{+0.011}_{-0.010}$	0.1

5.1. Gas Mass Fractions

Gas mass fractions, calculated as $M_{\rm gas}(r_{2500})/M_{\rm total}(r_{2500})$, are listed in Table 9 for the X-ray and SZE I samples and in Table 10 for the SZE II sample. The weighted mean values for our sample calculated with the fiducial ΛCDM cosmology and ellipticity corrections included in quadrature are 0.109 ± 0.003 for the X-ray data, 0.115 ± 0.005 for the SZE I data, and 0.116 ± 0.009 for SZE II. Gas mass fractions as a function of redshift for each of the samples are shown in Figure 7 with mean values denoted by the dashed line.

The X-ray results agree with the *Chandra* results of Allen et al. (2002) for a sample of six highly relaxed clusters; they find a mean $f_{\rm gas}$ equal to 0.113 ± 0.005 for the same cosmology at r_{2500}. This agreement is particularly impressive in light of the fact that Allen et al. use a very different analysis technique to determine $f_{\rm gas}$. By assuming that the observed surface brightness profile is in HSE with a NFW dark matter potential, they determine the predicted temperature at a given radius and compare with a deprojected temperature profile from the data to get the best-fit gas and total mass profiles. Comparison of our mean results with theirs further suggests that simply excluding the central 100 kpc from the X-ray fit gives results consistent with a detailed modeling of the core, and that extrapolating the mass profile into the core has a negligible effect at r_{2500}. It is also interesting that they specifically select highly relaxed clusters, whereas our selection criteria are less stringent. The agreement in the mean supports the notion that most clusters are well-behaved and self-similar outside of the core.

Allen et al. (2004) present a larger sample of relaxed clusters, which partially encompasses the Allen et al. (2002) sample. They use the same analysis techniques on 26 clusters to obtain a mean $f_{\rm gas}$ of 0.117 ± 0.002. Although this result is slightly larger than ours, there is good agreement in $f_{\rm gas}$ between clusters that appear in both the Allen et al. (2004) dataset and the one presented here. This is illustrated in Figure 8 for the eight clusters in common between the two samples. The best-fit Allen gas mass fractions are subtracted from the best-fit $f_{\rm gas}$ values in this sample, and the difference is divided by the sum of the 68% statistical uncertainty for each measurement; any values outside of ± 1 in the figure would be inconsistent at 68%. Although the same data are used in both analyses, the weighting schemes are very different due to the differing analysis techniques and the 68% uncertainties are still used as a benchmark for comparison. As the figure shows, all values are consistent with one another, and there is no clear systematic offset. This eight cluster subsample consists of five cool core and three non-cool core clusters spanning a range in redshift from 0.14 to 0.89 and nearly an order of magnitude in total mass within r_{2500}. The finding of good agreement despite these wide-ranging properties and different analysis techniques further indicates the robustness of the 100 kpc-cut model.

Table 9—Continued

Cluster	$M_{\rm gas}^{\rm x\text{-}ray}(r_{2500})$ (10^{13} M$_\odot$)	$M_{\rm gas}^{\rm sze}(r_{2500})$ (10^{13} M$_\odot$)	$M_{\rm total}(r_{2500})$ (10^{14} M$_\odot$)	$f_{\rm gas}^{\rm x\text{-}ray}(r_{2500})$	$f_{\rm gas}^{\rm sze}(r_{2500})$	$t_{\rm cool}/t_{\rm H}$
MC1423	$2.26^{+0.10}_{-0.10}$	$2.63^{+0.44}_{-0.47}$	$1.94^{+0.20}_{-0.18}$	$0.116^{+0.006}_{-0.006}$	$0.135^{+0.029}_{-0.028}$	0.1
A1914	$4.85^{+0.12}_{-0.10}$	$5.11^{+0.42}_{-0.42}$	$4.82^{+0.30}_{-0.25}$	$0.100^{+0.003}_{-0.004}$	$0.106^{+0.011}_{-0.011}$	0.7
A1995	$3.51^{+0.14}_{-0.14}$	$4.33^{+0.28}_{-0.27}$	$4.74^{+0.50}_{-0.48}$	$0.074^{+0.005}_{-0.005}$	$0.092^{+0.013}_{-0.011}$	1.2
A2111	$2.19^{+0.27}_{-0.23}$	$2.15^{+0.42}_{-0.42}$	$2.49^{+0.56}_{-0.44}$	$0.088^{+0.008}_{-0.008}$	$0.085^{+0.026}_{-0.021}$	1.7
A2163	$8.08^{+0.21}_{-0.20}$	$5.89^{+0.55}_{-0.53}$	$5.49^{+0.24}_{-0.23}$	$0.147^{+0.003}_{-0.003}$	$0.107^{+0.011}_{-0.011}$	1.2
A2218	$3.00^{+0.13}_{-0.12}$	$4.10^{+0.38}_{-0.38}$	$3.33^{+0.31}_{-0.27}$	$0.090^{+0.004}_{-0.004}$	$0.123^{+0.017}_{-0.015}$	1.2
R1716	$1.23^{+0.19}_{-0.16}$	$1.32^{+0.28}_{-0.28}$	$1.39^{+0.45}_{-0.33}$	$0.088^{+0.013}_{-0.011}$	$0.093^{+0.034}_{-0.028}$	1.0
A2259	$1.81^{+0.14}_{-0.14}$	$1.65^{+0.61}_{-0.58}$	$1.79^{+0.27}_{-0.24}$	$0.101^{+0.007}_{-0.007}$	$0.092^{+0.036}_{-0.034}$	0.8
A2261	$3.04^{+0.20}_{-0.19}$	$3.58^{+0.40}_{-0.38}$	$2.56^{+0.36}_{-0.31}$	$0.119^{+0.008}_{-0.008}$	$0.139^{+0.026}_{-0.023}$	0.3
MS2053	$0.93^{+0.12}_{-0.12}$	$1.39^{+0.23}_{-0.22}$	$1.23^{+0.38}_{-0.29}$	$0.076^{+0.012}_{-0.011}$	$0.113^{+0.039}_{-0.030}$	0.9
MC2129	$3.26^{+0.30}_{-0.26}$	$3.28^{+0.34}_{-0.35}$	$2.82^{+0.57}_{-0.45}$	$0.116^{+0.011}_{-0.011}$	$0.116^{+0.027}_{-0.023}$	0.8
R2129	$2.58^{+0.16}_{-0.14}$	$2.17^{+0.33}_{-0.33}$	$2.08^{+0.27}_{-0.23}$	$0.124^{+0.008}_{-0.008}$	$0.104^{+0.022}_{-0.019}$	0.1
MC2214	$3.77^{+0.31}_{-0.28}$	$4.58^{+0.37}_{-0.37}$	$3.95^{+0.73}_{-0.58}$	$0.095^{+0.008}_{-0.008}$	$0.116^{+0.023}_{-0.021}$	0.9
MC2228	$2.81^{+0.24}_{-0.22}$	$3.84^{+0.35}_{-0.36}$	$2.03^{+0.31}_{-0.27}$	$0.138^{+0.009}_{-0.009}$	$0.188^{+0.035}_{-0.031}$	0.9

Table 10. SZE Masses and Gas Mass Fractions

Cluster	θ_c ($''$)	ΔT_0 (mK)	$M_{\rm gas}(r_{2500})$ ($10^{13}\,{\rm M}_\odot$)	$M_{\rm total}(r_{2500})$ ($10^{14}\,{\rm M}_\odot$)	$f_{\rm gas}(r_{2500})$
CL0016	$52.0^{+\ 9.0}_{-\ 8.1}$	$-1.449^{+0.088}_{-0.094}$	$4.65^{+0.42}_{-0.39}$	$2.83^{+0.32}_{-0.32}$	$0.165^{+0.033}_{-0.027}$
A267	$38.6^{+15.8}_{-12.8}$	$-0.735^{+0.084}_{-0.099}$	$2.74^{+0.68}_{-0.57}$	$1.99^{+0.25}_{-0.23}$	$0.137^{+0.054}_{-0.038}$
A370	$21.5^{+\ 9.3}_{-\ 7.4}$	$-1.072^{+0.144}_{-0.244}$	$2.58^{+0.47}_{-0.40}$	$3.18^{+0.22}_{-0.22}$	$0.081^{+0.021}_{-0.016}$
MS0451	$31.4^{+\ 7.1}_{-\ 6.4}$	$-1.610^{+0.100}_{-0.112}$	$5.03^{+0.83}_{-0.71}$	$3.46^{+0.32}_{-0.31}$	$0.145^{+0.039}_{-0.030}$
MC0647	$19.1^{+\ 8.1}_{-\ 6.6}$	$-1.390^{+0.151}_{-0.242}$	$2.81^{+0.72}_{-0.57}$	$6.21^{+0.86}_{-0.74}$	$0.045^{+0.018}_{-0.012}$
A 665	$56.8^{+23.5}_{-17.5}$	$-0.801^{+0.083}_{-0.105}$	$2.43^{+0.71}_{-0.53}$	$2.77^{+0.21}_{-0.29}$	$0.087^{+0.038}_{-0.023}$
A773	$30.9^{+11.7}_{-\ 9.8}$	$-0.985^{+0.109}_{-0.128}$	$2.56^{+0.67}_{-0.54}$	$3.12^{+0.23}_{-0.22}$	$0.082^{+0.027}_{-0.020}$
Zw3146	$29.4^{+11.9}_{-\ 9.7}$	$-1.223^{+0.177}_{-0.242}$	$3.95^{+0.82}_{-0.73}$	$3.43^{+0.17}_{-0.19}$	$0.115^{+0.030}_{-0.024}$
MS1137	$12.2^{+\ 8.4}_{-\ 4.4}$	$-1.021^{+0.301}_{-0.441}$	$2.09^{+0.38}_{-0.36}$	$0.96^{+0.15}_{-0.14}$	$0.221^{+0.064}_{-0.051}$
MC1149	$53.2^{+19.1}_{-16.6}$	$-1.181^{+0.127}_{-0.160}$	$3.00^{+0.42}_{-0.37}$	$2.17^{+0.55}_{-0.53}$	$0.139^{+0.059}_{-0.038}$
CL1226	$11.1^{+\ 8.2}_{-\ 4.5}$	$-2.171^{+0.677}_{-1.164}$	$2.82^{+0.63}_{-0.51}$	$5.08^{+1.05}_{-0.88}$	$0.056^{+0.026}_{-0.017}$
A1689	$25.2^{+\ 6.9}_{-\ 5.9}$	$-1.749^{+0.171}_{-0.213}$	$3.57^{+0.69}_{-0.57}$	$5.21^{+0.23}_{-0.23}$	$0.069^{+0.015}_{-0.012}$
R1347	$28.7^{+10.5}_{-\ 8.1}$	$-2.235^{+0.316}_{-0.429}$	$5.88^{+0.92}_{-0.85}$	$8.35^{+0.56}_{-0.56}$	$0.070^{+0.015}_{-0.013}$
A1835	$50.1^{+\ 9.2}_{-\ 8.2}$	$-1.590^{+0.112}_{-0.113}$	$6.20^{+0.93}_{-0.82}$	$5.38^{+0.34}_{-0.31}$	$0.115^{+0.024}_{-0.020}$
A1914	$29.4^{+11.3}_{-\ 8.9}$	$-1.776^{+0.200}_{-0.317}$	$4.33^{+0.96}_{-0.75}$	$4.69^{+0.18}_{-0.16}$	$0.092^{+0.023}_{-0.017}$
A1995	$34.6^{+\ 5.5}_{-\ 5.4}$	$-1.051^{+0.062}_{-0.063}$	$4.49^{+0.63}_{-0.57}$	$3.63^{+0.22}_{-0.21}$	$0.124^{+0.024}_{-0.020}$
A2163	$102.7^{+17.0}_{-15.1}$	$-1.898^{+0.276}_{-0.336}$	$7.57^{+1.61}_{-1.38}$	$6.17^{+0.38}_{-0.44}$	$0.123^{+0.036}_{-0.028}$
A2218	$79.0^{+13.6}_{-12.4}$	$-1.059^{+0.143}_{-0.176}$	$5.34^{+1.23}_{-1.03}$	$2.95^{+0.21}_{-0.20}$	$0.181^{+0.055}_{-0.042}$
A2261	$20.9^{+\ 9.8}_{-\ 7.5}$	$-1.179^{+0.148}_{-0.239}$	$2.46^{+0.75}_{-0.54}$	$2.91^{+0.27}_{-0.23}$	$0.084^{+0.031}_{-0.021}$
MC2214	$27.0^{+\ 8.2}_{-\ 6.9}$	$-1.523^{+0.160}_{-0.225}$	$4.41^{+0.63}_{-0.56}$	$3.99^{+0.42}_{-0.38}$	$0.110^{+0.028}_{-0.022}$
MC2228	$47.3^{+18.7}_{-15.5}$	$-1.315^{+0.137}_{-0.164}$	$3.91^{+0.65}_{-0.56}$	$2.15^{+0.40}_{-0.43}$	$0.182^{+0.076}_{-0.049}$

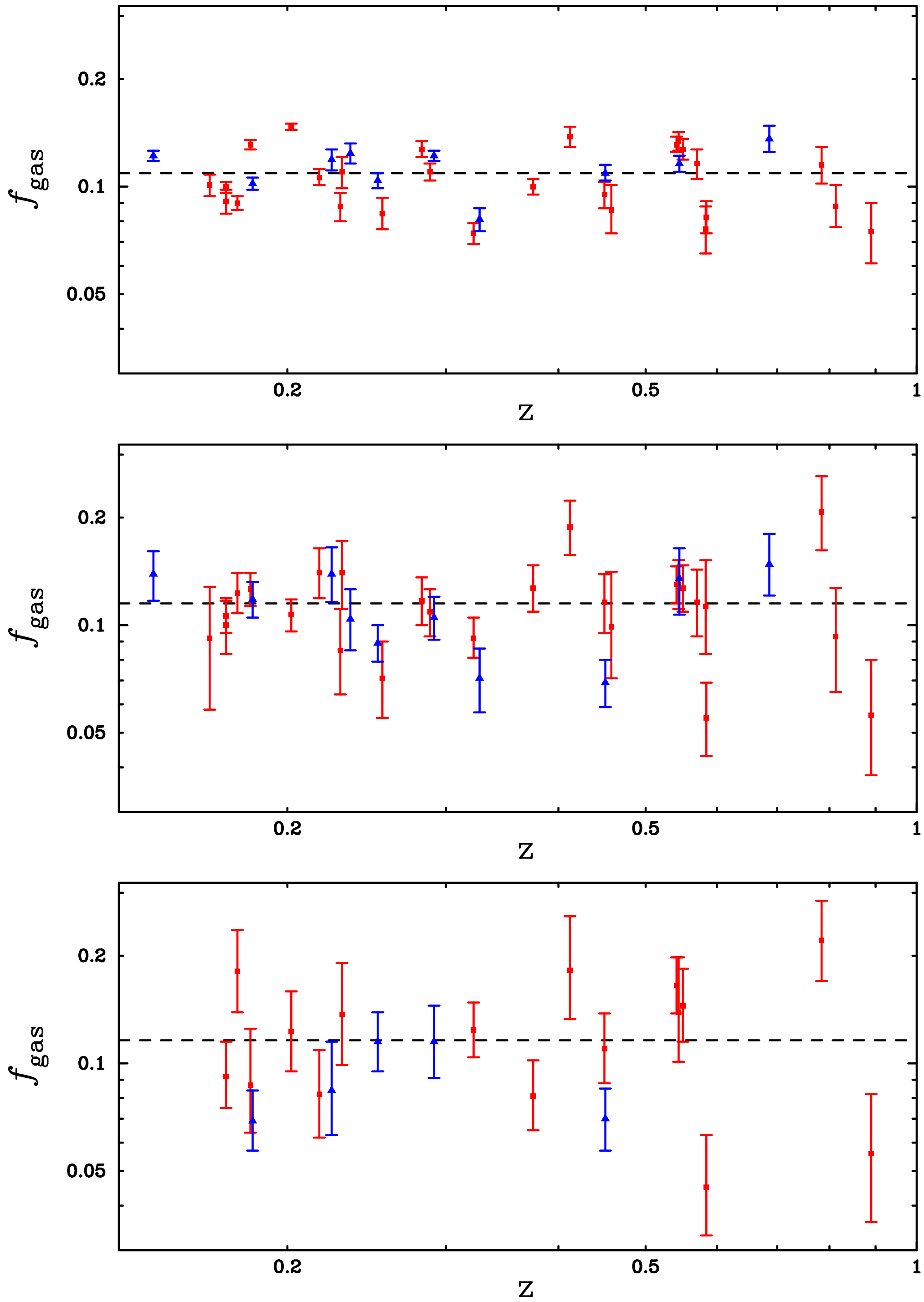

Fig. 7.— Gas mass fraction versus redshift results for the X-ray (top), SZE I (center), and SZE II (bottom) datasets. The dashed line shows the weighted mean f_{gas} for each sample. Cool core clusters are shown as blue triangles.

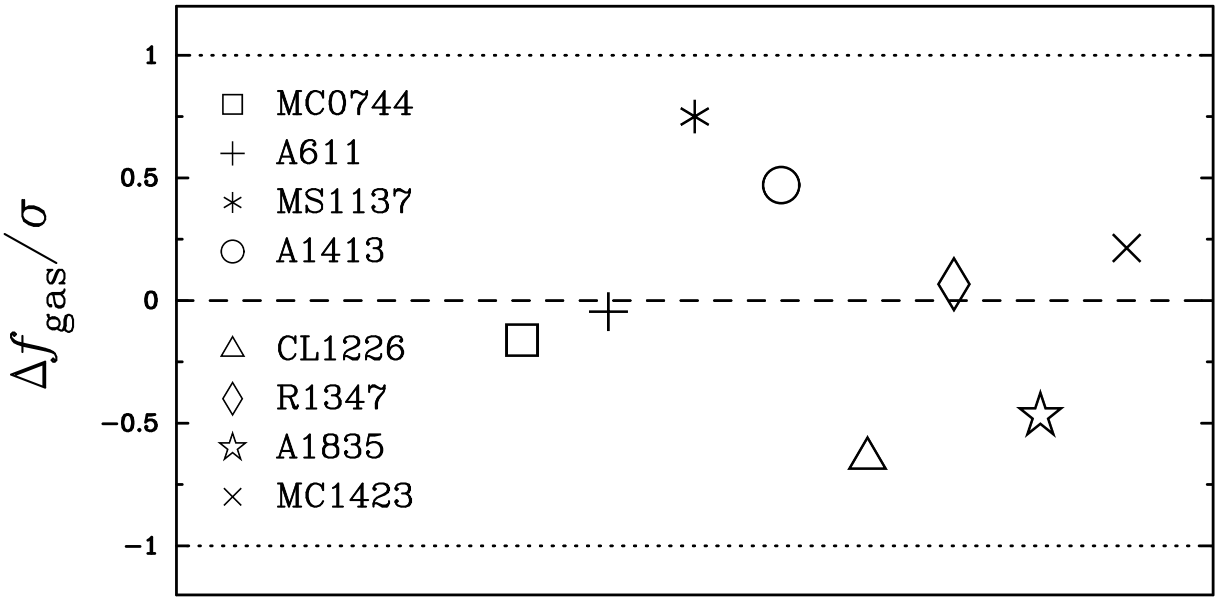

Fig. 8.— Gas mass fractions for the eight common clusters between this sample and the Allen et al. (2004) sample are compared. Plotted is the difference between the values presented here and the Allen values, divided by the difference allowed by the 68% uncertainties. All measurements are consistent at 68%, and no systematic trends are seen.

Although mean gas mass fraction results for other cluster samples are available in the literature (e.g., Evrard 1997; Mohr et al. 1999; Ettori et al. 2003; Sanderson et al. 2003), they are often calculated at different radii and assume different cosmologies, making detailed comparison with our results difficult. We do compare results with the SZE gas mass fraction results of Grego et al. (2001), since our cluster sample and analyses are similar. They also use BIMA and OVRO data, and 12 of our 21 SZE II clusters have data in common with their sample. They use spectroscopic temperatures from the literature (generally drawn from *ASCA*) and fit isothermal β-models to the u-v data, although they do not fix β. Scaling their $65''$ results to r_{500} with relations based on the results of Evrard et al. (1996) and Evrard (1997), they obtain a mean $f_{\rm gas}$ of $0.081^{+0.009}_{-0.011}\,h^{-1}$. We repeat this analysis on our 21 cluster SZE II sample, evaluating $f_{\rm gas}$ at $65''$ and scaling the results to r_{500} using the same relations. We obtain a mean $f_{\rm gas}$ of $0.086 \pm 0.007\,h^{-1}$, in good agreement with the Grego et al. results as we would expect.

Mean gas mass fractions for the X-ray, SZE I, and SZE II samples are consistent at the 68% level. The agreement between the X-ray and SZE gas mass fractions indicates a clumping factor C consistent with zero in our analysis. This factor, defined as $C \equiv \langle n_e^2 \rangle \,/\, \langle n_e \rangle^2$, reflects a possible bias in the X-ray surface brightness that could be caused by density inhomogeneities in the ICM. Such structures would increase the measured X-ray surface brightness by a factor of C relative to the SZE decrement (e.g., Mathiesen et al. 1999). The agreement suggests that the high resolution *Chandra* data allow us to remove clumps effectively before the data are fit, and any clumps below the noise level of the data have a negligible effect on the fits. We cannot rule out the possibility that this effect is cancelling with another systematic, and further constraints suggesting a negligible clumping factor are discussed in §6.7.

The agreement between the SZE I and SZE II datasets is further indication of how robustly the SZE is measured. The total mass calculations differ between the two datasets, with the SZE I total mass being driven by the 100 kpc-cut X-ray data and the SZE II total mass coming directly from the SZE with no data cut out. The agreement further suggests that the SZE is not highly sensitive to complicated core physics in clusters when measured on sufficiently large scales.

5.2. Cosmology From $f_{\mathbf{gas}}$

Having examined the mean gas mass fraction results and some of their implications for cluster structure, we focus now on their cosmological implications as described in the introduction. These cosmological tests can be carried out by fitting the data to the following model: (e.g., Allen et al. 2004):

$$f_{\rm gas}^{\rm mod}(z,\Omega_M,\Omega_\Lambda) = \frac{b\,\Omega_B}{(1+c)\Omega_M}\left(\frac{h_{\rm mod}D_{\rm A}{}^{\rm def}}{h_{\rm def}D_{\rm A}{}^{\rm mod}}\right)^{(3/2\,[\text{X-ray}],\,1\,[\text{SZE}])}. \tag{22}$$

Here b is a bias factor which accounts for the fact that the baryon fraction in clusters may not precisely equal Ω_B/Ω_M. The parameter c accounts for the fraction of baryons in the cluster that are not in the form of hot ICM gas observable in X-ray or SZE; c is defined as the ratio of baryonic mass in forms other than hot gas to the hot gas mass.

The cosmological analysis is divided three parts. We first examine the constraints on Ω_M obtained by assuming that the correct $D_{\rm A}$ is used and fitting only the first term of Eq. [22] to the X-ray and SZE $f_{\rm gas}$ distributions. We use a well-established measurement for Ω_B and experiment with two very different sets of b and c drawn from the literature. Next, we ignore all information about Ω_B, b, and c and fit only the second term of Eq. [22] to the data using an arbitrary normalization. This gives us information on Ω_M and Ω_Λ from the shape of the $f_{\rm gas}(z)$ distribution only. We then combine these two approaches, fitting the $f_{\rm gas}$ data to Eq. [22] to obtain cosmological information from an approach that combines the methods of the first two sections. Finally, in §5.3 we examine what constraints can be placed on cluster structure by using as priors cosmological constraints obtained from other experiments.

To obtain constraints on Ω_M from the the $f_{\rm gas}$-z normalization, the X-ray data and both SZE datasets are fit to the model function

$$f_{\rm gas}^{\rm mod}(\Omega_M, \Omega_\Lambda) = \frac{b\,\Omega_B}{(1+c)\Omega_M}. \tag{23}$$

Our sample extends to high redshift, and the change in $D_{\rm A}$ for different cosmologies will lead to different calculated gas mass fractions. We therefore recalculate $f_{\rm gas}$ for the entire sample for each new cosmology tested so as to avoid biasing the results toward getting back out the same cosmology we put in (Grego et al. 2001). We marginalize over the *WMAP* total density prior $\Omega_M + \Omega_\Lambda = 1.02 \pm 0.02$ (Spergel et al. 2003) and, following Allen et al. (2004), we adopt Gaussian priors on the quantities Ω_B and b and marginalize over them as well. These priors are marginalized by gridding over a range as large as the uncertainties.

For Ω_B we adopt the *WMAP* result $\Omega_B h^2 = 0.0224 \pm 0.0009$ (Spergel et al. 2003) and use the *Hubble Space Telescope* constraint $h = 0.72 \pm 0.08$ (Freedman et al. 2001) which includes systematic uncertainty. For completeness, two different scenarios are treated for the bias factor b and amount of additional baryons not in gas, c. These two b and c scenarios are by no means the only reasonable choices, but are chosen because they are motivated by two very different physical pictures derived from different types of simulations. First, for consistency with the Allen et al. (2004) results, we adopt a bias factor $b = 0.824 \pm 0.033$ based on the N-body/gasdynamical simulations of Eke et al. (1998) and a non-gas baryonic ratio $c = 0.19\,h^{3/2}$ from a study of the Coma cluster by White et al. (1993).

The second scenario uses more recent results for b and c, drawn from simulations generated with an Adaptive Refinement Tree (ART) N-body+gasdynamics code (Kravtsov 1999; Kravtsov et al. 2002). The simulated clusters include radiative cooling and UV heating, star formation, and stellar feedback processes in addition to the standard baryonic gas dynamics, and the baryon distribution is very different from that determined by simulations that neglect cooling. Kravtsov et al. (2005) find that cooling and star formation redistribute baryons throughout the cluster and that the factors b and c are therefore radially dependent. The most massive cluster in their analysis is similar to the clusters in our sample, with a total mass within r_{2500} equal to $2.78 \times 10^{14}\,h^{-1}\,{\rm M}_\odot$ and a mean spectroscopic temperature of 8.6 keV; we therefore adopt the b and c values associated with this cluster. Kravtsov et al. find a bias factor $b(< r_{2500}) = 1.06$ for this cluster; the redistribution of cluster baryons due to cooling and star formation in the core actually drives the cluster baryon fraction above the universal value. They also find a ratio of non-gas baryonic mass to gas mass of 0.89, much higher than the White et al. (1993) Coma result. No statistical uncertainties on b or c are as yet available since they are drawn from only one cluster. Any statistical uncertainty on the Ω_M result is therefore likely to be underestimated.

The gas mass fraction data are converted to log space to account for the fractional nature of the uncertainties, and the fit is performed using the model of Eq. [23] and the appropriate priors. Results for all three datasets, X-ray, SZE I, and SZE II, are shown in Table 11. The results are consistent with the *WMAP* constraint $0.268^{+0.016}_{-0.018}$ for $h = 0.71$ (Spergel et al. 2003), and as mentioned earlier the statistical uncertainty for the Kravtsov et al. b and c result is likely understated. As will be seen in §6.4, the systematic uncertainty in $M_{\rm total}$ is substantial and we estimate that it may be underestimated by up 30% in our analysis. More must be understood about this systematic and the b and c parameters before we can place precision cosmological constraints on Ω_M.

We now examine the case in which we derive cosmological constraints from the shape of the $f_{\rm gas}$-z distribution, with no specific information about the normalization. The shape of the curve depends only on the assumed angular diameter distance, so parameters such as Ω_B, h, and the poorly known b and c are ignored, and systematic uncertainty in the mass should not strongly affect the results if it is reasonably consistent from cluster to cluster. We fit the parameters N, $\Omega_M^{\rm mod}$, and $\Omega_\Lambda^{\rm mod}$ to the data with the model function

$$f_{\rm gas}^{\rm mod}(z) = N \left(\frac{D_{\rm A}(z, \Omega_M^{\rm def}, \Omega_\Lambda^{\rm def})}{D_{\rm A}(z, \Omega_M^{\rm mod}, \Omega_\Lambda^{\rm mod})} \right)^{(3/2\,[\text{X-ray}],\ 1\,[\text{SZE}])} \tag{24}$$

where N is an arbitrary normalization and the "default" cosmology is $\Omega_M = 0.3$, $\Omega_\Lambda = 0.7$.

This method is tested on the X-ray data, with Ω_M and Ω_Λ each being gridded between 0 and 1.3, and N free to find its best fit value. Results for the cosmological parameters are reported in the first column of Table 12, showing that the data cannot constrain cosmology from shape information alone. We therefore again adopt the same prior on the geometry of the universe that we used when treating the $f_{\rm gas}$-z normalization above; the results of marginalizing over this prior are shown in the second column of Table 12. The cosmological parameters are now constrained by the data, but statistical uncertainties are large. We conclude that, given our ability to infer cluster properties from the data, this method cannot yet provide tight constraints on cosmological parameters. However, the results are consistent with independent tests, such as *WMAP*, and inconsistent with some flat cosmological models such as Standard Cold Dark Matter (SCDM,Ω_M=1,Ω_Λ=0).

The qualitative nature of this behavior is illustrated in Figure 9, where the top panel shows the X-ray gas mass fractions calculated with the default cosmology along with fits to the X-ray data for several different cosmologies. The dark solid line shows the best fit using the *WMAP* prior. The dashed green line is plotted using the unconstrained "best-fit" values from the first column of Table 12. Comparison of the green and black lines,

Table 11. Results of Fits to $f_{\rm gas}$ Normalization

Dataset	$b = 0.824, c = 0.19h^{3/2}$[a]	$b = 1.06, c = 0.89$[b]	$\chi^2_{\rm red}$
X-ray	$\Omega_M^{\rm bf} = 0.31^{+0.04}_{-0.03}$	$\Omega_M^{\rm bf} = 0.23^{+0.02}_{-0.02}$	0.8
SZE I	$\Omega_M^{\rm bf} = 0.30^{+0.05}_{-0.04}$	$\Omega_M^{\rm bf} = 0.22^{+0.03}_{-0.03}$	1.5
SZE II	$\Omega_M^{\rm bf} = 0.32^{+0.05}_{-0.05}$	$\Omega_M^{\rm bf} = 0.23^{+0.03}_{-0.03}$	2.0

[a] b and c chosen for consistency with Allen et al. (2004).

[b] b and c from Kravtsov et al. (2005).

Table 12. Results of Fits to $f_{\rm gas}$ Shape

Dataset	no prior[a]	*WMAP* prior $\Omega_{\rm tot} = 1.02$
X-ray	$\Omega_M^{\rm bf} = 0.00^{+0.68}_{-0.00}$, $\Omega_\Lambda^{\rm bf} = 0.26^{+1.04}_{-0.26}$	$\Omega_M^{\rm bf} = 0.26^{+0.22}_{-0.15}$, $\Omega_\Lambda^{\rm bf} = 0.76^{+0.15}_{-0.22}$
SZE I	$\Omega_M^{\rm bf} = 0.86^{+0.44}_{-0.86}$, $\Omega_\Lambda^{\rm bf} = 1.30^{+0.00}_{-1.30}$	$\Omega_M^{\rm bf} = 0.36^{+0.47}_{-0.22}$, $\Omega_\Lambda^{\rm bf} = 0.66^{+0.22}_{-0.47}$

[a] Results are unconstrained by the data.

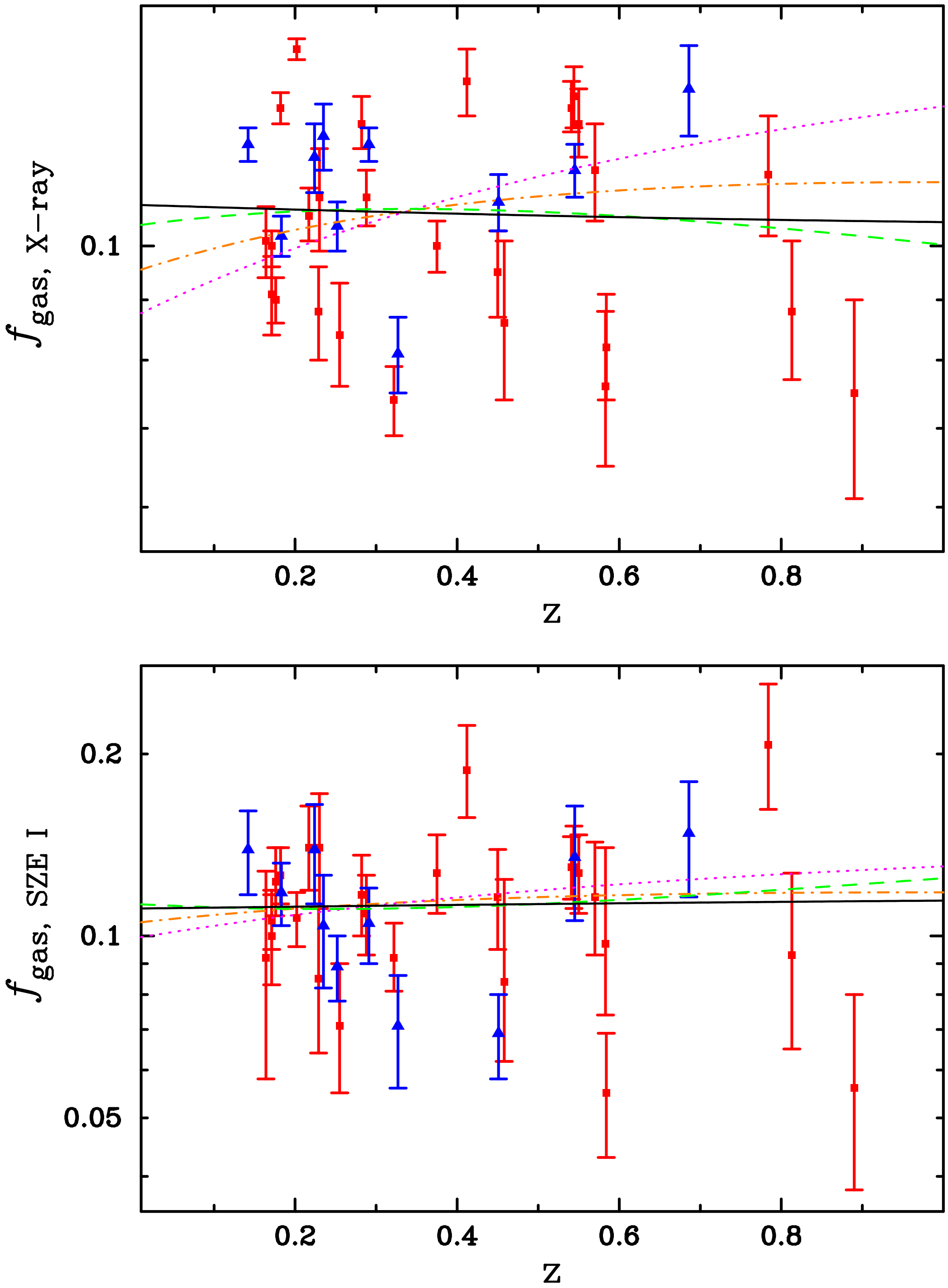

Fig. 9.— Gas mass fraction versus redshift for X-ray (top) and SZE I (bottom) data, showing best fit models for different cosmologies. The dark solid lines show the best fit cosmologies when the prior $\Omega_M + \Omega_\Lambda = 1.02$ is assumed. The dashed green lines show the best fit cosmologies when no prior is assumed. Refer to Table 12 for best fit results. The dash-dotted orange line shows the best fit normalization when an oCDM cosmology (Ω_M=0.3,Ω_Λ=0) is assumed, and the dotted magenta line shows the best fit normalization for the SCDM cosmology (Ω_M=1.0,Ω_Λ=0).

which correspond to very different combinations of Ω_M and Ω_Λ, shows that the data are not sufficiently sensitive to distinguish between degeneracies in Ω_M and Ω_Λ. However, the figure does show that some fiducial cosmologies are disfavored by the data. This is particularly true of the SCDM cosmology which is indicated by the dotted magenta line. Although already ruled out by the *WMAP* density prior, the open Cold Dark Matter (oCDM) cosmology (Ω_M=0.3,Ω_Λ=0), which is denoted by the dash-dotted orange line, also does not appear to be a very good fit at high redshift.

Repeating this analysis with the SZE I sample, we again find that the model is unconstrained without a prior (Table 12). Introducing the same prior on $\Omega_M + \Omega_\Lambda$, however, we are again able to constrain Ω_M and Ω_Λ with similar overall behavior. The best fit model is consistent with the *WMAP* constraints, and flat cosmologies such as SCDM are excluded. The lower panel of Figure 9 shows the default SZE gas mass fractions with fits from several cosmologies overlaid. It is much more difficult to distinguish between cosmologies in the SZE data. This is a result of two major factors; first, the uncertainties in the SZE data are simply larger than those in the X-ray data because the decrement is not measured to nearly the same significance as the X-ray surface brightness. Second, since the SZE derived $f_{\rm gas}$ goes linearly with $D_{\rm A}$ instead of as ${D_{\rm A}}^{3/2}$, the behavior of the different cosmologies at high redshift is more difficult to distinguish. It is therefore quite remarkable that the SZE data are capable of distinguishing at all between a ΛCDM and SCDM universe. Note that the differing $D_{\rm A}$ dependences can be used to solve for the angular diameter distances and subsequently H_0 (e.g. Birkinshaw et al. 1991; Mason et al. 2001; Reese et al. 2002); results from this sample will be presented in a separate work (Bonamente et al., in preparation).

Finally, we note that meaningful cosmological constraints cannot be derived from the SZE II dataset, even using the *WMAP* prior. This is presumably due to the larger measurement uncertainties combined with the smaller sample size, and no SZE II results are presented here.

The shape and normalization methods are now combined to obtain a more complete picture of the cosmological constraints available from studying gas mass fractions. The data are fit to Eq. [22] with no assumed prior on the geometry of the universe, in the hope that combining the shape and normalization information will give non-zero constraints on Ω_Λ without a strong density prior. It is not necessary to recalculate gas mass fractions for each choice of cosmology as we did in treating the normalization, since the model of Eq. [22] accounts for a "default" input cosmology; this is again taken to be a ΛCDM cosmology. The results of using both the Allen et al. (2004) and Kravtsov et al. (2005) values of b and c are shown in Table 13. Although the SZE II sample provides nearly the same results on Ω_M as it did above when only the normalization was considered, it again provides no useful constraints on Ω_Λ and is not treated here.

For the X-ray data, the Ω_M results are nearly identical to those presented in Table 11, since it is the same normalization of $f_{\rm gas}$ versus z that drives the Ω_M fits. With this strong constraint on Ω_M, we are able to derive non-zero constraints on Ω_Λ without using the *WMAP* total density prior. The data and best fit model are shown in Figure 10. The best fit value of Ω_Λ is lower when the priors from Kravtsov et al. (2005) are used relative to results using the Allen et al. priors. This reflects a correlation between Ω_M and Ω_Λ when measuring distances; at redshifts $z < 1$, $D_{\rm A}$ is inversely proportional to Ω_M, but directly proportional to Ω_Λ (e.g., Kolb & Turner 1990). When Ω_M decreases with the larger b and c, Ω_Λ must also decrease in order to maintain the same $D_{\rm A}$ behavior at high z. Results of fits to the SZE I gas mass fractions are also shown in Table 13. We cannot yet obtain non-zero constraints on Ω_Λ from the SZE data alone. The best fit results, however, are similar to those of the X-ray data and the best-fitting model is shown along with the data in Figure 10. When the *WMAP* density prior is imposed, the SZE results are $\Omega_M = 0.29^{+0.05}_{-0.03}$, $\Omega_\Lambda = 0.73^{+0.03}_{-0.05}$ for b and c from Allen et al. (2004), and $\Omega_M = 0.23^{+0.02}_{-0.03}$, $\Omega_\Lambda = 0.79^{+0.03}_{-0.02}$ for the Kravtsov et al. (2005) b and c values.

Since our analysis method is very similar to that of Allen et al. (2004), it is interesting to compare our results with theirs. The two samples have only eight clusters with common data, and we look for agreement between the best fit results. For consistency with their method, we use the same b, c, and h priors but adopt an older, BBN determined value $\Omega_B h^2 = 0.0214 \pm 0.0020$ from Kirkman et al. (2003). Adopting this revised prior and refitting the data, we obtain the constraints $\Omega_M = 0.30^{+0.04}_{-0.04}$, $\Omega_\Lambda = 0.67^{+0.47}_{-0.51}$. These are compared to the Allen et al. (2004) results, $\Omega_M = 0.25^{+0.04}_{-0.04}$, $\Omega_\Lambda = 0.96^{+0.19}_{-0.22}$. While the results are consistent, the Allen Ω_M is lower than ours, likely due to the mild ($\sim 7\%$) offset in mean

Table 13. Results of Fits to $f_{\rm gas}$ vs. z Normalization and Shape

Dataset	$b = 0.824$, $c = 0.19h^{3/2}$	$b = 1.06$, $c = 0.89$
X-ray	$\Omega_M^{\rm bf} = 0.31^{+0.04}_{-0.04}$, $\Omega_\Lambda^{\rm bf} = 0.74^{+0.43}_{-0.56}$	$\Omega_M^{\rm bf} = 0.24^{+0.02}_{-0.03}$, $\Omega_\Lambda^{\rm bf} = 0.61^{+0.45}_{-0.58}$
SZE I	$\Omega_M^{\rm bf} = 0.30^{+0.04}_{-0.03}$, $\Omega_\Lambda^{\rm bf} = 0.62^{+0.55}_{-0.62}$	$\Omega_M^{\rm bf} = 0.23^{+0.02}_{-0.02}$, $\Omega_\Lambda^{\rm bf} = 0.46^{+0.60}_{-0.46}$

[a] b and c chosen for consistency with Allen et al. (2004).

[b] b and c from Kravtsov et al. (2005).

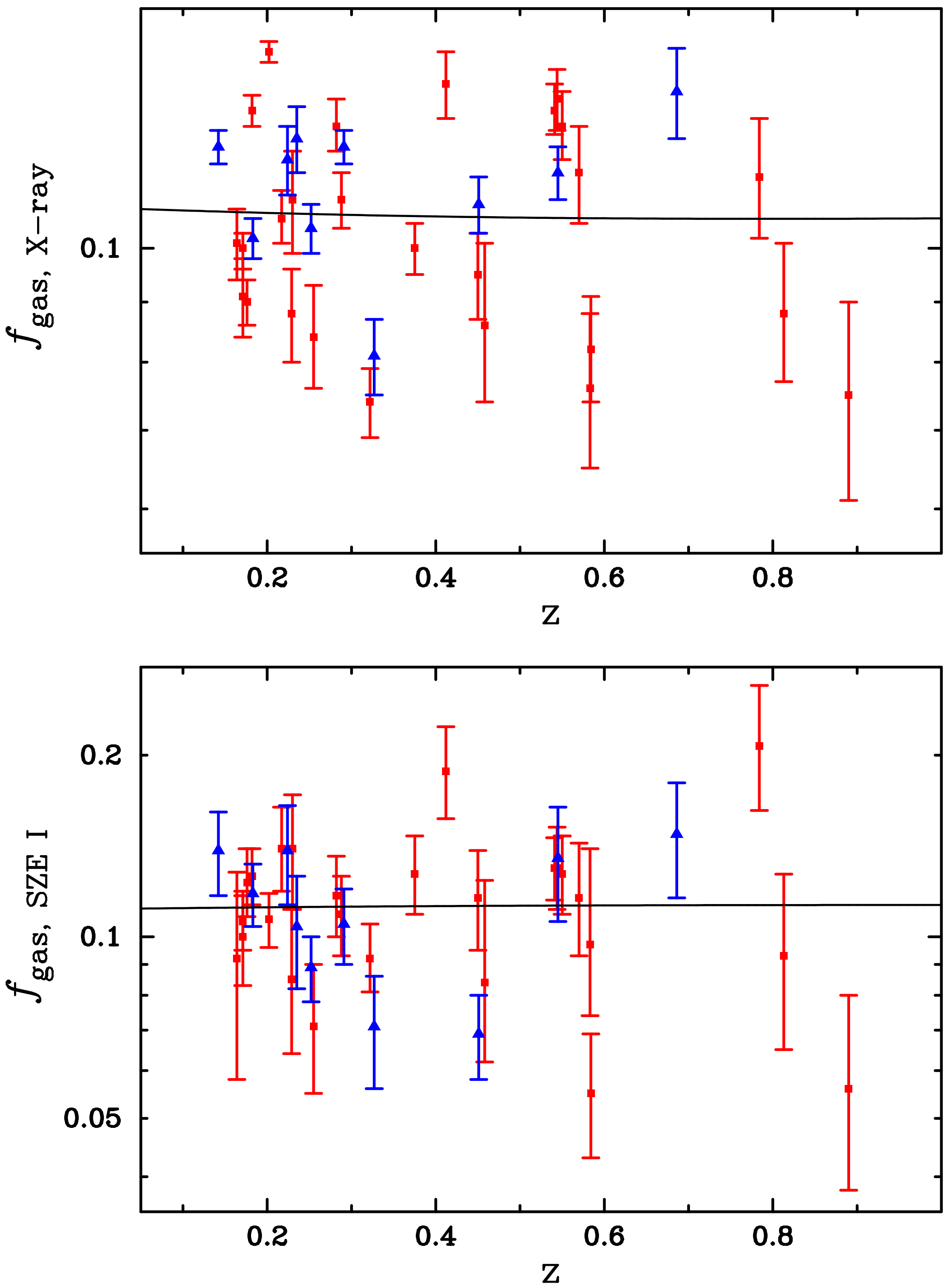

Fig. 10.— Gas mass fraction versus radius for X-ray (top) and SZE I (bottom) data, showing best fit models when both the shape and normalization information of the $f_{\rm gas}$ versus z are combined. The gas mass fractions were calculated assuming a ΛCDM cosmology, and best fit cosmological parameters can be found in Table 13.

gas mass fractions. The larger Ω_Λ in the Allen results is not so easily explained; if anything we would expect to find a smaller Ω_Λ based on the correlation described above.

We also note, however, that the Allen results are calculated assuming a SCDM cosmology as the default, with $\Omega_M = 1.0$, $\Omega_\Lambda = 0.0$, and $h = 0.5$. Recalculating our gas mass fractions assuming this same cosmology and again fitting Eq. [22] to the data we find $\Omega_M = 0.31^{+0.04}_{-0.03}$, $\Omega_\Lambda = 0.95^{+0.33}_{-0.49}$. While Ω_M is unchanged, Ω_Λ increases substantially and the best-fit value is in better agreement with the Allen results. The reason for this discrepancy appears to be in the calculation of r_{2500}, within which the gas mass fractions are computed. Because it depends on the critical density, the radius $r_{2500} \propto [{H_0}^2 E^2(z)]^{-1/2}$ where

$$E^2(z) \equiv \Omega_M(1+z)^3 + (1 - \Omega_M - \Omega_\Lambda)(1+z)^2 + \Omega_\Lambda. \tag{25}$$

For small z the lower value of h assumed in SCDM leads to a larger r_{2500} than would be obtained for ΛCDM. The opposite situation is true at large z, however; the increase in $E^2(z)$ due to the larger Ω_M overcompensates the smaller h, and a smaller r_{2500} is obtained for SCDM relative to ΛCDM. The gas mass fraction in clusters increases with radius (e.g., David et al. 1995; Evrard 1997; Frenk et al. 1999) so the SCDM assumption leads to larger $f_{\rm gas}$ values at small z and smaller $f_{\rm gas}$ values at large z compared to ΛCDM. The result is a steepening of the $f_{\rm gas}$-z curve relative to the ΛCDM case. The smaller $f_{\rm gas}$ values at high z mean that the best fit model prefers a larger value of $D_{\rm A}$, which is obtained by increasing Ω_Λ.

Because our default ΛCDM cosmology is similar to the best-fit cosmologies of Table 13, the level of bias due to this effect is small in our results. For instance, the difference between the derived physical r_{2500} for the ΛCDM cosmology versus that derived using the best-fit cosmologies of Table 13 is generally less than 2%, corresponding to a change of less than 1% in $f_{\rm gas}$. By contrast, the difference between the derived r_{2500} for the SCDM cosmology versus that derived using the corresponding best-fit cosmology quoted above is as much as 30%. This can cause the measured $f_{\rm gas}$ to change by as much as 10% due only to the different measurement radius. As a final test, we recalculate the best-fit cosmology assuming the b and c values from Allen et al. (2004) but using as our default cosmology the best-fit results Ω_M=0.31, Ω_Λ=0.74 from Table 13, and assuming $h = 0.72$. The new best-fit cosmology is $\Omega_M = 0.31^{+0.04}_{-0.04}, \Omega_\Lambda = 0.72^{+0.43}_{-0.58}$, virtually identical to the results obtained when a ΛCDM cosmology is used as the default.

5.3. Constraints on Clusters from Cosmology

The results of the previous section are highly sensitive to two poorly known quantities, b and c, which describe the baryon budget in clusters. We conclude this section by using current cosmological constraints from the CMB as priors to determine what we can we learn about the cluster baryon budget. The cosmological constraints from CMB experiments are stronger than those that cluster studies currently provide. The results of *WMAP* data combined with finer scale experiments show very tight constraints on cosmological parameters, finding $\Omega_B h^2 = 0.0224 \pm 0.0009$ and $\Omega_{\rm tot} = 1.02 \pm 0.02$ and constraining the matter density as $\Omega_M h^2 = 0.135^{+0.008}_{-0.009}$ (Spergel et al. 2003). We perform analysis similar to that of §5.2, but instead of fixing b and c, we fix Ω_B and Ω_M to the *WMAP* values and fit for the ratio $b/(1+c)$. The gas mass fractions are calculated assuming Ω_M=0.3, Ω_Λ=0.7, $h = 0.7$, which are very similar to the *WMAP* constraints so no significant bias in the results is expected. The results for each dataset are shown in Table 14.

The results show that the measured gas mass fraction in clusters within r_{2500} accounts for $\sim$ 65% of the ratio Ω_B/Ω_M. Although this is higher than what recent cooling simulations show (e.g., Kravtsov et al. 2005), it is consistent with the results of recent observational studies which report mean $f_{\rm gas}$ values in the range 50—70% of Ω_B/Ω_M, over radii from r_{2500} to r_{200} (Mohr et al. 1999; Sanderson et al. 2003; Ettori et al. 2003; Allen et al. 2004). However, given the still sizable systematic uncertainties in these measurements (§6) combined with widely varying constraints on the b and c factors, advances in both simulation and observation are needed before comparing the measured $f_{\rm gas}$ with Ω_B/Ω_M can be used to obtain precision cosmological results. Although no constraints on b or c are needed to constrain cosmology using the $f_{\rm gas}(z)$ shape method, our ability to model the data and extract constraints on $f_{\rm gas}$ is not yet at a level that we can easily distinguish between the $f_{\rm gas}$-z curves for different cosmologies.

In summary, we have demonstrated that clusters are sufficiently well behaved that stud-

Table 14. Results of Fits to $f_{\rm gas}$ Normalization

Dataset	$\frac{b}{(1+c)}$	$\chi^2_{\rm red}$
X-ray	0.64 ± 0.03	1.2
SZE I	0.66 ± 0.03	1.9
SZE II	0.64 ± 0.04	2.5

ies of $f_{\rm gas}$ provide cosmological constraints that agree with results of independent cosmological probes. We conclude on the slightly more cautious note that, based on the sensitivity of the results to the assumed baryon budget and in light of the systematics discussed in the next section, the rich physics in clusters must be better understood through advances in both observation and theory, as well as implementation of more complex data modeling, before the $f_{\rm gas}$ methods discussed here can be used for precision cosmological constraints.

6. Systematic Uncertainties

We now address sources of systematic uncertainty that may affect the results reported here. The first systematics considered, instrument calibration, measurement of X-ray background, and point source contamination, involve observational effects. We then consider systematics that involve the modeling of clusters, namely mass calculation, selection biases, temperature structure, and cluster substructure.

6.1. Instrument Calibration

The absolute calibration of the ACIS response is uncertain at the 7% level[7], after CTI corrections and correction for contamination on the optical blocking filters are applied. Although no spatially dependent effective area correction is applied to the *Chandra* exposure maps, this is found to affect the data at a level of only $\sim 1\%$. The *Chandra* calibration uncertainty then translates to $\sim 4\%$ uncertainty in the X-ray gas mass, since density goes as square root of the surface brightness. This calibration applies at all energies, so will have no effect on T_x which depends only on the shape of the spectrum. Since r_c and β are not affected either, the uncertainty has no effect on total cluster mass. Absolute calibration of the BIMA/OVRO interferometric imaging system is known conservatively to 4% (Reese 2001), which translates directly to a 4% uncertainty in the SZE derived gas mass, which is linearly proportional to ΔT_0.

6.2. X-ray Background

X-ray backgrounds for clusters in our sample are determined using the method described in §3.1. In general background regions are chosen to be as far from a cluster as possible.

[7]Information on the *Chandra* calibration is available at http://cxc.harvard.edu/cal/

However, because cluster emission falls off as a power law, it is difficult to determine precisely where it becomes insignificant relative to the background. It is possible, then, that the background regions chosen could contain some amount of cluster flux, particularly for low-z clusters which subtend a larger solid angle on the sky. The effect of overestimating the X-ray background due to cluster contamination is tested on the cluster Zw3146. This cluster is on chip I3, so the original background is extracted from circular regions on chips I0, I1, and I2 at appropriate distances from the readouts (e.g., Bonamente et al. 2004). The result obtained is $B_x = 6.33 \pm 0.13 \times 10^{-6}$ cts cm^{-2} arcmin^{-2} s^{-1}. To test the effect of overestimating the background, we move the extraction regions closer to the cluster until the best-fit background increases by $\sim 25\%$ due to cluster contamination. We redo the spectral fits with these new background regions, and use the resulting temperature and higher background level in the X-ray/SZE jointfit.

The fit results are provided in Table 15. A higher background trades off with a lower central surface brightness. ??wever, since the total flux of the cluster is not changed, θ_c and β change to offset the decrease in S_{x0}. These changes are small enough that any corresponding change in ΔT_0 is negligible. As for the spectral temperature, the inclusion of more cluster photons in the background spectrum leads to an oversubtraction of soft X-ray emission, since the detected cluster emission peaks around 1 keV. The resulting cluster spectrum is therefore harder, which biases the temperature higher.

The impact of these changes on the inferred cluster properties are provided in Table 16, where properties are again measured at r_{2500}. As was shown in §4.4, the X-ray and SZE-derived gas masses are robustly measured quantities and change very little between the two cases. The total mass is driven up by the increases in β and T_x, leading to a decrease in the gas mass fraction, in this case by $\sim 7\%$.

Table 15. Fit Parameters for Different Background Levels

Background	S_{x0}[a]	θ_c ($''$)	β	ΔT_0 (mK)	T_x (keV)
original	$2.13^{+0.09}_{-0.08} \times 10^{-3}$	$30.4^{+0.9}_{-0.9}$	$0.736^{+0.009}_{-0.009}$	$-1.17^{+0.14}_{-0.14}$	$8.28^{+0.30}_{-0.29}$
25% high	$2.02^{+0.08}_{-0.08} \times 10^{-3}$	$32.6^{+1.0}_{-1.0}$	$0.769^{+0.011}_{-0.010}$	$-1.16^{+0.14}_{-0.13}$	$8.50^{+0.32}_{-0.32}$

[a]Units are cts cm^{-2} arcmin^{-2} s^{-1}.

An increase in the background of 25% should be close to an upper limit, and would only apply to a small number of bright, nearby clusters in our sample. It may seem like a poor representation to perform this test on a bright cluster such as Zw3146, whose central surface brightness is several hundred times more intense than the background, even with the core removed. This test is therefore repeated with the cluster A2259, which has a much smaller central surface brightness to background ratio ($S_{x0}/B_x \sim 50$). The results are much the same with $f_{\rm gas}$ decreasing by $\sim$ 10%. We conclude that the X-ray data in our sample have sufficient signal to noise that overestimating the background has a very small effect on the derived results. In §4.3, it was pointed out that we fix B_x in the cluster fits to avoid degeneracies with S_{x0}. Given that typical statistical uncertainty in B_x is at most $\sim$ 5%, much less than the 25% case examined here, ignoring the statistical uncertainty in the background should have a negligible effect on the results.

6.3. Radio Point Source Contamination

Point sources are identified in the data using images from DIFMAP, as described in §3.2. All cluster fields are also cross-referenced with 1.4 GHz maps from the NRAO VLA Sky Survey (NVSS) (Condon et al. 1998). Most point sources have spectra that decline with frequency between 1.4 and 30 GHz (e.g., Taylor et al. 2001), so the presence of a point source in the NVSS map does not mean that it will be detectable at 30 GHz. However, the NVSS maps occasionally allow us to distinguish faint point sources with flat or gently declining spectra from the noise in the 30 GHz maps.

Not accounting for a point source can cause the SZE decrement to be "filled in" by the point source flux, and the magnitude of the decrement is typically diminished. This would lead to a lower derived density and, subsequently, a lower gas mass and gas mass fraction. It is possible to overestimate the magnitude of the decrement if the point source falls in a

Table 16. Inferred Parameters for Different Background Levels

Background	$M_{\rm gas}^{\rm x\text{-}ray}$ (10^{13} M$_\odot$)	$M_{\rm gas}^{\rm sze}$ (10^{13} M$_\odot$)	$M_{\rm total}$ (10^{14} M$_\odot$)	$f_{\rm gas}^{\rm x\text{-}ray}$
original	$4.42^{+0.11}_{-0.11}$	$3.80^{+0.47}_{-0.47}$	$3.62^{+0.22}_{-0.20}$	$0.122^{+0.004}_{-0.004}$
25% high	$4.53^{+0.11}_{-0.11}$	$3.86^{+0.44}_{-0.46}$	$4.00^{+0.25}_{-0.25}$	$0.113^{+0.005}_{-0.004}$

negative beam sidelobe; however, these sidelobes are weak relative to the beam center so the effect of overestimating ΔT_0 would be smaller. The most severe systematic would be associated with an undetected point source directly on center, where the instrument response is strongest.

For cases in which NVSS shows a bright source that does not show up at 30 GHz, we place a point source model at the NVSS position and marginalize over its flux. We do not find any instances in which NVSS shows a bright on-center point source that does not appear at all at 30 GHz. The main danger then lies in the presence of a point source with an inverted spectrum that is masked by the noise in a map. Such a source would not necessarily show up in NVSS data if it had a sufficiently inverted spectrum. Such sources should be very rare, however; Cooray et al. (1998) compare fluxes of 55 point sources at wavelengths of 1 cm (BIMA/OVRO) and 20 cm (VLA); many also have 2 cm and 6 cm fluxes from the VLA. Only three are found to have inverted spectra, and the spectral indices are all mild ($\alpha \geq -0.61$ where the point source flux $S \propto \nu^{-\alpha}$).

NVSS contains only point sources with fluxes greater than 2 mJy at 1.4 GHz. To test the effect of point sources too faint to be cross-correlated with NVSS, LaRoque et al. (2002) randomly distribute point sources in the field of the cluster A2163 according to a number count versus flux density relationship calibrated from 41 clusters observed with BIMA. Considering undetected point sources with intrinsic fluxes between 10 μJy and 300 μJy at 30 GHz, they find that the decrement can change by $\pm 4\%$.

Most clusters do have massive central galaxies known as cD galaxies, and many of these are radio bright. LaRoque et al. (2002) include a point source model at the optical position of the cD galaxy in A2163 and marginalize over its flux. They find a change in the best-fit central decrement of 7%, although the best-fit point source flux is consistent with zero. Reese (2001) uses a similar treatment, placing point source models at the centers of the clusters A697, A2261, and A1413. The best-fit fluxes are all consistent with zero, and alter ΔT_0 at the level of only $\sim 2\%$. We conclude then that the effect of undetected point sources on the central decrement is likely to be at the level of $\sim 5\%$, which translates directly to a $\sim 5\%$ systematic in the SZE $f_{\rm gas}$ values.

6.4. Cluster Masses

Although the 100 kpc-cut model provides good fits to the outer regions of clusters (cf. §4.4), we cannot know for certain how well the recovered gas and total masses reflect the true masses of the observed clusters. Some handle on the accuracy of the recovered masses can be assessed by fitting projected data from simulated clusters with the 100 kpc-cut model. We carry out this test using simulated clusters from the ART simulations described in §5.2.

Mock *Chandra* observations of these simulated clusters are done by using the true T_e and gas density in each gas cell along with the MEKAL spectral emissivity code (Mewe et al. 1985) to generate an energy-dependent X-ray flux between 0.1 and 10 keV. This flux is then projected along the line of sight, converted to a photon count rate appropriate for $z = 0.01$, and convolved with an instrumental response meant to simulate that of ACIS-I between 0.7 and 2.0 keV. This generates a counts image similar to the *Chandra* level 2 event files described in §3.1. The spectroscopic temperature over a region of interest is then determined using an absorbed MEKAL model in XSPEC (Nagai et al., in preparation). We find that temperatures derived using the MEKAL model differ by at most a few percent from those derived from the relativistic Raymond-Smith model used in our analysis. These temperatures should therefore well approximate the measured *Chandra* temperatures for the clusters in our sample.

We have fit β-models to the simulated counts images described above. Three fits are performed for each cluster; one each to images showing projections along the x, y, and z cluster axes. The likelihood analysis follows the methods of §4.3, and the central 100 kpc of each simulated cluster are excluded from the fit. Any obvious gas clumps are also removed from the mock images prior to fitting. A spectroscopic temperature is measured between 100 kpc and r_{2500}, and the masses are determined at r_{2500} using the methods of §4.2. This analysis is performed on four simulated clusters spanning a range in mass from 8.7×10^{13} to $6.0 \times 10^{14}\,\mathrm{M}_\odot$ at r_{2500}, and the results for both a highly relaxed cluster and a highly unrelaxed cluster are shown in Figure 11. The degree of relaxation of the other two clusters is intermediate between those shown in the figure.

As described in §4.4, the X-ray gas mass is almost directly recoverable from the data. The top panel of Figure 11 shows the results for a cluster observed at a highly relaxed epoch of its evolution. The inner part of the profile is cut off at 100 kpc to emphasize only the regions actually included in the fit. The recovered gas masses for all three projections are accurate to $\sim 3\%$ at r_{2500}, and accurate to $\sim 5\%$ from $0.5r_{2500}$ to beyond $2r_{2500}$. The bottom panel of Figure 11 shows results for a cluster which is observed at an unrelaxed epoch, having undergone a major merger roughly 1 Gyr prior to observation. Despite its unrelaxed state, the gas mass is again recovered with remarkable accuracy at r_{2500}, this time to within $\sim 2\%$. The gas mass is accurate to within $\sim 7\%$ between $0.5r_{2500}$ and $2r_{2500}$ for all three projections. We find similar results for the other two simulated clusters studied, with the gas mass again being recovered to better than 5% at r_{2500}. We therefore conclude that the isothermal β-model with central 100 kpc excluded does an excellent job of recovering the

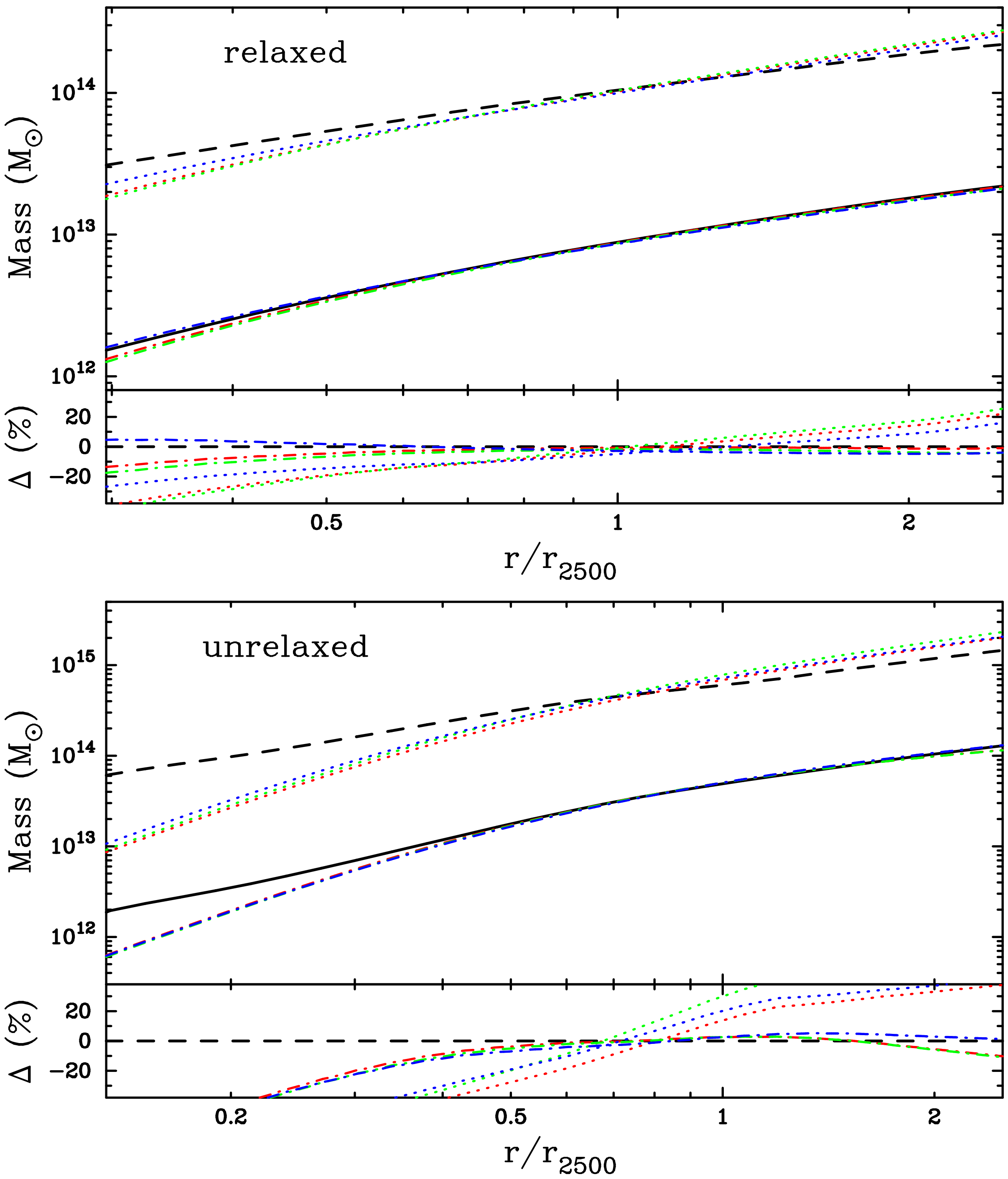

Fig. 11.— Ability of the isothermal β-model to recover the gas mass and total mass at r_{2500} in two simulated clusters, one highly relaxed (top) and one highly unrelaxed (bottom). The top part of each panel shows the true gas mass profile (dark solid line) and true total mass profile (dark dashed line). Dash-dotted lines show gas mass profiles recovered from the β-model fit; red, green, and blue correspond to x, y, and z cluster projections, respectively. Dotted lines correspond to the total mass profile recovered by assuming HSE. The lower part of each panel shows the fractional deviation of recovered masses from true masses as a function of radius. WILL CHANGE THIS TO INCLUDE ONLY MGAS

true three-dimensional gas mass distribution from the two-dimensional projection at radii encompassing r_{2500}. This bolsters our assertion that excluding the central 100 kpc from the fit has a negligible effect on the recovered gas mass, even in a cluster with a very bright cool core. Whether the results presented here extend to real clusters depends on how well the simulations emulate clusters at radii greater than 100 kpc. For now, we can state only that the spectroscopic temperature profiles and gas mass profiles for the simulated clusters agree well with deprojected *Chandra* results for nearby clusters at the radii of interest (Vikhlinin et al. 2005).

Systematic uncertainty in the total mass is treated here.

6.5. Selection Effects

As described in §2, selecting clusters from X-ray surveys on the basis of flux may preferentially select highly elongated objects, particularly if clusters are selected at or near the survey flux limit. We therefore select on the basis of luminosity, although this could lead to preferential selection of cool core clusters or clusters undergoing major merging events. To test for any obvious bias associated with sample selection, we carefully construct a subsample that is expected to be largely free of these effects. The subsample consists of clusters from the BCS catalog (Ebeling et al. 1998), which is compiled with data from a single instrument (*ROSAT*) and has a well-defined flux limit of 4.4×10^{-12} erg cm^{-2} s^{-1} in the *ROSAT* 0.1—2.4 keV band. The subsample contains only clusters with redshifts $z \leq 0.3$, so any bias associated with cluster redshift evolution or point source diminution should not be a factor. We impose a flux cut of 6.6×10^{-12} erg cm^{-2} s^{-1} on the subsample, which is 50% higher than the BCS flux limit. This should reduce selection effects associated with line-of-sight elongation. Finally, we impose a range in intrinsic luminosity $0.35 \leq L_x \leq 1.5 \times 10^{45}$ erg s^{-1} using the 2—10 keV *Chandra* luminosities of Table 1. This eliminates clusters in the extreme high and low luminosity ranges of our sample, which may have unusual dynamical properties. The final subsample consists of the nine clusters A267, A665, A773, Zw3146, A1413, A1914, A2218, A2261, and R2129 for X-ray and SZE I datasets; A1413, A2218, and R2129 are not included in the SZE II dataset.

Gas mass fraction results for both the full cluster sample and the unbiased subsample are provided in Table 17 for each dataset. The differences between results for the X-ray and SZE I datasets are small, at the level of 5%. The change for the SZE II data is larger, but SZE II has considerably fewer clusters and more fluctuation is expected as we go to a smaller sample. There is no significant difference between full sample and subsample results. The X-ray and SZE I $f_{\rm gas}$ results are slightly larger for the unbiased sample, while the SZE II

$f_{\rm gas}$ results are smaller.

6.6. Temperature Structure

As shown in §6.4, there is no indication that the assumption of isothermality significantly biases the X-ray derived gas mass. The temperature dependence of the X-ray surface brightness is very weak compared to its density dependence, and therefore the derived gas mass is only weakly dependent on the assumed temperature. We have not addressed the issue of the SZE-derived gas mass, however, which is much more sensitive to the assumed temperature profile. Although variations in the cluster temperature profiles between 100 kpc and r_{2500} are accounted for in §6.4, an effect not accounted for is the dropoff in temperature profiles seen in cool core clusters beyond r_{2500} (Vikhlinin et al. 2004) and even in non-cool core clusters at larger radii (De Grandi & Molendi 2002). This could be significant, because the central decrement fit for in Eq. [8] is calculated assuming a density profile described by the β-model multiplied by a constant temperature in Eq. [2]. The best-fit density model is determined either from the X-ray data, which are shown to recover the density profile accurately, or by fixing β at the X-ray favored value of 0.7. If the temperature profile is decreasing in the outer regions of the cluster, however, the best-fit central decrement could give too low a central density under the isothermal assumption.

We note that the good agreement between the X-ray and SZE I derived mean gas mass fractions suggests that gas masses derived from the SZE data are not systematically underestimated. It is possible that the SZE observations simply do not sample this cooler gas component since it is distributed on scales larger than those to which the interferometer is sensitive. Mock interferometric SZE observations of simulation-generated Compton-y maps should provide a good test of this, and are currently in progress. For now we perform a cruder

Table 17. Comparison of Full Sample Results with Unbiased Subsample

	mean $f_{\rm gas}$		
Dataset	full sample	unbiased subsample	$\Delta f_{\rm gas}$
X-ray	0.109 ± 0.003	0.114 ± 0.004	+5%
SZE I	0.115 ± 0.005	0.123 ± 0.005	+7%
SZE II	0.116 ± 0.009	0.099 ± 0.008	−15%

test by comparing the SZE gas mass results from the single isothermal β-model with those of the non-isothermal, double β-model in which the temperature profile is parametrized so as to drop to a value 10% of the average cluster temperature at r_{200}. For the two cool core clusters Zw3146 and MS1358 we find that SZE gas masses derived under the isothermal assumption are 15—20% lower than those derived under the double β-model. We cannot attribute this entirely to the difference in temperature profiles since the density models themselves are parametrized differently. Even if the temperature profile does account entirely for the discrepancy, this would be an upper limit since De Grandi & Molendi (2002) have shown the temperature gradient to be milder at large radii in non-cool core clusters. However, we see no evidence for this systematic in our data and we await the results of mock interferometric observations to determine whether the interferometer is sensitive to this component.

6.7. Cluster Substructure

Although we have mostly addressed cluster substructure in terms of its effect on T_x §6.4, gas clumps can also increase the measured surface brightness relative to the SZE as described in §5.1, leading to a higher measured X-ray gas mass. Such enhancements may be difficult to detect if they are faint relative to the noise, or have size scales smaller than the resolution of the instrument.

We find no evidence for a significant clumping factor in our data. The agreement in the mean X-ray and SZE gas mass fractions suggests that the clumping factor is negligible, although we cannot rule out the possibility that competing systematic effects are cancelling. Systematic effects associated with clumping, which would increase the measured X-ray gas mass, would go in the opposite direction of systematic effects associated with temperature structure, which would decrease the measured SZE gas mass as explained above. These effects would therefore not cancel but rather reinforce if present in the data, and this further indicates that neither effect is substantial. Other comparisons of SZE and X-ray results also find little evidence for a large clumping factor (e.g., Grego et al. 2001; Reese et al. 2002). Note that these studies compare the SZE results with X-ray results from *ROSAT*. Clumping should be a less significant factor for *Chandra*, since its superior sensitivity and resolution allow small clumps to be detected and removed before the data are fit.

This is supported by the results of fitting simulated data in §6.4. The simulated clusters do contain small clumps; when they are identified and masked out in the fits, the recovered gas masses agree to better than 5% with the true value at r_{2500}, with no systematic offset (cf. Figure 11). This is an ideal case since there is no background noise in the simulated data; we therefore repeat the fits to the simulated data without masking out any of the clumps and compare the results. We find a maximum increase in gas mass of 9%. These may be extreme limits, however, as the simulations tend to produce exceptionally bright clumps due to high rates of gas cooling (D. Nagai, private communication). Many of the clumps left in have count rates in individual pixels several hundred times higher than those of pixels in surrounding regions, and it is hard to imagine that they would not be detected and masked out even by an instrument with poorer spatial resolution. Incidentally, when only these anomalously bright clumps are removed and the data are refit with the fainter clumps left in, the changes in $M_{\rm gas}$ are at the 1% level.

Although called the clumping factor, C is not only affected by small, discreet gas clumps, but is sensitive to inhomogeneities in the gas density on any scale. Much larger scale density fluctuations are difficult to treat, since they cannot simply be masked out in the fits. However, such large scale fluctuations are seen in the simulated data and are not found to have a measurable effect on the derived gas mass in §6.4.

Finally, excluding the central 100 kpc from the fit should reduce the effects of clumping. This excludes surface brightness enhancements due to structures such as cluster cold fronts, which Markevitch et al. (2003b) show to be more prevalent within 100 kpc. Furthermore, density inhomogeneities at larger radii are averaged over a larger area in computing the surface brightness fits. To test this, we examine the case of the cluster A611 which has a bright source offset $\sim$ 10 kpc from the center, and a comparably bright source offset $\sim$ 200 kpc from the center. Performing the fit to the entire dataset both with and without the bright central source causes a change of $\sim 6\%$ in $M_{\rm gas}$. When this analysis is repeated with the central 100 kpc excluded, this time fitting the dataset both with and without the bright source at 200 kpc, no measurable change in $M_{\rm gas}$is found.

We conclude that there is no evidence that clumping in the gas significantly affects our results when the central 100 kpc are masked out of the X-ray data and bright spots are removed from the images prior to fitting.

7. Conclusions

We have presented results from a study of 36 massive galaxy clusters, incorporating X-ray data from the *Chandra* observatory and SZE data from the BIMA and OVRO interferometers in an effort to constrain both cluster structure and cosmological models. The density model used to obtain cluster masses is simply an isothermal β-model with the central 100 kpc excluded from the X-ray data. The outer regions of all clusters are well fit by this model, and it allows a consistent analysis of the entire sample. A goodness-of-fit analysis indicates that the 100 kpc-cut X-ray model generally provides a better fit in the outer regions of clusters than does a fit to the entire X-ray dataset; this is important since most of the cluster mass measured at r_{2500} is contained outside of the central 100 kpc. Interestingly, a similar analysis indicates that the 100 kpc-cut X-ray shape parameters give a better description of the SZE data than the full-fit X-ray shape parameters; this result strongly suggests that the SZE data are largely insensitive to complex cluster core morphology, since no 100 kpc-cut is made for the SZE data.

The weighted mean X-ray, SZE I, and SZE II $f_{\rm gas}$ results are consistent with each other, suggesting that the effects of clumping are negligible in our analysis and further indicating that the SZE is not sensitive to complicated core physics. The results are also consistent with those of much more complex ICM models, applied to clusters with a range of redshifts, masses, and morphological states. This indicates that simply excluding the central 100 kpc from the X-ray fit gives results consistent with a detailed modeling of the core and that most clusters are well-behaved and self-similar in their outer regions.

We use normalization and shape information from the $f_{\rm gas}$ versus z relation to constrain Ω_M and Ω_Λ. From the normalization only, we find Ω_M results consistent with the *WMAP* constraint but the results are very sensitive to assumptions about the cluster baryon budget. Using the shape of the curve instead does not require assumptions about the baryon budget and is shown to constrain Ω_Λ in addition to Ω_M. Although the results are consistent with independent tests such as *WMAP*, they have large associated uncertainties even when a prior on total density is used. Combining the shape and normalization methods provides the tightest constraints on Ω_M and Ω_Λ, and non-zero constraints on both parameters are obtained from the X-ray data without using a flat prior. When *WMAP* constraints are used as priors on cosmology, our data show that the measured gas mass fraction in clusters within r_{2500} accounts for up to $\sim$ 65% of Ω_B/Ω_M, in good agreement with other cluster studies. However, obtaining precision cosmological constraints through comparison of $f_{\rm gas}$ with Ω_B/Ω_M awaits a better understanding of systematic uncertainties, particularly in the measurement of $M_{\rm total}$.

We account for sources of systematic uncertainty in our measurements, finding that while measured temperatures may be biased low by $\sim$ 10% and the total masses biased low by up to 30%, systematics associated with background estimation, point source contamination and sample selection should have only a small effect on the results. The 100 kpc-cut model is tested by analyzing mock *Chandra* data from simulated clusters with precisely known masses. The model recovers the true three-dimensional gas mass distribution to 5% at r_{2500} in all four simulations, so excluding the central 100 kpc has a negligible effect on the recovered gas mass, even in clusters with bright, cool cores. Finally, a careful analysis shows that clumping in the gas does not significantly affect the results when the central 100 kpc are masked out of the X-ray data and bright spots are removed from the X-ray images.

The consistency among cluster properties derived from X-ray and SZE data suggests that these properties can now be reliably measured. Some shortcomings in our understanding of cluster properties are still apparent, but while the X-ray data used here are among the best currently available, improved SZE measurements will soon come from imaging experiments such as the Sunyaev-Zel'dovich Array and the quality of numerical cluster simulations is advancing at a rapid pace. Meanwhile, the self-consistent results from the large sample presented here demonstrate the promise of using clusters to obtain precision cosmological constraints.

REFERENCES

Allen, S. W. et al. 1992, MNRAS, 259, 67

Allen, S. W., Schmidt, R. W., Ebeling, H., Fabian, A. C., & van Speybroeck, L. 2004, MNRAS, 353, 457

Allen, S. W., Schmidt, R. W., & Fabian, A. C. 2001, MNRAS, 328, L37

—. 2002, MNRAS, 334, L11

Arnaud, K. A. 1996, in Astronomical Data Analysis Software and Systems V, ed. G. H. Jacoby & J. Barnes, 17

Bahcall, N. A., & Fan, X. 1998, ApJ, 504, 1

Birkinshaw, M., Hughes, J. P., & Arnaud, K. A. 1991, ApJ, 379, 466

Böhringer, H. et al. 2000, ApJS, 129, 435

Bonamente, M., Joy, M. K., Carlstrom, J. E., Reese, E. D., & LaRoque, S. J. 2004, ApJ, 614, 56

Borgani, S. et al. 2004, MNRAS, 348, 1078

Burles, S., & Tytler, D. 1998a, ApJ, 499, 699

—. 1998b, ApJ, 507, 732

Burns, J. O. 1990, AJ, 99, 14

Carlstrom, J. E., Joy, M., & Grego, L. 1996, ApJ, 456, L75

Cash, W. 1979, ApJ, 228, 939

Cavaliere, A., & Fusco-Femiano, R. 1976, A&A, 49, 137

—. 1978, A&A, 70, 677

Christensen, N., Meyer, R., Knox, L., & Luey, B. 2001, astro-ph/0103134

Condon, J. J., Cotton, W. D., Greisen, E. W., Yin, Q. F., Perley, R. A., Taylor, G. B., & Broderick, J. J. 1998, AJ, 115, 1693

Cooray, A. R. 1998, A&A, 339, 623

Cooray, A. R., Grego, L., Holzapfel, W. L., Joy, M., & Carlstrom, J. E. 1998, AJ, 115, 1388

Copi, C. J., Schramm, D. N., & Turner, M. S. 1995, ApJ, 455, L95

David, L. P., Jones, C., & Forman, W. 1995, ApJ, 445, 578

De Grandi, S., Ettori, S., Longhetti, M., & Molendi, S. 2004, A&A, 419, 7

De Grandi, S., & Molendi, S. 2002, ApJ, 567, 163

Dickey, J. M., & Lockman, F. J. 1990, ARA&A, 28, 215

Donahue, M., Voit, G. M., Scharf, C. A., Gioia, I. M., Mullis, C. R., Hughes, J. P., & Stocke, J. T. 1999, ApJ, 527, 525

Ebeling, H., Edge, A. C., Bohringer, H., Allen, S. W., Crawford, C. S., Fabian, A. C., Voges, W., & Huchra, J. P. 1998, MNRAS, 301, 881

Ebeling, H., Edge, A. C., & Henry, J. P. 2001a, ApJ, 553, 668

Ebeling, H., Jones, L. R., Fairley, B. W., Perlman, E., Scharf, C., & Horner, D. 2001b, ApJ, 548, L23

Ebeling, H., Voges, W., Bohringer, H., Edge, A. C., Huchra, J. P., & Briel, U. G. 1996a, MNRAS, 283, 1103

—. 1996b, MNRAS, 281, 799

Eke, V. R., Cole, S., Frenk, C. S., & Henry, J. P. 1998, MNRAS, 298, 1145

Elbaz, D., Arnaud, M., & Böhringer, H. 1995, A&A, 293, 337

Ettori, S., & Fabian, A. C. 1999, MNRAS, 305, 834

Ettori, S., Tozzi, P., Borgani, S., & Rosati, P. 2004, A&A, 417, 13

Ettori, S., Tozzi, P., & Rosati, P. 2003, A&A, 398, 879

Evrard, A. E. 1997, MNRAS, 292, 289

Evrard, A. E., Metzler, C. A., & Navarro, J. F. 1996, ApJ, 469, 494

Fabian, A. C. 2003, in Galaxy Evolution: Theory & Observations, ed. V. Avila-Reese, C. Firmani, C. S. Frenk, & C. Allen, 303

Fabricant, D., Rybicki, G., & Gorenstein, P. 1984, ApJ, 286, 186

Feldman, U. 1992, Physica Scripta Volume T, 46, 202

Freedman, W. L. et al. 2001, ApJ, 553, 47

Frenk, C. S. et al. 1999, ApJ, 525, 554

Gamerman, D. 1997, Markov Chain Monte Carlo: Stochastic Simulation for Bayesian Inference (Chapman and Hall)

Gelman, A., & Rubin, D. 1992, Statistical Science, 7, 457

Gilks, W. R., Richardson, S., & Spiegelhalter, D. J. 1996, Markov Chain Monte Carlo in Practice (Chapman and Hall)

Gioia, I. M., & Luppino, G. A. 1994, ApJS, 94, 583

Gioia, I. M., Maccacaro, T., Schild, R. E., Wolter, A., Stocke, J. T., Morris, S. L., & Henry, J. P. 1990, ApJS, 72, 567

Gnedin, O. Y., Kravtsov, A. V., Klypin, A. A., & Nagai, D. 2004, ApJ, 616, 16

Grego, L. 1999, PhD thesis, California Institute of Technology

Grego, L., Carlstrom, J. E., Joy, M. K., Reese, E. D., Holder, G. P., Patel, S., Cooray, A. R., & Holzapfel, W. L. 2000, ApJ, 539, 39

Grego, L., Carlstrom, J. E., Reese, E. D., Holder, G. P., Holzapfel, W. L., Joy, M. K., Mohr, J. J., & Patel, S. 2001, ApJ, 552, 2

Hastings, W. K. 1970, Biometrika, 57, 97

Henry, J. P. et al. 1997, AJ, 114, 1293

Holder, G. P., Mohr, J. J., Carlstrom, J. E., Evrard, A. E., & Leitch, E. M. 2000, ApJ, 544, 629

Itoh, N., Kohyama, Y., & Nozawa, S. 1998, ApJ, 502, 7

Jones, C., & Forman, W. 1984, ApJ, 276, 38

—. 1999, ApJ, 511, 65

Jonker, P. G., Campana, S., Steeghs, D., Torres, M. A. P., Galloway, D. K., Markwardt, C. B., Chakrabarty, D., & Swank, J. 2005, MNRAS, 537

Kazantzidis, S., Kravtsov, A. V., Zentner, A. R., Allgood, B., Nagai, D., & Moore, B. 2004, ApJ, 611, L73

Kirkman, D., Tytler, D., Suzuki, N., O'Meara, J. M., & Lubin, D. 2003, ApJS, 149, 1

Klypin, A., Kravtsov, A. V., Bullock, J. S., & Primack, J. R. 2001, ApJ, 554, 903

Kolb, E. W., & Turner, M. S. 1990, The Early Universe (Addison-Wesley)

Kravtsov, A. V. 1999, PhD thesis, New Mexico State University

Kravtsov, A. V., Klypin, A., & Hoffman, Y. 2002, ApJ, 571, 563

Kravtsov, A. V., Nagai, D., & Vikhlinin, A. A. 2005, ApJ, 625, 588

LaRoque, S. J. et al. 2003, ApJ, 583, 559

LaRoque, S. J., Reese, E. D., Carlstrom, J. E., Holder, G., Holzapfel, W. L., Joy, M., & Grego, L. 2002, astro-ph/0204134

Majerowicz, S., Neumann, D. M., & Reiprich, T. H. 2002, A&A, 394, 77

Markevitch, M. 2002, astro-ph/0205333

Markevitch, M. et al. 2003a, ApJ, 583, 70

—. 2000, ApJ, 541, 542

Markevitch, M., Vikhlinin, A., & Forman, W. R. 2003b, in Matter and Energy in Clusters of Galaxies, ed. S. Bowyer & C. Hwang (The Astronomical Society of the Pacific), 37

Markevitch, M., Vikhlinin, A., & Mazzotta, P. 2001, ApJ, 562, L153

Mason, B. S., Myers, S. T., & Readhead, A. C. S. 2001, ApJ, 555, L11

Mathiesen, B., Evrard, A. E., & Mohr, J. J. 1999, ApJ, 520, L21

Metropolis, N., Rosenbluth, A. W., Rosenbluth, M. N., Teller, A. H., & Teller, E. 1953, Journal of Chemical Physics, 21, 1087

Mewe, R., Gronenschild, E. H. B. M., & van den Oord, G. H. J. 1985, A&AS, 62, 197

Mohr, J. J., Evrard, A. E., Fabricant, D. G., & Geller, M. J. 1995, ApJ, 447, 8

Mohr, J. J., Mathiesen, B., & Evrard, A. E. 1999, ApJ, 517, 627

Myers, S. T., Baker, J. E., Readhead, A. C. S., Leitch, E. M., & Herbig, T. 1997, ApJ, 485, 1

Navarro, J. F., Frenk, C. S., & White, S. D. M. 1995, MNRAS, 275, 720

Navarro, J. F., Frenk, C. S., & White, S. D. M. 1996, ApJ, 462, 563

—. 1997, ApJ, 490, 493

Nollett, K. M., & Burles, S. 2000, Phys. Rev. D, 61, 123505

O'Meara, J. M., Tytler, D., Kirkman, D., Suzuki, N., Prochaska, J. X., Lubin, D., & Wolfe, A. M. 2001, ApJ, 552, 718

Ota, N., & Mitsuda, K. 2002, ApJ, 567, L23

Patel, S. K. et al. 2000, ApJ, 541, 37

Pearson, T. J., Shepherd, M. C., Taylor, G. B., & Myers, S. T. 1994, BAAS, 185, 0808

Pen, U. 1997, New Astronomy, 2, 309

Peres, C. B., Fabian, A. C., Edge, A. C., Allen, S. W., Johnstone, R. M., & White, D. A. 1998, MNRAS, 298, 416

Piffaretti, R., Jetzer, P., & Schindler, S. 2003, A&A, 398, 41

Pospieszalski, M. W., Lakatosh, W. J., Nguyen, L. D., Lui, M., Liu, T., Le, M., Thompson, M. A., & Delaney, M. J. 1995, IEEE MTT-S Int. Microwave Symp., 1121

Press, W. H., Teukolsky, S. A., Vetterling, W. T., & Flannery, B. P. 1992, Numerical Recipes in C. The Art of Scientific Computing (Cambridge University Press, 2nd ed.)

Raftery, A. L., & Lewis, S. 1992, in Bayesian Statistics IV, ed. J. M. Bernardo & M. H. DeGroot (Oxford University Press), 763

Raymond, J. C., & Smith, B. W. 1977, ApJS, 35, 419

Reese, E. D. 2001, PhD thesis, University of Chicago

Reese, E. D., Carlstrom, J. E., Joy, M., Mohr, J. J., Grego, L., & Holzapfel, W. L. 2002, ApJ, 581, 53

Reese, E. D. et al. 2000, ApJ, 533, 38

Rudy, D. J. 1987, PhD thesis, California Institute of Technology

Sanderson, A. J. R., Ponman, T. J., Finoguenov, A., Lloyd-Davies, E. J., & Markevitch, M. 2003, MNRAS, 340, 989

Sasaki, S. 1996, PASJ, 48, L119

Sault, R. J., Teuben, P. J., & Wright, M. C. H. 1995, in Astronomical Data Analysis Software and Systems IV, ed. R. A. Shaw, H. E. Payne, & J. J. E. Hayes, 433

Scharf, C. A., Jones, L. R., Ebeling, H., Perlman, E., Malkan, M., & Wegner, G. 1997, ApJ, 477, 79

Schindler, S. et al. 1995, A&A, 299, L9

Schindler, S., Hattori, M., Neumann, D. M., & Boehringer, H. 1997, A&A, 317, 646

Scoville, N. Z., Carlstrom, J. E., Chandler, C. J., Phillips, J. A., Scott, S. L., Tilanus, R. P. J., & Wang, Z. 1993, PASP, 105, 1482

Snowden, S. L. 1998, ApJS, 117, 233

Spergel, D. N. et al. 2003, ApJS, 148, 175

Stocke, J. T., Morris, S. L., Gioia, I. M., Maccacaro, T., Schild, R., Wolter, A., Fleming, T. A., & Henry, J. P. 1991, ApJS, 76, 813

Struble, M. F., & Rood, H. J. 1999, ApJS, 125, 35

Taylor, A. C., Grainge, K., Jones, M. E., Pooley, G. G., Saunders, R. D. E., & Waldram, E. M. 2001, MNRAS, 327, L1

Thomas, P. A., & Couchman, H. M. P. 1992, MNRAS, 257, 11

Townsley, L. K., Broos, P. S., Garmire, G. P., & Nousek, J. A. 2000, ApJ, 534, L139

Verde, L. et al. 2003, ApJS, 148, 195

Vikhlinin, A. 2005, ApJ—submitted: astro-ph/0504098

Vikhlinin, A., Forman, W., & Jones, C. 1999, ApJ, 525, 47

Vikhlinin, A., Kravtsov, A., Forman, W., Jones, C., Markevitch, M., Murray, S. S., & Van Speybroeck, L. 2005, ApJ—submitted: astro-ph/0507092

Vikhlinin, A., Markevitch, M., Murray, S. S., Jones, C., Forman, W., & Van Speybroeck, L. 2004, ApJ—in press: astro-ph/0412306

Voges, W. 1992, in Environment Observation and Climate Modelling Through International Space Projects, 9

White, D. A., Jones, C., & Forman, W. 1997, MNRAS, 292, 419

White, S. D. M., Navarro, J. F., Evrard, A. E., & Frenk, C. S. 1993, Nature, 366, 429

Winkler, C. et al. 1995, A&A, 302, 765

This preprint was prepared with the AAS LATEX macros v5.0.